



**UNIVERSIDAD NACIONAL AUTÓNOMA DE MÉXICO**  
**POSGRADO EN CIENCIAS E INGENIERIA DE MATERIALES**

STUDY OF THE MICROSTRUCTURE AND RHEOLOGY OF EMULSIONS IN AN AQUEOUS MEDIUM

TESIS

QUE PARA OPTAR POR EL GRADO DE  
DOCTOR EN CIENCIA E INGENIERÍA DE MATERIALES

PRESENTA

JAIRO EDUARDO LEIVA MATEUS

TUTOR PRINCIPAL

DR. ENRIQUE GEFFROY AGUILAR  
INSTITUTO DE INVESTIGACIONES EN MATERIALES

COMITÉ TUTOR

DR. OCTAVIO MANERO BRITO  
INSTITUTO DE INVESTIGACIONES EN MATERIALES

DR. JESÚS GRACIA FADRIQUE  
FACULTAD DE QUÍMICA

MÉXICO, CDMX. OCTUBRE DE 2018.



Universidad Nacional  
Autónoma de México

Dirección General de Bibliotecas de la UNAM

**Biblioteca Central**



**UNAM – Dirección General de Bibliotecas**  
**Tesis Digitales**  
**Restricciones de uso**

**DERECHOS RESERVADOS ©**  
**PROHIBIDA SU REPRODUCCIÓN TOTAL O PARCIAL**

Todo el material contenido en esta tesis esta protegido por la Ley Federal del Derecho de Autor (LFDA) de los Estados Unidos Mexicanos (México).

El uso de imágenes, fragmentos de videos, y demás material que sea objeto de protección de los derechos de autor, será exclusivamente para fines educativos e informativos y deberá citar la fuente donde la obtuvo mencionando el autor o autores. Cualquier uso distinto como el lucro, reproducción, edición o modificación, será perseguido y sancionado por el respectivo titular de los Derechos de Autor.

---

# STUDY OF THE MICROSTRUCTURE AND RHEOLOGY OF EMULSIONS IN AN AQUEOUS MEDIUM

---

A thesis submitted in fulfillment of the requirements for the  
degree of Doctor en Ciencia e Ingeniería de Materiales

---

J. E. LEIVA MATEUS

---









## ***ACKNOWLEDGMENTS***

I want to thank my advisor, Dr. Enrique Geffroy, for allowing me to work in his laboratory and offer me not only his moral support but above all his trust that never faded. Also, the many talks that will always be for me, an inexhaustible source of growth. For having instilled in me the meticulous work and rigor of this profession, the taste for cultivating the critical spirit and all the essential values for this noble profession of research.

To my laboratory colleagues, Liz, and their weather forecasts, Israel and the challenging chess competitions, Carlos and the coffee of his land, Johana, Alfredo, Roberto, Elsa, Lay, Moisés, Rocío, Jorge (visitor); I wish to express my sincere gratitude. I also thank the people who have participated in this work, in particular, Dr. Marco A. R. Huesca for the discussions and clarify several of my ideas.



To my soccer friends for their kindness, encouragement and hope towards me in precise moments in my last stage of writing and publishing; In particular, the Torres Rodríguez family always gave me moments of happiness.

I am primarily and profoundly grateful to Ix Chel whose friendship and spiritual support filled me with consolation in my darkest days in this last stage. I would also like to express my thanks to César, Jess, Christian, Ana, and Lalo, who came to help me when my health was weak, thank you, really appreciate you, thank you very much.

I also thank CONACYT, PAPIIT-IN114618 and, Roberto Rocca Education Program for the financial support to finish my Ph.D studies.

With a little heart, I am leaving these crucial years of my life. A new adventure will take place, but first, with great pleasure I thank each and every one of the people who accompanied me during this time, I will always remember them.

My last lines will be for my family, from whom I always received support and encouragement. In particular to my sisters, Johana and Marcela, and Sofia, my mother, thank you for accepting to live the sacrifice of remoteness; the words will not be enough to express my gratitude.

*A mi madre, gracias por aceptar vivir el sacrificio de la lejanía.*



"Do not tell me  
that I will be okay  
until you have seen  
the monsters I battle  
every time the sun  
goes down".

unknown





## ***OUTLINE OF THE THESIS***

In this thesis, observations are made on the morphological behavior of a concentrated emulsion (Water-in-Oil; W/O) under resting and shear conditions. The background information on the morphology, behavior, and properties of emulsions will be reviewed in Chapter 1. Chapter 2 presents the procedure of elaboration of the emulsion, the materials used, the procedure of placing the emulsion sample in the flow cell, the steps followed for image processing and the methods used in this thesis.

The results about the changes of the distribution of the size of the dispersed phase under different conditions of shear rate ( $0.75 \text{ s}^{-1}$  to  $4.5 \text{ s}^{-1}$ ), before and after the flow, are presented and analyzed in Chapter 3. One of the phenomena observed is the band formation —aligned along the vorticity axis— as the shear rate increases,

whose description and the associated structural changes of the dispersed phase is presented and analyzed in Chapter 4

A second, no less important observation on the behavior of these complex systems, is the role played by the excess free energy of the interfaces —associated to the surface tension of deformed drops— in the highly concentrated emulsion. In Chapter 5, the measurement of the interfacial tension between the two phases by the Deformed Drop Retraction (DDR) Method is described, as well as other possible effects due to the presence of other nearby drops during the time of retraction of the target drop. The main conclusions of this work are expressed in Chapter 6. Lines of future research are also included. Additional information is shown in the Appendices.

## ***ABSTRACT***

Understanding the rheology of immiscible liquids mixtures, as well as the role played by its micro-structures, are important criteria for the production of new materials and processes in industry. Here, we study changes over time of the droplet size distributions of emulsions induced by slow shearing flows. We observe that the initial heterogeneous microstructure may evolve toward more complex structures (such as bimodal distribution) as a result of coalescence and rupture of droplets. These dynamic structures were produced using a flow cell made up of two parallel disks, separated by a gap of 100  $\mu\text{m}$ . The steady rotation of the lower disk generates a simple shear flow of  $0.75 \text{ s}^{-1}$ , during  $\sim 400 \text{ s}$ . After a brief rest time, this procedure was repeated by applying a step ramp until the maximum shear rate of  $4.5 \text{ s}^{-1}$  was reached, using step increments of 0.75. During the last portion of the flow and during the rest time in between flows, structures of



emulsions were characterized. Initially, a broad single-peak distribution of drops was observed, which evolved toward a slightly narrower bimodal distribution, at first due to the coalescence of the smaller droplets and subsequently of the larger drops. The rupture of drops at higher shear rates was also observed. The observed evolutions also presented global structures such as “pearl necklaces” or “bands of particles,” the latter characterized by alternating bands of a high density of particles and regions of the continuous phase with only a few droplets. These changes may indicate complex, time-dependent rheological properties of these mixtures.

In the present work, the optical analysis of the evolution of the microstructure of the emulsion is carried out. Statistical descriptions are made, and possible scenarios of evolution are planned.

## TABLE OF CONTENTS

<b>ACKNOWLEDGMENTS .....</b>	<b>I</b>
<b>OUTLINE OF THE THESIS .....</b>	<b>VII</b>
<b>ABSTRACT.....</b>	<b>IX</b>
<b>TABLE OF CONTENTS .....</b>	<b>XI</b>
<b>CHAPTER 1: MORPHOLOGY OF EMULSIONS .....</b>	<b>1</b>
1.1.    BACKGROUND .....	1
1.2.    DEFORMATION OF A DROP UNDER A FLOW .....	2
1.3.    NEWTONIAN SYSTEMS.....	5
1.4.    NON-NEWTONIAN SYSTEMS.....	14
1.5.    RETRACTION OF NEWTONIAN DROPS AFTER STOPPING THE FLOW.....	19
1.6.    COALESCENCE OF DROPS.....	21
1.7.    CHAPTER CONCLUSIONS .....	24
1.8.    REFERENCES .....	25
<b>CHAPTER 2: EXPERIMENTAL SETUP AND METHODS .....</b>	<b>29</b>
2.1.    OVERVIEW OF EXPERIMENTAL SETUP.....	29
2.2.    THE FLOW CELL .....	30
2.3.    DESCRIPTION OF ADDITIONAL EQUIPMENT.....	32
2.4.    PREPARATION OF THE EMULSION.....	35
2.5.    PLACEMENT OF THE SAMPLE IN THE CELL.....	40
2.6.    IMAGE PROCESSING TECHNIQUE.....	42
<b>CHAPTER 3: EVOLUTION OF THE SIZE DISTRIBUTION OF AN EMULSION UNDER SIMPLE SHEAR FLOW.....</b>	<b>47</b>
3.1.    BRIEF THEORETICAL BACKGROUND .....	48
3.1.1. <i>Introduction</i> .....	48
3.1.2. <i>Coalescence in slow flows</i> .....	51
3.1.3. <i>Breakup of Droplets under a Shearing Flow</i> .....	54
3.2.    MATERIALS AND METHODS.....	55
3.2.1. <i>Constituents and preparation of emulsions</i> .....	55
3.2.2. <i>Smooth kernel distribution estimation</i> .....	59
3.2.3. <i>Size Distribution of the initial emulsion</i> .....	60
3.2.4. <i>The experimental conditions</i> .....	65
3.3.    RESULTS .....	68
3.4.    DISCUSSION .....	76
3.5.    CHAPTER CONCLUSIONS .....	80
3.6.    REFERENCES .....	82

<b>CHAPTER 4: MORPHOLOGY OF BANDED, ANYSOTROPIC STRUCTURES .....</b>	<b>85</b>
4.1. INTRODUCTION.....	86
4.1.1. <i>Shear banding in the emulsion</i> .....	88
4.1.2. <i>The breakup of droplets under a shearing flow</i> .....	90
4.2. MATERIALS AND METHODS.....	91
4.2.1. <i>Constituents and preparation of emulsions</i> .....	91
4.2.2. <i>Parallel disks cell/device</i> .....	93
4.2.3. <i>Images analysis</i> .....	95
4.2.4. <i>The Horizontal Distribution of Drops. The velocity field of the developed flow on the x-w plane.</i>	104
4.2.5. <i>The Vertical distribution of drops. The velocity field of the developed flow on the x-y plane.</i> .....	109
4.3. DISCUSSION OF RESULTS .....	113
4.3.1. <i>Critical capillary in concentrated emulsions</i> .....	113
4.4. CHAPTER CONCLUSIONS.....	120
4.5. REFERENCES.....	122
<b>CHAPTER 5: IN SITU MEASUREMENT OF INTERFACIAL TENSION OF AN EMULSION.</b>	<b>125</b>
5.1. DEFORMED DROP RETRACTION METHOD .....	126
5.2. TIME CONSTANT.....	127
5.3. MEASUREMENT OF THE INTERFACIAL TENSION.....	129
5.4. EXPERIMENTAL PROGRESS OF THE PROPOSAL.....	131
5.5. SOME RESULTS.....	134
5.6. DISCUSSION OF RESULTS .....	138
5.7. REFERENCES.....	140
<b>CHAPTER 6: GENERAL CONCLUSIONS .....</b>	<b>143</b>
6.1. STATISTICAL CHARACTERIZATION OF THE DATA OF THE DIAMETERS OF THE EMULSION.....	144
6.2. BAND FORMATION .....	145
6.3. MEASUREMENT OF INTERFACIAL TENSION IN SITU .....	146
6.4. SUGGESTIONS FOR FUTURE WORK.....	146
<b>APPENDIX A.....</b>	<b>149</b>
SAMPLE SIZE .....	149
<b>APPENDIX B .....</b>	<b>151</b>
THEORETICAL DESCRIPTION OF PARALLEL CIRCULAR DISCS.....	151
<b>APPENDIX C .....</b>	<b>155</b>
LOCATION OF THE IMAGE CAPTURED IN THE OBSERVATION HOLE.....	155
<b>APPENDIX D.....</b>	<b>159</b>
CALIBRATION AND RESOLUTION OF THE IMAGE.....	159
<b>APPENDIX E .....</b>	<b>163</b>

## ***Chapter 1: Morphology of emulsions***

### **1.1. Background**

Emulsions prevalence is widespread in an extensive range of industrial applications, including foodstuff, pharmaceuticals, cosmetics, plastics, fertilizers, construction materials, and oil-well engineering. The rheological properties of these emulsions are a complex and highly dependent on a set of various factors, including the properties of the fluid, the shape of the particle and size, and the volume fractions of the liquids. The knowledge of the microstructure and the rheological properties of the emulsion are essential for understanding and possible manipulation of flows in different fields of application. In the present work, the distribution of drop sizes of the dispersed phase is studied after the application of

a simple shear rate in a parallel disks flow cell with a of 100  $\mu\text{m}$ . The shear rate ranges from  $0.75 \text{ s}^{-1}$  to  $4.50 \text{ s}^{-1}$ . Details are described in the following Chapters.

## 1.2. Deformation of a drop under a flow

The study of biphasic systems, such as an isolated drop in an immiscible matrix, has been the subject of numerous experimental, theoretical and numerical publications since the pioneering works of Taylor [1,2], Tomotika [3], Grace [4], Stone & Leal [5]. They have approached the problem from various perspectives, developing the theories that have successfully been verified experimentally and numerically. The first work about the deformation of drops embedded in another fluid were those carried out by Geoffrey Ingram Taylor [1,2], for systems of Newtonian components, where two dimensionless numbers are defined plus a deformation parameter: the ratio of the viscosities  $p$ , the capillary number  $Ca$  and the Taylor deformation. The value of  $p$  is the ratio of the viscosity of the drop between the viscosity of the matrix,

$$p = \eta_d / \eta_m. \quad (1.1)$$

The dimensionless number of the capillary represents the relation of the viscous forces, those that tend to deform the drop, and the superficial forces that tend to maintain the spherical shape.

$$Ca = \frac{\eta_m \cdot \dot{\gamma}}{\sigma/R} = \frac{\eta_m \cdot R \cdot \dot{\gamma}}{\sigma}. \quad (1.2)$$

Where  $\dot{\gamma}$  is the applied stress,  $\sigma$  is the interfacial tension and  $R$  is the radius of the drop in its spherical shape. If the shape of the drop is a three dimensional ellipsoid, then Taylor deformation of a drop is characterized by two measures:

$$D_{Taylor} = \frac{L - B'}{L + B'} \quad (1.3)$$

$$D'_{Taylor} = \frac{L' - W}{L' + W} \quad (1.4)$$

where  $L$  and  $B$  are the length and width of the deformed drop in the flow-gradient plane, respectively, as shown in Figure 1.1a. The Taylor deformation on the flow-vorticity observation plane ( $D'_{Taylor}$ ) is defined in Equation. 1.4, where  $L'$  is the projection of  $L$  and  $W$  is the width of the deformed drop as shown in Figure 1.1a. Taylor's work predicts that the deformation depends on the capillary number and the viscosity ratio, Equations. (1.1) and (1.2), obtaining Equation (1.5); this relationship is applicable for all deformations of drops. It is emphasized, that the deformation of the droplet is limited by the equations of mass conservation and momentum of the two fluids.

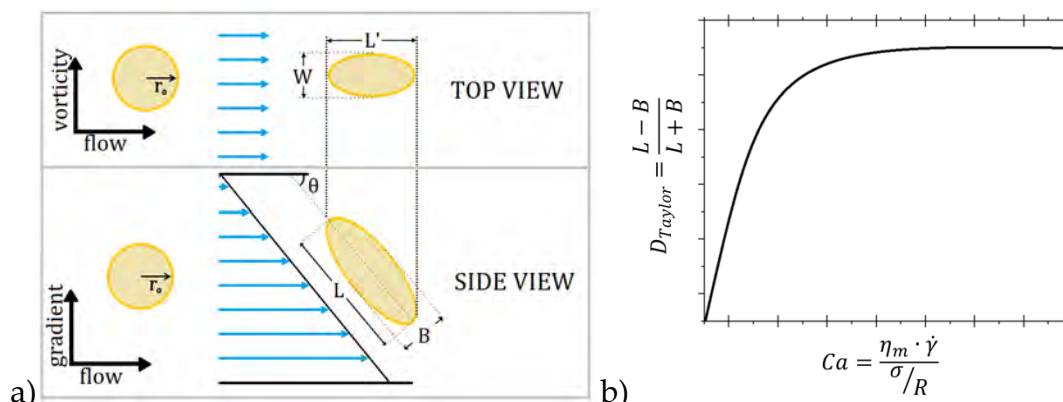
$$D_{Taylor} = D_T = Ca \frac{19p + 16}{16p + 16} \quad (1.5)$$

With appropriate boundary conditions, it can be solved analytically. For example,

- If the deformation  $D_T$  is large, we have that  $D_T$  approaches the unit asymptotically and its orientation angle  $\theta$  is zero [6];
- For small deformations,  $D_T < 0.2$ , we have the same capillary number, that is  $D_T = D = Ca$ , and its behavior is linear (Figure 1.1b).
- For a zero capillary number, the deformation equals zero, and the drop has a spherical shape.

The Taylor deformation, therefore, increases the “real” capillary number seen under flow conditions, as shown in Figure 1.1b. It is explained in more detail in the following Sections of this Chapter.

Now, when a drop is subjected to a stress field, there are two possibilities: that it deforms until it reaches a steady state or that it elongates sufficiently and its rupture occurs. This rupture is due to the application of a greater stresses that exceeds the interfacial forces that keep the drop in its deformed shape but without breaking. The drop can be broken by different mechanisms; this break depends mainly on the viscosity ratio  $p$ , the applied flow, the interfacial tension and other elastic properties of the phases.



**Figure 1.1.** (a) Diagram of the deformation and orientation of a drop under simple shear rate seen from the side and seen from above. (b) projection of Taylor deformation prediction.

In the following Sections, said break mechanisms are described in greater detail. Different cases can be found, depending on the rheological characteristics of the dispersed and continuous phases. The most frequently studied is the fully Newtonian system, where both the dispersed and continuous phases are Newtonian. However, in industry, most cases have thinning by shear flow or viscoelasticity, which are not Newtonian systems, like most emulsions. The following paragraphs present the generalities of the theories and models developed for Newtonian and non-Newtonian systems, as well as the role of coalescence and the measurement of interfacial tension by the DDR method.

### 1.3. Newtonian systems

The best-known model for Newtonian systems is the 1969 Cox model [7], which describes the deformation by the relationship of two dimensionless numbers,



which were already defined in the previous section, the viscosity ratio  $p$  and the capillary number  $Ca$ . Equation (1.6) is only valid if the Taylor deformation is small ( $D_T < 0.2$ ). For this case  $p$ , must necessarily be large or  $Ca$  be very small, or both conditions would fulfill the Cox model conditions. Experimentally, it has been found that for small  $p$  values ( $p \rightarrow 0$ ) they fulfill the Cox model and describe it favorably [8].

$$\frac{L - B}{L + B} = \frac{5(19p + 16)}{4(1 + p)\sqrt{(19p)^2 + \left(\frac{20}{Ca}\right)^2}} \quad (1.6)$$

The model of Maffettone and Minale (model MM) [9], which is phenomenological and for Newtonian systems, is valid for small deformations, by assuming that drops are ellipsoids of revolution at all times and that the interfacial forces are additive. For the stationary state of bead deformation, that is, a well-defined ellipsoid, they are given by the following equations:

$$L^2 = \frac{f_1^2 + Ca^2 + f_2Ca\sqrt{f_1^2 + Ca^2}}{(f_1^2 + Ca^2)^{1/3} \cdot (f_1^2 + Ca^2 - f_2Ca)^{2/3}},$$

$$B^2 = \frac{f_1^2 + Ca^2 + f_2Ca\sqrt{f_1^2 + Ca^2}}{(f_1^2 + Ca^2)^{1/3} \cdot (f_1^2 + Ca^2 - f_2Ca)^{2/3}}, \quad (1.7)$$

$$W^2 = \frac{f_1^2 + Ca^2 + (f_2 Ca)^2}{(f_1^2 + Ca^2)^{1/3} \cdot (f_1^2 + Ca^2 - f_2 Ca)^{2/3}}.$$

With,

$$f_1 = \frac{40(p + 1)}{(2p + 3) \cdot (19p + 16)}, \quad (1.8a)$$

and

$$f_2 = \frac{5}{(2p + 3)} + \frac{3Ca^2}{2 + 6Ca^2}. \quad (1.8b)$$

The term  $f_2$  in parentheses was added to predict deformations of very high  $p$  and high  $Ca$ . This model is not valid for large deformations where the drop ceases to be a *simple ellipsoid of revolution*. At first, we have a spherical drop, and we have the following possible cases described in Figure 1.2. If a significant effort is applied, the drop stops being ellipsoidal. The drop is deformed from a stable stationary state and finally presents sigmoid shape previous to rupture —i.e., with increasing shear value or going past the value of  $Ca_{cr}$ . Experimentally, the critical value is determined by increasing the applied shear rate, where different states are classified into four categories of deformation and breakage as a function of  $p$ .

The importance of the work of Rumscheidt and Mason [10] is the wide range of viscosity ratios and interfacial tensions they studied, and observing four different types of possible deformations under simple shear flow. In Figure 1.2, the four

types of deformation are presented; for each case, the shear rate is applied from the initial spherical drop shape and evolving to an ellipsoid if the deformation is small. When increasing the shear rate the break of the drop is observed:

a) *Deformation type I*: For low values of  $p$ . Shear rate is higher than the critical value, the drop adopting a sinusoidal shape with sharply pointed ends, which release continuously small drops. This phenomenon is known as Tip-streaming.










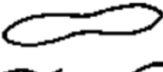



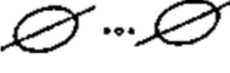
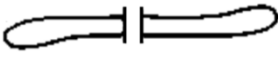


b) *Deformation type II*:  $p = 1.0$ , and above its  $Ca_{cr}$ . Drops form a series of necks that end up breaking up and leaving a set of smaller drops known as satellite drops, while the larger part is divided into two drops daughters.

c) *Deformation type III*:  $p = 0.7$  and  $Ca > Ca_{cr}$ , the drop elongates as a band, until it becomes unstable and breaks up into several drops.

d) *Type IV deformation*:  $p > 4$ , no rupture has been observed.

As can be observed in Figure. 1.2, the orientation angle  $\theta$  plays a significant role when deformations deviate from the spheroidal shape— $\theta$  corresponds to the angle between the principal axis of the drop and the direction of the flow field.

For example, Rumscheidt & Mason [10] observed that *all* drops deform and align with an angle  $\theta$ . The angle  $\theta$  starts from  $45^\circ$ , and as the shear rate increases the orientation decreases until it reaches zero. For *Type I* drops, only when  $p \sim 2 \times 10^{-4}$  and Taylor deformations are  $0.01 < D_{Taylor} < 0.4$ , then the observed angle is  $45^\circ > \theta > 30^\circ$ . When  $D_{Taylor} = 0.54$ , then  $\theta = 25^\circ$ . In *Type II* and *Type III* drops, with  $p = 1$  and  $D_{Taylor} = 0.1$ , an angle of  $\theta = 45^\circ$  is observed. For  $0.2 < D_{Taylor} < 0.58$ , an angle of  $30^\circ > \theta > 15^\circ$  is measured. For *Type IV* drops, with  $p = 17$  and  $D_{Taylor} = 0.29$  the measured angle is  $\theta = 0^\circ$ .

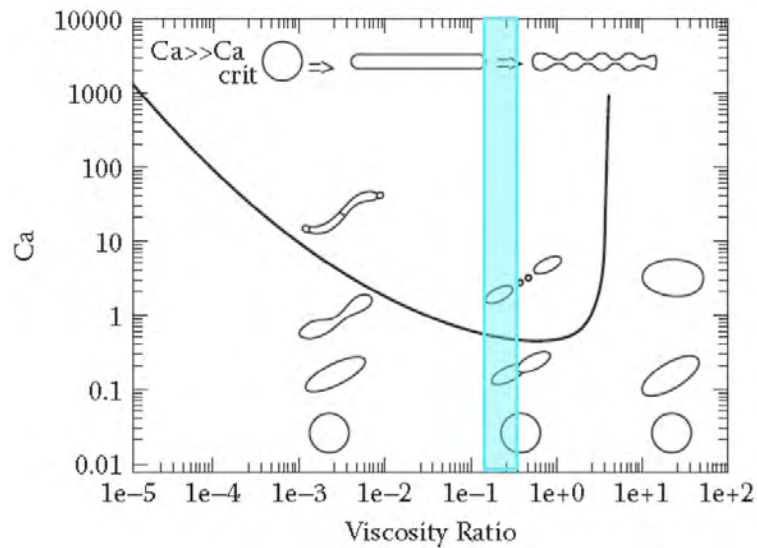
INTERFACIAL TENSION VISCOSITY RATIO	$\sigma < 10$	$10 < \sigma < 20$	$\sigma < 20$	$\sigma > 4.0$
	$p < 0.14$	$0.14 < p < 0.65$	$0.7 < p < 2.2$	$p > 38$
	<i>Type I</i>	<i>Type II</i>	<i>Type III</i>	<i>Type IV</i>
1				
2				
3				
4				
5				

**Figure 1.2.** Schematic of the different types of deformation of a single drop in a simple flow. Adapted from Rumscheidt and Mason 1961.

This angle  $\theta$  can be calculated using Equation (1.9) given by Cerf [11] and then correlated with the theoretical work of Rumscheidt and Mason [10], using measures of deformation and the ratio of viscosities  $p$ .

$$\theta = \frac{\pi}{4} - D_T \cdot \left( \frac{2p + 3}{5} \right). \quad (1.9)$$

We also have the experimental work of Grace [4] where it is found that  $Ca_{cr}(p)$  —that is, as a function of the quotient of viscosities  $p$ — provides information about the conditions of breakup of drops.



**Figure 1.3.** Effect of the viscosity ratio in the capillary number, determined by Grace (1982) and fixed by De Bruijn (1989), the Cyan box is the conditions of our experiment. The figure is taken from [51].

The curve shown in Figure 1.3 establishes the domains for non-rupture and rupture, valid for Newtonian systems. It is clear that the critical capillary varies with the viscosity ratio  $Ca_{cr}(p)$ . For example, the breaking up of the dispersed phase in an emulsion can be determined if we vary the viscosity ratio while keeping other parameters constant (such as the interfacial tension and initial radius). For small values of  $p$ , the breakup of drops is more resilient, hence a large

deformation is observed. The breakup occurs more easily for values of  $0.1 < p < 1$ , with  $Ca_{cr}$  of approximately 0.5. For values of  $p$  higher than 3.5 to 4 it becomes impossible to break up the dispersed phase. This conclusion is supported in the literature in particular with Rumscheidt and Mason [10]. This type of curves can be obtained by increasing the shear rate step by step, then reaching the steady state for each advance.

Another mechanism of rupture is observed when  $p$  is very low ( $p < 0.1$ ) and  $Ca_{cr} \sim 0.5$ , and is known, as already mentioned, as tip-streaming [1, 2, 4, 10, 12]. Then drops adopt a very pointed shape and small droplets are shed in rapid succession from the ends; this effect may be explained by interfacial tension gradients on the surface of the drop, with values at the tips smaller than in the bulk [13]. In recent studies, the presence of surfactants in the surface of the drop generates even more pronounced tip-streaming effects, for example,  $0.3 < p < 3.3$ . However, for values of  $p = 30$ , the effects are less pronounced. In both cases, drops are aligned in the flow direction ( $\theta = 0$ ) or inducing small orientation angle [14, 15].

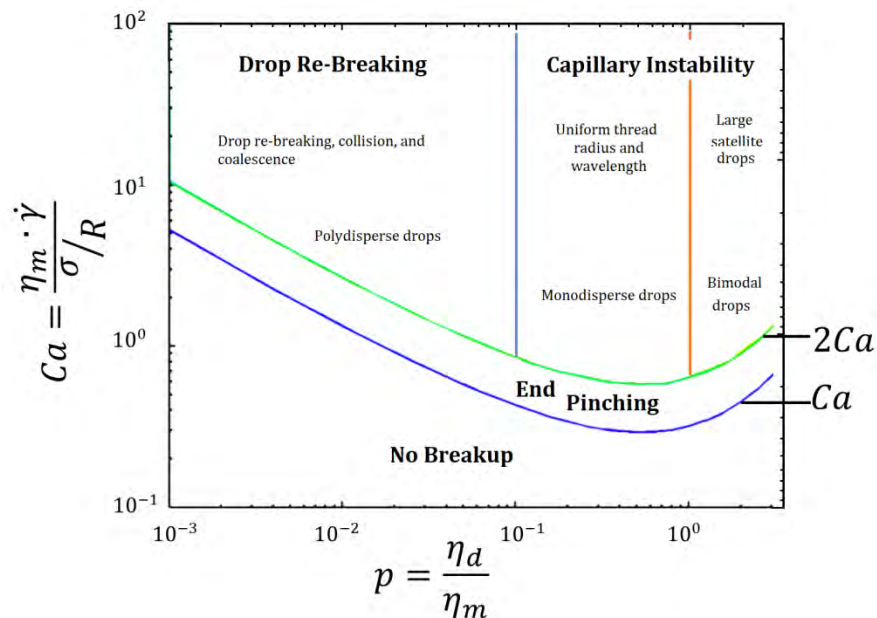
A new mechanism of rupture of drops occurs when the applied flow is stopped after attaining a large deformation of the drop [5,6]. If an elongated drop attains a larger than a critical deformation, and the flow then stops, the retraction process

towards the state of a spherical drops, may produce the fragmentation into small drops. These smaller drops are observed at the ends of the mother drop, reducing the pointed tips at the ends. The disappearance of the tips provides for a secondary mechanism for the interfacial tension to regain its uniformity when recovering a spherical shape.

Cristini [16] presents his work taking into account the size of the drop *after the breakup*. The first stage of this breakup mechanism corresponds to formation of two smaller drops called daughters, of similar size to the critical size. That is to say, when there is no rupture, regardless of the initial size of the mother drop. The second breakup stage occurs at the pointed ends (end-pinching) or by the instabilities that form multiple satellite drops. The size of the satellite drops is determined by the width of the neck after the first rupture mechanism. Cristini concludes that for emulsified systems the size distribution only depends on the first average of the drop size and the  $\dot{\gamma}$ .

On the other hand, studies by Changzhi & Liejin [17] show that the diameter of the daughter droplets is linearly correlated with the inverse shear rate, but independent of the initial size of drops. They also showed that the three types of breakup mechanism can occur, depending on the capillary number  $Ca$ . If  $Ca \cong Ca_{cr}$ , the rupture mechanisms are drop sequences, similar to necklaces,

producing daughter droplets of approximately equal size, sometimes separated by satellite drops. For  $Ca_{cr} < Ca < 2Ca_{cr}$  end shedding appears (end pinching), and this mechanism of rupture is dominant if  $Ca > 2Ca_{cr}$  due to capillary instabilities.



**Figure 1.4.** Complement to Grace and De Bruijn's graphics Adapted from Zhao 2007.

Similar results were found by Zhao [18], who studied the mechanism of rupture and the final size distribution of the drops which depend on  $Ca$  and  $p$ , as shown in Figure. 1.4. This study reveals new evidence of possible mechanisms of rupture of drops. However, these results should be considered with care since drops may have been subjected to effects of walls or confinement, which promote deformation. Of course, the existence of neighboring drops must also be taken into account since the ratio of the diameter of drop and the separation distance between drop centers varies from 0.1 to 0.7. Values of this ratio less than 0.1 are



desirable in order to neglect hydrodynamic effects with wall or other nearby drops.

Other more recent studies by Vananroye [19, 20] have shown that confining effects favor the deformation and orientation along the flow direction. Interestingly, this phenomenon was possible until the breakup of drops with high viscosity ratios  $p > 3.5$  becomes impossible. With confinement and for  $p > 1$ , the critical values of the capillary decreases and therefore favors breakup. Rupture for values of  $p < 1$  requires larger values of  $Ca_{cr}$ . Sibillo and colleagues [21] found similar results for values of  $p = 1$ ; they show that the confinement enriches the deformation but prevents the drop rupture due to the proximity of the flow lines; that is, increments of the vorticity, away from the drops (towards the wall), reduces the rate of elongation of the drop.

#### **1.4. Non-Newtonian Systems**

Gauthier and collaborators [22] published the first results of *systems of Newtonian droplets in viscoelastic matrices*, using tubular or Poiseuille flow. They did not report a relationship with the deformation of the drops. Flumerfelt work [23] measures the deformation and rupture of the Newtonian droplets in a viscoelastic matrix, finding that the effort required for the rupture of droplets in

a viscoelastic fluid is less than that required in Newtonian systems under similar conditions, i.e., same viscosity ratio  $p$  and same applied stress.

As well, the deformation of drops in a diluted emulsion is favored when a viscoelastic matrix is used, as reported by Elmendorp & Maalcke [24], Mighri [25]. Although this study provided a new perspective on the influence of the elasticity of the matrix, it did not allow a complete understanding of the effect of elasticity and shear thinning of the matrix on the deformation of a Newtonian drop. It does provide some very relevant insights; e. g., when observing shear thinning effects in the viscoelastic matrix, which increases the  $p$  values, causes more stable drops, when compared with those of Newtonian matrix. But when values of normal stresses increase —increasing elongational stresses— drops become more strongly destabilized and rupture occurs earlier, compared to Newtonian systems under similar conditions.

In another work by Sibillo [26], the elasticity of the matrix limits the deformation of the dispersed phase, compared to a purely Newtonian system under similar conditions; i. e., with the same viscosity ratio and nearby wall stresses. It is also reported that the drops are more aligned —oriented in the flow direction— compared to their similar Newtonian system [21, 27]. It is believed that stronger orientation of the drop —with respect to the flow— correlate with the existence

of additional normal stresses of the matrix. De Bruijn's doctoral thesis [13] presents an extensive study of systems with viscoelastic droplets under *pure shearing flows*, by comparing the medium contribution of two types of viscoelastic fluids. The first one does not have any measured elasticity (known as a viscometric flow) and a second purely elastic fluid, called a Boger fluid (fluids whose shearing viscosity is constant, i.e., it does not depend on the shear rate, but normal stresses are observed). It is shown, that in the case of drops with shear thinning and  $p < 0.1$ , the  $Ca_{cr}$  could be correlated with the breaking criterion that is determined in systems Newtonians. For  $p \geq 1$ , the critical  $Ca_{cr}$  deviates from those observed for Newtonian systems, increasing for larger viscosity ratios.

Several studies followed the use of similar fluids. For example, Lerdwijitjarud [28], Mighri [25], Milliken & Leal [29], Sibillo [26]. Tsakalos [30], Varanasi [31], also reported that elastic drops produce high critical capillary numbers, meaning that it is more difficult to break the elastic drop in a Newtonian matrix when compared to a similar purely Newtonian system. The most recent studies agree with the inhibition of the elongation of the drop and the resistance to the rupture caused by the elasticity of the drop in comparison with the entirely Newtonian systems. These works conclude that the critical steady-state capillary number

increases with the *first normal stress difference* of the dispersed phase. The work of Sibillo and collaborators with non-Newtonian systems, also shows that no difference of the behavior of the Newtonian drops could be observed for small deformations and, therefore, that the small deformation limit could be used to derive interfacial tension, independently of the viscoelasticity of one phase or another [26]. For higher capillary numbers, drops show a less distorted appearance and a smaller orientation angle than for Newtonian drops, confirming the theoretical predictions [32]. They also reported an overshoot of the deformation before reaching its steady state. In some cases, breakage was reported in the vorticity axis for Boger liquid drops [34]. This type of behavior occurs most frequently when both phases are viscoelastic.

Now, when both phases are viscoelastic, deformation and rupture of the disperse phase have been studied mainly to understand the morphology of polymer mixtures. It is found that the deformation of a drop in such systems depends mainly on the elasticity ratio, i.e., the elasticity of the drop normalized with respect to the elasticity of the matrix, which corresponds to the ratio of first normal stresses differences [25]. When this ratio is low ( $< 0.37$ ) and, consequently, the elasticity of the matrix is high, the deformation of the drop is higher than that observed for Newtonian systems. On the other hand, when the

drop is highly elastic (elastic ratio  $> 0.37$ ), its deformation is inhibited. This result is to be expected when taking into account the observations mentioned in the previous sections.

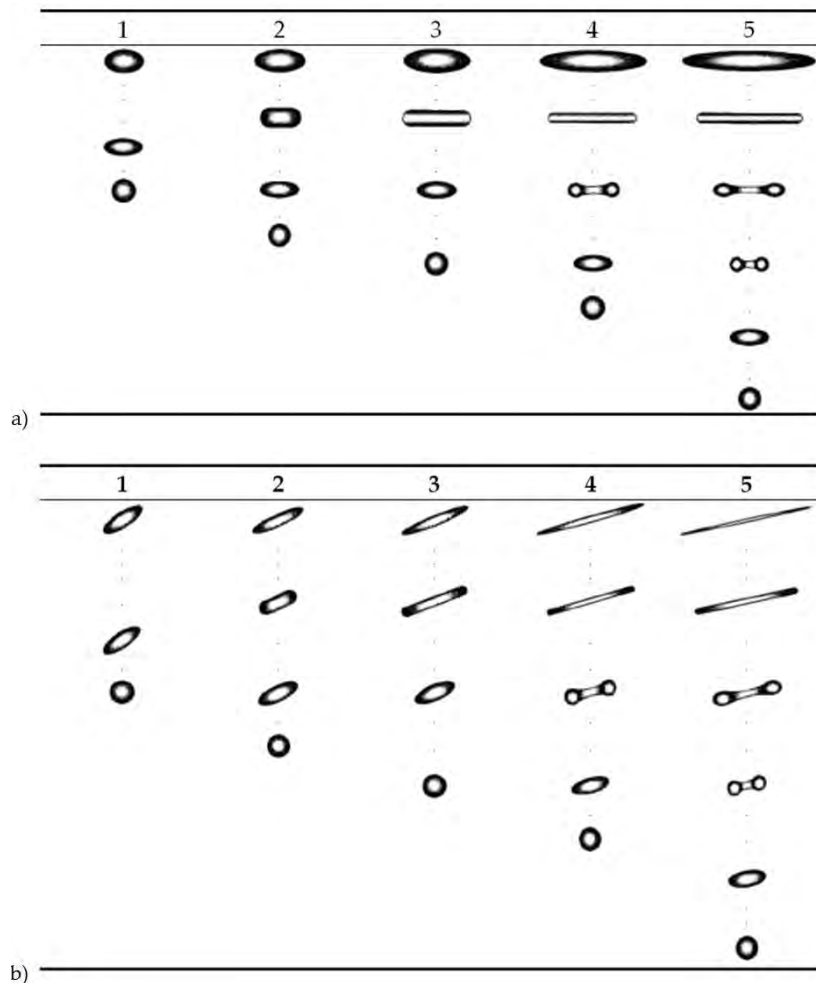
A more unusual deformation (and rupture) mechanism was observed, consisting of a widening of the drop on the plane perpendicular to the flow, especially along the vorticity axis [35, 36]. Levitt and Macosko [35] were the first to report this phenomenon, finding an analytical relationship between the second difference in the normal tension of the phases and the degree of widening. Tanpaiboonkul and colleagues [36] divided the evolution in time of the deformation of the drop into three distinct stages. The first consists of elongation of the drop in the direction of flow followed by a contraction —a lengthening by the secondary flow—, and finally a widening along the direction of the vorticity. It appears that a sufficiently strong elasticity of the droplet and/or matrix can hinder rupture along the direction of flow leading to rupture along the axis of vorticity. The latter can be a consequence of much higher capillary numbers than those observed in the flow axis. Finally, a later study showed that this type of behavior depends on the size of drops [34]. The primary rupture occurs in the flow direction, but the daughter drop obtained broke along the direction of vorticity, by a rupture mechanism describe as erosion.

Ghodgaonkar & Sundararaj [37] developed a model of droplet diameter in polymer blends, based on the balance between the viscous forces that deform the drop and the forces that resist deformation when the drop is in equilibrium. In this case, two new parameters were added: matrix and drop elasticities. The first one is part of the forces that induce deformation (viscous forces) while the second is added to the interfacial forces, where  $G'$  is the elastic modulus. Here you can use  $G'$  since shear rates are low ( $< 10 \text{ s}^{-1}$ ), and the first normal stress difference can be approximated by  $2G'$ . Above  $10 \text{ s}^{-1}$  the first normal stress difference is greater than  $2G'$ , but these quantities are proportional to each other. Finally, a break was observed for viscosity ratios greater than 3.5 in polymer blends [36]. Gout first formed a sheet along the flow direction which then broke into smaller daughter droplets along the direction of flow; it was referred to as the "parallel break."

### **1.5. Retraction of Newtonian Drops after Stopping the Flow**

Like the deformation history, the *evolution of the shape of the drop* after stopping the flow contributes significantly to the rheological behavior of the relaxation mixtures. Through observations of the relaxation of a drop after stopping the simple shear rate flow at different amplitudes, the work of Yamane and

colleagues [39] has shown that the shape of a drop is governed to a large extent by *the history of its deformation*. For weakly deformed drops, i.e.,  $\gamma \sim 1$ , drops retract maintaining the shape of an ellipsoid of revolution at all times until it regains its spherical equilibrium shape.



**Figure 1.5.** Diagram of the shape change of a drop under pure shear rate a) seen from above and b) from the side. Adapted from Yamane [39].

For moderate deformations, i.e.,  $2 < \gamma < 3$ , it is shown that, once the flow stops, the drop relaxes into a cylindrical shape before becoming an ellipsoid and finally evolving toward its spherical shape. For deformations on the order of 4, the drop

is deformed into a thin oblate ellipsoid ( $B \ll W < L$ ). It first acquires a cylindrical shape, followed by an altered form prior to an ellipsoid of revolution and, finally, finding its spherical shape. As for the alignment of the drop, it has been observed in the direction perpendicular to the plane of flow, with the angle  $\theta$  remaining constant during the relaxation process. Yamane's observations are shown schematically in Figure 1.5.

These observations permit determination of the interfacial tension during relaxation of drop in an emulsion, with several advantages: The technique can be used on liquids with similar densities and high viscosities, the requirements in equipment are simple; and there is no restriction for the materials, either the drop or the matrix. One of the limitations is that the theoretical models do not take into account the elasticity of the samples. But when compared with the static and dynamic methods, it compares favorably for our purposes.

## **1.6. Coalescence of Drops**

The phenomenon of coalescence of two colliding drops is always preceded by a lapse of time, during which the separation distance between the drops slowly becomes small. This time interval corresponds to drainage of the continuous phase that separates the two drops. When this separation becomes nil, coalescence occur.



It is clear that the interlayer between drops thickness decreases due to drainage, and being is of the order of 10 nm to 100 nm [40]. The rupture of this thin-film can result in a complete or partial coalescence. On the other hand, a bounce is usually observed when the film's draw speed is too slow. The informative and general description of Newtonian drops coalescing is available in several references [41, 42, 43; 44, 45]. The coalescence between droplets has been investigated less extensively than that of bubbles.

There has been only a limited number of studies published about the coalescence of drops in non-Newtonian media, among them Acharya and Ulbrecht [46]. The work by Das and colleagues [47] develops a model for the coalescence of droplets in stirred dispersions involving non-Newtonian polymer solutions. Also, Bazhlekov and colleagues [48,49] have examined the drainage and rupture of the thin Newtonian layer that separates two drops of fluid that meet the “power law” (not Newtonians) model, under the action of a constant force. The main finding seems to be that the critical thickness of the rupture in bubbles, drops, and particles in the fluids are weakly dependent on the “power law” of the dispersed phase.

Similarly, Yildirim and Basaran [50] have studied the deformation and rupture of the stretching bridges between two Newtonian and non-Newtonian liquid disks. The liquid bridge suffers deformation until it breaks when the two disks are

separated. Despite the highly idealized conditions, such studies add to the understanding of film thinning in the context of coalescence.

For sufficiently long times, a probability of collision equal to 1 can be established, and, thus, guaranteeing coalescence. For emulsions, the collision frequency is inversely proportional to the volume fraction of the disperse phase, while the collision time is inversely proportional to the shearing speed. Coalescence also depends on other factors. If the collision time is too short or if the drops are too large, the amount of continuous phase to be removed is too large, and the separation distance will not reach the critical value required for coalescence; subsequently the two drops move away without any changes. Three models have been proposed to deal with effects for maximum drop size achievable through coalescence, with respect to the mobility of the interface: Immobile interface (IMI), partially mobile interface (PMI) and fully mobile interface (FMI). Thus, because not all collisions lead to coalescence, the rate of coalescence in the emulsion is determined by the product of the collision frequency of the counted drops and the efficiency of coalescence of the collision droplets.

The review of the literature shows that the study of the behavior of polymer mixtures in the pure flow has been the subject of a large number of experimental

works. This is probably due to the experimental facilities with this type of flow; this opposite situation for an elongational flow.

## **1.7. Chapter Conclusions**

In this Chapter, a non-exhaustive summary of state of the art was presented for the development of this work on the evolution of the morphology of emulsions, in particular of the deformation, rupture, retraction, and coalescence of Newtonian and non-Newtonian systems. In general terms, the state of the art addresses many important phenomena and variables for understanding the dynamics of population of drops in a continuum medium. The present supplements previous works along the lines referred to as environmentally not so "simple": the mixture of two Newtonian liquids, which are emulsified at very high fractions.

In the literature, the study of systems in simple shear flow presents several models, as presented in this Chapter, but few of relevance to the behavior of drops in bulk (highly concentrated emulsions). However, for highly concentrated emulsions, the deformation, coalescence and breakup of a drop are still poorly understood phenomena, a complicated issue since it may depend on the type of system, i.e., Newtonian or non-Newtonian, the presence of surfactants, confinement and shearing rates.

## 1.8. References

- [1] Taylor GI. The formation of emulsions in definable fields of flow. *Proc. R. Soc. Lond. A.* 1934 Oct 1;146(858):501-23.
- [2] Taylor GI. The viscosity of a fluid containing small drops of another fluid. *Proc. R. Soc. Lond. A.* 1932 Oct 1;138(834):41-8.
- [3] Tomotika S. On the instability of a cylindrical thread of a viscous liquid surrounded by another viscous fluid. *Proc. R. Soc. Lond. A.* 1935 Jun 1;150(870):322-37.
- [4] Grace HP. Dispersion phenomena in high viscosity immiscible fluid systems and application of static mixers as dispersion devices in such systems. *Chemical Engineering Communications.* 1982 Mar 1;14(3-6):225-77.
- [5] Stone HA, Leal LG. The influence of initial deformation on drop breakup in subcritical time-dependent flows at low Reynolds numbers. *Journal of Fluid Mechanics.* 1989 Sep;206:223-63.
- [6] Bentley BJ, Leal LG. An experimental investigation of drop deformation and breakup in steady, two-dimensional linear flows. *Journal of Fluid Mechanics.* 1986 Jun;167:241-83.
- [7] Cox RG. The deformation of a drop in a general time-dependent fluid flow. *Journal of Fluid Mechanics.* 1969 Jul;37(3):601-23.
- [8] Torza S, Cox RG, Mason SG. Particle motions in sheared suspensions XXVII. Transient and steady deformation and burst of liquid drops. *Journal of Colloid and Interface Science.* 1972 Feb 1;38(2):395-411.
- [9] Maffettone PL, Minale M. Equation of change for ellipsoidal drops in viscous flow. *Journal of Non-Newtonian Fluid Mechanics.* 1998 Aug 1;78(2-3):227-41.
- [10] Rumscheidt FD, Mason SG. Particle motions in sheared suspensions XII. Deformation and burst of fluid drops in shear and hyperbolic flow. *Journal of Colloid Science.* 1961 Jun 1;16(3):238-61.
- [11] Cerf-Ducastel B, Murphy C. fMRI activation in response to odorants orally delivered in aqueous solutions. *Chemical Senses.* 2001 Jul 1;26(6):625-37.
- [12] De Bruijn RA. Tipstreaming of drops in simple shear flows. *Chemical Engineering Science.* 1993 Jan 1;48(2):277-84.
- [13] De Bruijn RA. Deformation and breakup of drops in simple shear flows (Doctoral dissertation, Technische Universiteit Eindhoven).
- [14] Bazhlekov IB, Anderson PD, Meijer HE. Numerical investigation of the effect of insoluble surfactants on drop deformation and breakup in simple shear flow. *Journal of Colloid and Interface Science.* 2006 Jun 1;298(1):369-94.

- [15] Feigl K, Megias-Alguacil D, Fischer P, Windhab EJ. Simulation and experiments of droplet deformation and orientation in simple shear flow with surfactants. *Chemical Engineering Science*. 2007 Jun 1;62(12):3242-58.
- [16] Cristini V, Guido S, Alfani A, Bławzdziwicz J, Loewenberg M. Drop breakup and fragment size distribution in shear flow. *Journal of Rheology*. 2003 Sep;47(5):1283-98.
- [17] Changzhi L, Liejin GU. Experimental study of drop deformation and breakup in simple shear flows. *Chinese Journal of Chemical Engineering*. 2007 Feb 1;15(1):1-5.
- [18] Zhao X. Drop breakup in dilute Newtonian emulsions in simple shear flow: New drop breakup mechanisms. *Journal of Rheology*. 2007 May;51(3):367-92.
- [19] Vananroye A, Van Puyvelde P, Moldenaers P. Structure development in confined polymer blends: steady-state shear flow and relaxation. *Langmuir*. 2006 Feb 28;22(5):2273-80.
- [20] Vananroye A, Van Puyvelde P, Moldenaers P. Effect of confinement on droplet breakup in sheared emulsions. *Langmuir*. 2006 Apr 25;22(9):3972-4.
- [21] Sibillo V, Pasquariello G, Simeone M, Cristini V, Guido S. Drop deformation in microconfined shear flow. *Physical review letters*. 2006 Aug 2;97(5):054502.
- [22] Gauthier F, Goldsmith HL, Mason SG. Particle motions in non-Newtonian media. II. Poiseuille flow. *Transactions of the Society of Rheology*. 1971 Jul;15(2):297-330.
- [23] Flumerfelt RW. Drop Breakup in Simple Shear Fields of Viscoelastic Fluids. *Industrial & Engineering Chemistry Fundamentals*. 1972 Aug;11(3):312-8.
- [24] Elmendorp JJ, Maalcke RJ. A study on polymer blending microrheology: Part 1. *Polymer Engineering & Science*. 1985 Nov;25(16):1041-7.
- [25] Mighri F, Carreau PJ, Aji A. Influence of elastic properties on drop deformation and breakup in shear flow. *Journal of Rheology*. 1998 Nov;42(6):1477-90.
- [26] Sibillo V, Guido S, Greco F, Maffettone PL. Single drop dynamics under shearing flow in systems with a viscoelastic phase. In *Macromolecular Symposia 2005 Aug* (Vol. 228, No. 1, pp. 31-40). Weinheim: WILEY-VCH Verlag.
- [27] Guido S, Simeone M, Greco F. Effects of matrix viscoelasticity on drop deformation in dilute polymer blends under slow shear flow. *Polymer*. 2003 Jan 1;44(2):467-71.
- [28] Lerdwijitjarud W, Sirivat A, Larson RG. Influence of dispersed-phase elasticity on steady-state deformation and breakup of droplets in simple shearing flow of immiscible polymer blends. *Journal of Rheology*. 2004 Jul;48(4):843-62.
- [29] Milliken WJ, Leal LG. Deformation and breakup of viscoelastic drops in planar extensional flows. *Journal of Non-newtonian Fluid Mechanics*. 1991 Nov 15;40(3):355-79.
- [30] Tsakalos VT, Navard P, Peuvrel-Disdier E. Deformation and breakup mechanisms of single drops during shear. *Journal of Rheology*. 1998 Nov;42(6):1403-17.

- [31] Varanasi PP, Ryan ME, Stroeve P. Experimental-Study on the Breakup of Model Viscoelastic Drops in Uniform Shear-Flow. *Industrial & Engineering Chemistry Research*. 1994;33(7):1858-66.
- [32] Greco F. Drop deformation for non-Newtonian fluids in slow flows. *Journal of Non-Newtonian Fluid Mechanics*. 2002;1(107):111-31.
- [34] Li H, Sundararaj U. Does drop size affect the mechanism of viscoelastic drop breakup?. *Physics of Fluids*. 2008 May;20(5):053101.
- [35] Levitt L, Macosko CW, Pearson SD. Influence of Normal Stress Difference on Polymer Drop Deformation. *Polymer Engineering and Science*. 1996;36(12):1647-55.
- [36] Tanpaiboonkul P, Lerdwijitjarud W, Sirivat A, Larson RG. Transient and steady-state deformations and breakup of dispersed-phase droplets of immiscible polymer blends in steady shear flow. *Polymer*. 2007;13(48):3822-35.
- [37] Ghodgaonkar PG, Sundararaj U. Prediction of Dispersed Phase Drop Diameter in Polymer Blends-The Effect of Elasticity. *Polymer Engineering and Science*. 1996;36(12):1656-65.
- [38] Lin B, Mighri F, Huneault MA, Sundararaj U. Parallel breakup of polymer drops under simple shear. *Macromolecular Rapid Communications*. 2003.
- [39] Yamane H, Takahashi M, Hayashi R, Okamoto K, Kashihara H, Masuda T. Observation of deformation and recovery of poly (isobutylene) droplet in a poly (isobutylene)/poly (dimethyl siloxane) blend after application of step shear strain. *Journal of Rheology*. 1998 May;42:567-80.
- [40] Scheele GT, Leng DE. An experimental study of factors which promote coalescence of two colliding drops suspended in water-I. *Chemical Engineering Science*. 1971 Nov 1;26(11):1867-79.
- [41] Kintner RC. Drop phenomena affecting liquid extraction. In *Advances in Chemical Engineering* 1964 Jan 1 (Vol. 4, pp. 51-94). Academic Press.
- [42] Tavlarides LL, Stamatoudis M. The analysis of interphase reactions and mass transfer in liquid-liquid dispersions. In *Advances in Chemical Engineering* 1981 Jan 1 (Vol. 11, pp. 199-273). Academic Press.
- [43] Godfrey JC, Hanson C. Liquid-liquid systems. *Hetbook of Multiphase Systems*, Ed. G. Hestroni, Hemisphere. 1982.
- [44] Grace JR. Hydrodynamics of liquid drops in immiscible liquids. *Handbook of Fluids in Motion*. 1983;38.
- [45] Möbius D, Miller R, editors. *Proteins at liquid interfaces*. Elsevier; 1998 Apr 24.
- [46] Acharya A, Ulbrecht JJ. Note on the influence of viscoelasticity on the coalescence rate of bubbles and drops. *AIChE Journal*. 1978 Mar;24(2):348-51.

- [47] Das PK, Kumar R, Ramkrishna D. Coalescence of drops in stirred dispersion. A white noise model for coalescence. *Chemical Engineering Science*. 1987 Jan 1;42(2):213-20.
- [48] Bazhlekov IB, Chesters AK, van de Vosse FN. The effect of the dispersed to continuous-phase viscosity ratio on film drainage between interacting drops. *International Journal of Multiphase Flow*. 2000;26(445):466.
- [49] Bazhlekov IB, van de Vosse FN. Multiple time step approach for numerical simulation of non-Newtonian drop coalescence. In *Recent Advances in Numerical Methods and Applications II 1999* (pp. 824-832).
- [50] Yildirim OE, Basaran OA. Deformation and breakup of stretching bridges of Newtonian and shear-thinning liquids: comparison of one- and two-dimensional models. *Chemical Engineering Science*. 2001;1(56):211-33.
- [51] Van Puyvelde P, Moldenaers P. Chapter. 19. Rheology-morphology relationship in immiscible polymer blends. In: Guo Q. *Polymer Morphology: Principles, Characterization, and Processing*. John Wiley & Sons; 2016 Mar 21.

## ***Chapter 2: Experimental setup and methods***

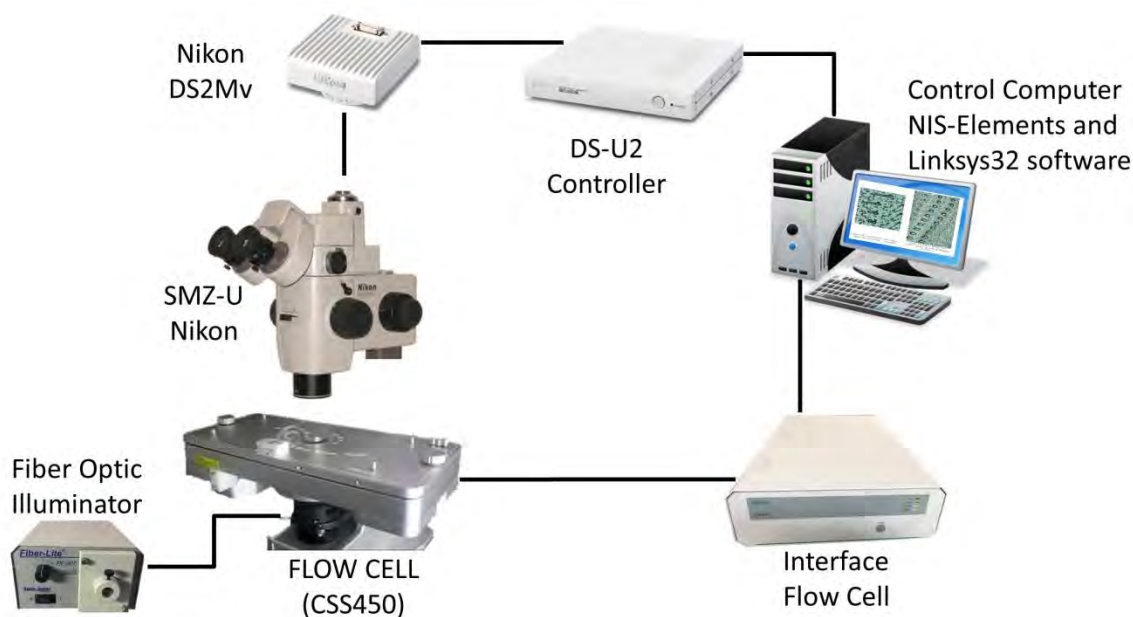
### **2.1. Overview of Experimental Setup**

The experimental setup used for the optical characterization of the emulsion is described in the following Sections. The main components of the experimental setup are: a pneumatically levitated table (Newport LW3036B-OPT) to reduce environmental vibrations, a flow cell (CSS450-Linkam), a Nikon SMZ-U microscope, and two cameras, one Nikon DS-2Vm and another PL-B953U (Pixelink Digital). In Figure 2.1 the arrangement of the experimental setup is shown. The main component to induced changes on the emulsion microstructure and for its statistical characterization is the CSS450 flow cell (Linkam).



## 2.2. The Flow Cell

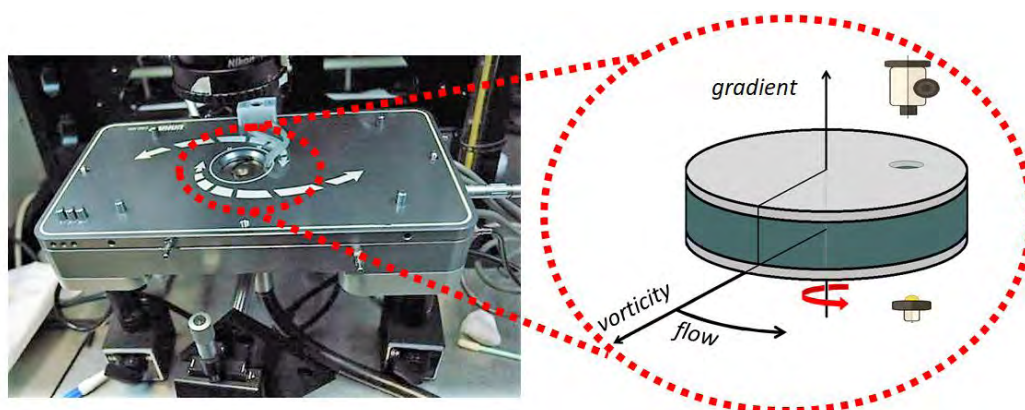
The Linkam flow cell (CSS450-LINKAM) applies a shear flow on a sample while simultaneously allowing the visualization of its microstructure. By operating in real time, one can directly observe the dynamics of the structure of the emulsion through the microscope. The cell carries out all experiments with a temperature precisely controlled and maintained at 30 °C. The ceramic plates surrounding the flow cell allows a wide range of temperatures: -80 to 450 °C. The separation of the flow cell walls can be varied from 5 to 2500  $\mu\text{m}$ .



**Figure 2.1.** Schematic setup of the experimental.

The angular speed of the shearing plate can vary within a range of 0.001 to 10 rad/s with a resolution of 25000 steps/rev. The software use for the control of the cell and the interface is Linksys®. In general, with this cell it is possible to

study the evolution of the microstructure of complex fluids to high degree of detail: for example, the phase separation of binary fluids at long times, the mixture induced by flow and the separation of polymer mixtures, defects of liquid crystal dynamics, aggregation of red blood cells and its deformation by fluxes, among many other possible materials.



**Figure 2.2.** Schematic of the device of parallel disks geometry with a diameter of 36 mm and a gap of 0.1 mm. The observation plane is described by the velocity-vorticity axes. The motion of the lower disc imposes a approximate simple shearing field on the sample.

Figure 2.2 shows a diagram of the flow cell and the axes of the flow, the velocity gradient, and the vorticity. The cell consists of two highly polished parallel, quartz discs. Each disc is in thermal contact with an independently controlled pure silver heater that uses platinum resistors sensitive to 0.01 °C. The lower disc, on which the material sample is placed, applies a shearing flow, of several types: oscillating, constant or progressive modes. These flows are programmed into the Linksys® software. To facilitate the diversity of samples the space between the two disks can be established with great precision from 5 to 2500  $\mu\text{m}$ .

The separation between the quartz plates was kept constant during all the experiments at 0.1 mm (100  $\mu\text{m}$ ). The rotation applied to the lower disc for the full set of experiments here reported was within 0.01 to 0.06 rad/s, which is equivalent to a range of shear rates from 0.75 to 4.5  $\text{s}^{-1}$ . All images were captured in the velocity-vorticity plane, with a resolution of 1155 x 867 pixels, through a 2 mm observation window, located at a radial position of 7.5 mm away from the center of rotation.

### **2.3. Description of Additional Equipment**

- Nikon SMZ-U Stereographic Microscope.

The microscope has a magnification ratio of 10:1, which covers a range of 0.75x to 7.5x, and reduces the need to change lenses frequently. The relationship used in the present work is 7.5x, with a maximum resolution of about 3-5  $\mu\text{m}$  for the complete field of view. This resolution matches the size of pixel (diagonal length) on the CCD. An interchangeable 1.0x objective lens is also used. The depth of field is approximately  $\sim 100 \mu\text{m}$ .

- Omni ES Macro Homogenizer.

It is a powerful 1800 W homogenizer that is compatible with a wide range of generator tips. In this work, the "fine" saw tooth tip — 10 mm diameter, 95 mm

long, stainless steel #316 probe— was used (SKU#15051), as shown in Figure 2.3. This homogenizer is ideally suited for mixing and creating stable emulsions. The homogenizer mixing capacity is between 1.5 ml to 100 ml.



**Figure 2.3.** Omni and tip homogenizer used in the emulsion realization.

- Ares Rheometer G.1 with temperature control by the circulated bathroom.

The ARES rheometer (Advanced Rheometric Expansion System) is a versatile rheometer, which has a motor with HR (High Resolution) displacements and an FRT (Force Rebalance Transducer) transducer. The rheometer is suitable for characterizing a wide variety of complex low- to high-viscosity materials, such as mixtures, suspensions, emulsions, among many others.

The rheometer can use a large variety of possible probe geometries, such as parallel plates, cone and plate, concentric cylinders, among others. The temperature control cover a range from -10 to 150 °C, which can be carried out in

three different ways: one by a water recirculation bath, by a Peltier dish and by forced convection. The latter is carried out with air convection and is used mainly for melts (plastics) and solids, up to a value of 600 °C.

The possible measurement that can be performed are the following: continuous shear measurements, dynamic shearing oscillations, transient shear rate tests (compliant and stress relaxation), parallel superposition (non-linear) experiments, torsion experiments and deformation measurements in a wide variety of materials covering from low to highly viscous solids. The rheometer is controlled by the Orchestrator® software.

- Digital camera DS-2Mv.

The DS-2Mv digital camera features a 2 megapixel CCD (1600 x 1200 pixels) that can display motionless SXGA motion pictures at 15 fps (max. 30 fps).

- Pixelink PL-B953U digital camera.

The PL-B953U is a high-performance 0.8-megapixel (1024 x 768) monochrome CCD camera designed for a wide range of industrial imaging applications. This camera uses a USB 2.0 digital interface for transferring images and is based on the Sony ICX204 progressive scan sensor with a 1/3" optical format and a pixel pitch of

4.65  $\mu\text{m}$ . External activation and two general purpose outputs give users the flexibility to synchronize the camera with its processes and lighting conditions.

## 2.4. Preparation of the Emulsion

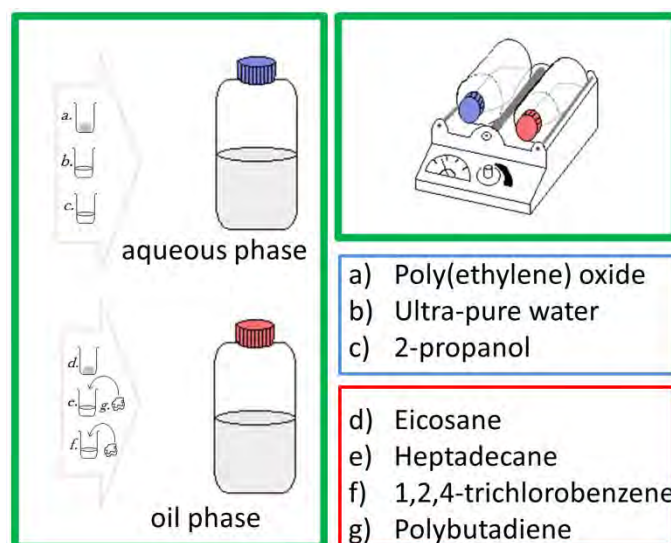
The methodology for the preparation of these emulsions and their characterization is carried out in four stages. The first stage is the preparation of the oil phase and the water phase. The objective here is having a water and oil phases *with control of density and viscosity independently* for each one. The second is the creation of the emulsion. The third is the characterization of the basic rheological properties of each phase, and the fourth is the optical characterization of the structure of the emulsion in the flow cell, which is detailed in the following paragraphs. The immiscibility of the two phases was visually validated by monitoring the diameter of a single drop immersed in the matrix fluid. No significant variation was detected in the time scale of the experiments, which guarantees that the fluids can be considered immiscible for the scope of this work.

The use of the mixture of heptadecane and eicosane (linear alkanes) in this work is a result of previous works in the Optical-Rheology Laboratory at the Instituto de Investigaciones en Materiales, of the National University of Mexico (UNAM). This emulsion can be used as a simple model capable of simulating the viscous behavior

of Mexican crude oils. In addition and in contrast to crude oil water mixtures, this model mixture is completely transparent allowing an optical characterization of its micro-structure, which can be used to predict the rheological/morphological properties of crude oil. The main advantage of this model system is that is well characterized and is reproducible in any laboratory. Although, only the morphology of a model emulsion is studied in the following Chapters.

The first step, the aqueous phase is prepared (w/W) from 10  $\mu\text{M}$  polyethylene oxide polymer (PEO)  $M_v \sim 1000000$  (Sigma-Aldrich CAS#372781), in 97 % deionized water (18.2  $\text{M}\Omega\cdot\text{cm}$ ;  $\rho = 0.997 \text{ g/mL}$ ) and 3 % of a low molecular weight alcohol isopropanol 2-propanol (Sigma-Aldrich CAS#190764,  $\geq 99.5 \%$  reagent grade); the viscosity of the sample in control mainly by the use of the polymer and its density can be adjusted by the fraction of alcohol. The oil phase is prepared as a mixture of alkanes —linear hydrocarbons: eicosane (Sigma-Aldrich CAS#219274), and heptadecane (Sigma-Aldrich CAS#128503). 1,2,4-trichlorobenzene (Sigma-Aldrich CAS#132047) is used to modified its density and be adjusted to that of the aqueous phase. Polybutadiene (Sigma-Aldrich CAS#181382) a high molecular weight polymer ( $M_w \sim 200,000$ ), adjust the viscosity of the oil phase. The preparation of the oil phase begins by mixing 7.56 % of eicosane with 39.69 % of heptadecane in a glass bottle (Kirax®) maintaining a temperature of 30 °C and later adding 46.5 % of trichlorobenzene and 6.25 % of polybutadiene ( $M_n \sim 200000$ ).

The second stage consists of placing each phase independently at constant rotation on a roller mixer at a speed of 3 rpm for a minimum of 48 h, to ensure a homogeneous mixture of each phase, as illustrated in Figure 2.4.

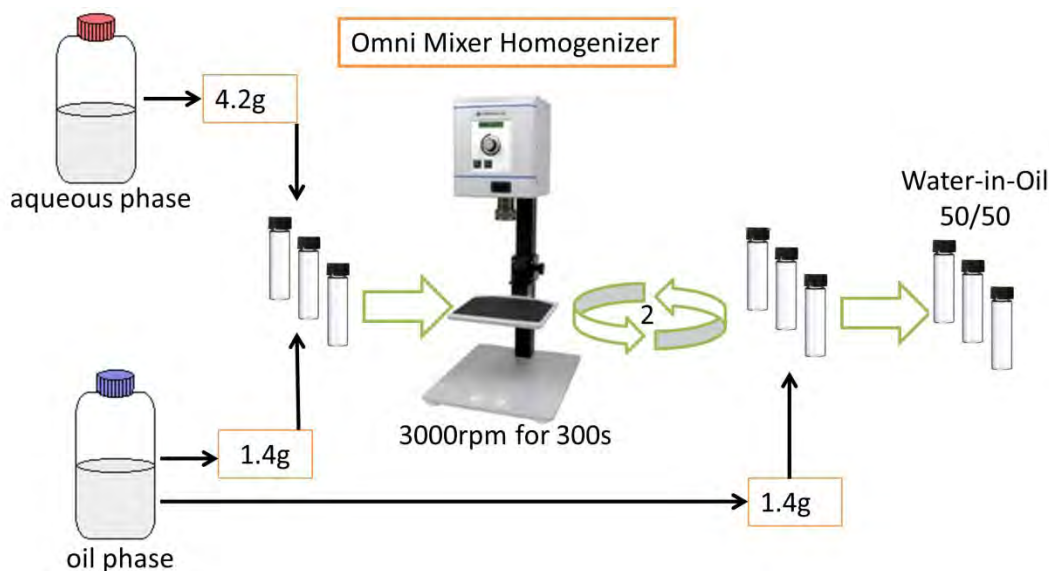


**Figure 2.4.** Scheme of the elaboration process of the emulsion. The bottles with a blue cover refer to the aqueous phase, and those with a red cover refer to the oil phase.

The densities of the two phases were measured and differed in less than  $0.001 \text{ g}\cdot\text{cm}^3$ . The next step is the preparation of the emulsion: It is split into three transparent glass containers, with 4.2 g of the oil phase and 1.4 g of the aqueous phase for the first batch. It is mixed in the Omni homogenizer, with the 10 mmx95 mm specimen (SKU#15051) at a speed of 3000 rpm, for 300 s. Subsequently an extra 1.4 g of the aqueous phase is added and again stirred at 3000 rpm, for 300 s. The procedure is repeated until completion of the 50/50 % ratio required by the emulsion. All batches are mixed into a single one at 3000 rpm during 300 s at a temperature of  $30 \text{ }^\circ\text{C}$  set by an external water bath. The emulsion



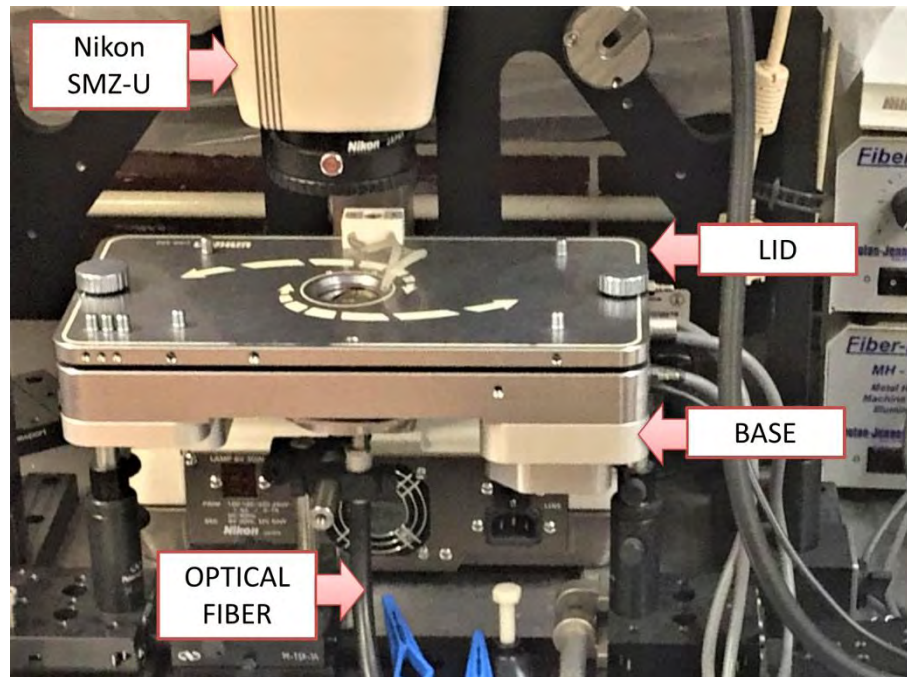
is stored in glass tubes of 5mm diameter and 500 mm in length, in an oven at a temperature of 30 °C, left for 48 h in a vertical position. The above procedure is to ensure the homogeneity of the emulsion and to ensure that the possible bubbles disappear. The procedure is shown in Figure 2.5.



**Figure 2.5.** Diagram of the execution of the aqueous phase and oil phase in the Omni homogenizer. Moreover, storage in tubes at a constant temperature of 30 °C for 48 h.

The third stage is the characterization with the ARES rheometer (Rheometric Scientific), of the viscosity for each phase. Applying a constant shear rate (within a range of deformation speed from 0.1 to 10 s<sup>-1</sup> was taken, with five stress measurements per decade) the viscosity of the oil phase is  $\eta_{oil} = 2.08 \text{ Pa} \cdot \text{s}$  and for water:  $\eta_{water} = 0.57 \text{ Pa} \cdot \text{s}$ . It is also desirable to study the stability of the emulsion under flowing conditions, for which the model emulsion will be subjected to a shearing flow with constant speed and measure *its properties at different times*.

The viscosity tests were constant with the shear applied, and the first differences of the normal stresses were so small that it was out of the sensitivity of the equipment.



**Figure 2.6.** The experimental arrangement, Linkam CSS-450 flow cell, Nikon SMZ-U microscope, and fiber optic lighting.

The fourth step is the optical characterization of the emulsion under flow conditions, using an experimental arrangement like the one in Figure 2.6. With this arrangement is possible to determine drop diameters (Chapter 3) for a large set of drops, thus observe the *evolution of the microstructure* under the influence of simple shear flows (Chapter 4) and *measure the interfacial tension as a property of the emulsion* using a dynamical technique (Chapter 5) in comparison to the conventional techniques that evaluate this property using an isolated drop.

Image of emulsions were captured using two different cameras: a digital Nikon DS-2Mv (Nikon Digital Sight) which is controlled by the software NIS-Elements, and the Pixelink PL-B953U which is controlled with its own software. Subsequently, the characteristics of each part of the experimental arrangement are specified. The software used allows capturing sequences of image, which will then be analyzed by the Open ImageJ (free) software.

## **2.5. Placement of the Sample in the Cell**

The emulsion is produced and stored for 48 h at a temperature of 30 °C. The next step of loading of the sample on the flow cell follows. A sample of ~0.4 ml of the emulsion is placed on the lower quartz plate of the flow cell (A simple calculation of the volume of sample to be used is described in Appendix A). Afterward, the top cover is placed on, and the separation distance between quartz plates is reduced to the working distance of 100  $\mu\text{m}$ . The sample is squeezed very slowly with the vertical movement of the plate above; squeezing rate of 0.1 mm for every 60 s approximately. Thus, no residual load stresses are generated in the sample and homogeneity is maintained. When the separation distance of 100  $\mu\text{m}$  is reached, the sample is left to stand for ~600 s (with no flow). Subsequently, a shear rate of  $0.075 \text{ s}^{-1}$  is applied for a time lapse of ~500 s. In this way, the residual stress that could have been generated by lowering the cell cover is sought to disappear, and

is called the *pre-shearing stage*. Afterward, the loaded sample can be studied in a reproducible manner.

The *experimental shear rate ramp* is subsequently applied starting with the shear rate step of a value of  $\dot{\gamma} = 0.75 \text{ s}^{-1}$ , which is maintained for a time  $t \sim 400 \text{ s}$ . This time lapse proves to be sufficiently long to ensure that the individual properties of the droplets (and the emulsion) reach a steady state. After the applied steady flow, a brief *rest time* is inserted —for about  $\sim 18 \text{ s}$ — between flow steps of the ramp. This rest-time is long enough for capturing the emulsion images used to evaluate its microstructure just generated by the flow, given that this time was sufficiently long for all drops to return to their spherical equilibrium state.

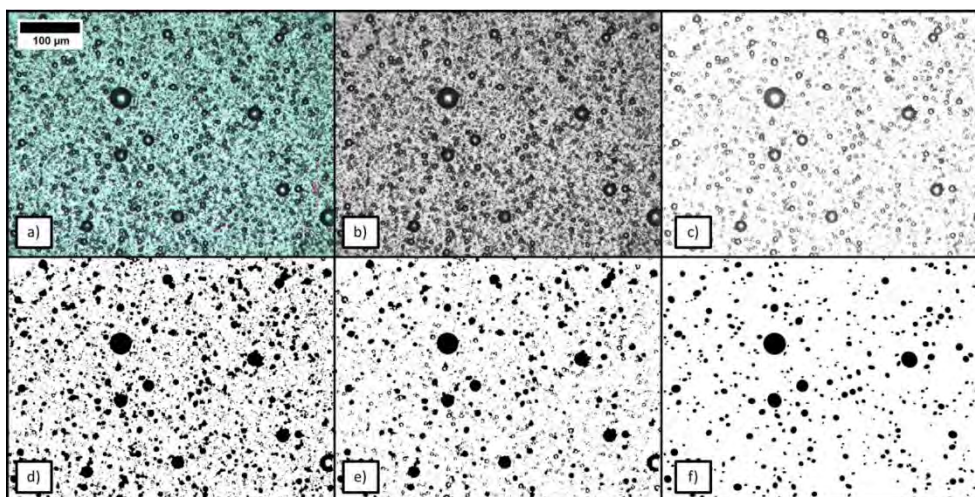
After the first brief rest-time, the intensity of the flow field is increased to  $\dot{\gamma} = 1.50 \text{ s}^{-1}$ , and this procedure is repeated until a shear rate of  $\dot{\gamma} = 4.5 \text{ s}^{-1}$  is attained. After each increase in shear rate, the flow was stopped for a rest-time, allowing droplets to relax. All images for the statistical analysis of the size distribution of the dispersed phase were recorded during the rest-times. Captured images during the no flow states of the sample are characterized by values of the shear rate previous to the rest-time. The main criteria been that, after cessation of the flow, drops relax their elongation but hardly anything else changes: no coalescence, rupture or accretion of drops appear to be significant.

To evaluate the influence of the brief rest-time on the population drops, and consequently in its statistical analysis, images were taken of two separate experiments. No significant differences were found in the evolution of the droplet size distribution during the no-flow condition, which allows us to infer the observed size distribution of drops is due mainly to the flow field previously applied.

Additional tests were carried out to evaluate the second most important property of the emulsion: the interfacial tension, which is of the order of 0.11 mN/m, as explained in Chapter 5. In these experiments the retraction of a flow induced elongation of a drop was measured, considering several environments: when the test drop is surrounded by nearby equal size drops, and when the retraction does not appear to modify the nearby environment.

## **2.6. Image Processing Technique**

Several techniques of image analysis have been used in each captured image to automatically and manually detect the contour of each drop, either when they are at rest or in motion (retraction). The necessary steps are: the segmentation of images, the detection of edges and the identification of the best layer of focus of each drop. These steps were implemented as a *macro standard call* for image analysis routines from the library of the ImageJ software package.



**Figure 2.7.** Description of the image processing procedure. a) the captured image is shown, 1155x867 px, RGB b) Grayscale image 8-bit, c) Background subtraction, d) Segmentation Threshold and hole filling, e) Binary image. And f) segmentation with watershed algorithm and subtraction smallest pixels.

The main advantage of this methodology is that it allows a significant amount of data to be processed, generally corresponding to a few thousand drops, which would be a cumbersome task if it is done entirely manually. An example of image processing is presented in Figure 2.7.

In Figure 2.7a, an image of the emulsion taken during the no-flow rest-time is shown. Figure 2.7b corresponds to the grayscale image of 8-bit. Figure 2.7c the brightness and contrasts are optimally tuned, Figure 2.7d shows the image with segmentation (Threshold) of the contours of each drop and hole filling, identified by the image processing (black circles). Figure 2.7e corresponds to binary image and Figure 2.7f correspond to watershed algorithm; this is used in image processing primarily for segmentation of the edges. It can be seen that most of the

drops that appear “in focus” on the image, without formatting, are detected well after this processing steps.

In order to identify, delimit and count drops on an image, a “macro” program is created in the ImageJ program, which facilitates repeating a sequence of operations on digital images. It starts from an RGB image taken with the Nikon microscope or DS-2mv camera, all three color channels are separated, and binary converted to a grey scale image; the binary image is subsequently process to optimize drop contours, to determine accurately size and shape prior to counting; and finally, the count is made.

Converting the RGB image into a binary image provides the software (the image with the ImageJ® program and convert it to an 8-bit "Image/Type/8-bit" ; see Figure 2.7b). with an image that more clearly defines edges of objects. This image is further processed to clean background noise. That is, the intensity for pixels that conform a drop is set by "Image/adjust/thresholding"; by setting a range of possible values for each pixel intensity from 0 to 90. In this manner a binary image is obtained where the chosen pixels (of the drop) now have values of 255 (white) or 0 (black) continuum liquid; see Figure 2.7e.

Because the image is produced with a bright field illumination, in order to enhance the location of the edge of the drop, then the central portion of each drop

is essentially a bright spot —a rather extended region proportional to the drop size. Thus, the next steps requires to convert drops, filling the central spot "with the instruction "Fill Holes" to fill gaps. Subsequently the "Watershed" instruction is use to separate some very small drops close to the environment of larger drops ; see Figure 2.7e-f. In the Process/Binary menu, it shows the modifications (procedures or subroutines) carried out with the image; that is, we start with Fill Holes, to fill gaps, Watershed to separate some small drops in the environment of larger drops.

Subsequently, the data for histograms is prepared. Only drops that have an specific range of size and an acceptable degree of roundness are taken into account. Shape of drops that deviate significantly from spherical, are due most frequently to superposition the images of various drop of smaller size. Hence those "deviatoric drops" are discarded, for no accurate size can be assigned. The counting technique corresponds to the "Analyze/Analyze Particle" menu where, after selecting the range of size and circularity, a table of drops is obtained, accompanied by a new "Overlay Masks" image with the counted drops.

Automate the count: After recording all processing steps with "Macro Recorder", from "Plugins/Macros/Record", prior to counting, the sequence of steps can be repeated for any image ("File/Open/...") file. That is, we convert it to a binary image,



we make the modifications favorable to our objective. Each of the actions we perform is recorded in "Recorder" separated by a semicolon. At the end of the sequence, press "Create," the "Scrip editor" opens in which we search to modify the "macro." In "Language" we select the "Macro" that shows us the commands, texts, and actions in different colors, which allows us to correct or add actions, by pressing the "Run" key, we search check if the counting sequence is correct.

### ***Chapter 3: Evolution of the size distribution of an emulsion under simple shear flow.***

This Chapter presents the methodology used for the investigation of the evolution of the diameter of droplets of the dispersed phase of an emulsion, due to a stress field generated under simple shear flow. The emphasis is on the mechanisms of coalescence and rupture of drops that modify the distribution of sizes of drops. The methodology is based on the acquisition of images through an optical microscope and a camera. The methodology was tested by studying dense emulsions and presents good reproducibility, as will be shown. All the experiments were carried out with the emulsion described in detail in Chapter 1. The two phases are transparent and well described as Newtonian liquids in the range of shear rates studied for the characterization. The procedure in the image analysis is described in Chapter 2. It is important to emphasize that the proposed

protocol is limited by the optical conditions, in particular, the resolution, which depends on the aperture and the objective used; limitations are also introduced at the time of image digitization, by degradation of image quality due to the turbidity of the first samples, among other criteria.

### **3.1. Brief Theoretical Background**

#### **3.1.1. Introduction**

Emulsions are of great relevance for a variety of applications in food, pharmaceuticals, adhesives, cosmetics, plastics, fertilizers, and petroleum recovery industries, inasmuch as mixtures of fluids provide a wider range of properties in their final products. However, the properties of the mixtures depend, to a great extent, on the microstructure of the emulsion, which is, in turn, the result of the history of the flow. Therefore, most rheological properties must be considered as dynamical properties, which may depend on the structure of the emulsion in a nonlinear manner.

For emulsions, the time evolution of their rheological properties can depend on a number of factors, such as fluid properties—i.e., the fluid viscosities and the interfacial energy—the particle size and shape, volume fractions of the phases, and other subtler effects, such as the anisotropic distribution of particles that the

imposed flow can induce [1]. In the literature, we find studies focused on the effects characterized by important processes, such as the role of coalescence-rupture [2–4] of drops or parameters (e.g., the viscosity ratio [5, 6], the shear rate [7–9], and the volume fraction [10, 11]). Nevertheless, much remains to be explored mainly because a complete understanding of the observed phenomena [12] is still lacking. This is especially relevant when the structure evolution shows multiple well-defined structures as time passes under a flow field, particularly, when global anisotropic structural changes are induced at higher shear rates. Despite the possible relevance of the latter, here, we address the changes in the microstructure of the emulsion at low shear rates and of relevance to the rheology of the emulsion. This behavior corresponds to the low, dimensionless time evolutions induced by slow shearing flows presented in this work.

This Section describes the background for this Chapter. There are many results published on the effects of *the history of shearing flows* (e.g., on the deformation, breakup of a single drop, or coalescence of quasi-equal size drops). The pioneering work of G. I. Taylor [13] about the slight deformation of a single drop establishes experimentally that two dimensionless numbers mainly determine the drop deformation under a linear flow: the *capillary number* and the *viscosity ratio*. Larger capillary numbers induce larger drop deformations, and viscous drops require a

higher shear rate or capillary number in order to deform significantly. The capillary number is given by

$$Ca = \frac{\eta_m R \dot{\gamma}}{\sigma} , \quad (3.1)$$

where  $\eta_m$ ,  $R$ ,  $\dot{\gamma}$  and  $\sigma$  represent the viscosity of the fluid matrix, the radius of the drop, the applied shear rate, and the interfacial tension coefficient between phases, respectively.

The viscosity ratio between the two phases is given by

$$p = \frac{\eta_d}{\eta_m} , \quad (3.2)$$

where  $\eta_d$  is the viscosity of the disperse fluid and  $\eta_m$  is the viscosity of the continuum fluid or matrix.

When studying emulsions under flow (besides deformation of drops), other phenomena can frequently be observed, such as coalescence of drops [4], break up of drops [6], or capture of a rather small drop by another significantly larger drop [14]; that is, the growth by accretion of the larger by addition of smaller drops.

When applying a larger shear rate to the emulsion, these phenomena may be observed and are frequently the main source of the observed dynamical changes of the size distributions of drops. Although, each phenomenon depends most

likely on different physical mechanisms. Under weak flows, coalescence of small, equal-sized drops is observed, and the rupture of drops occurs at higher rates of deformation, especially with low viscosity fluids. Research reporting large induced deformations under shearing flows, even beyond a critical drop size (up to break-up into two or multiple droplets), are given in [15–17]. The growth of drops through the capture of much smaller, nearby droplets—by a mechanism that appears to resemble an Oswald ripening process—can be readily produced but requires a rather broad size distribution, including large drops. Finally, spatially varying distributions of particles induced by flow have been observed as well, but its relation to the former phenomena is less well documented. Here, we attempt to describe a robust technique to evaluate the slow-shear-flow phenomena, which generally modifies the observed rheology of an emulsion in a rather complex and nonlinear manner.

### **3.1.2. Coalescence in slow flows**

Here, the coalescence mechanism occurs mainly in the weakest of flows. During this process, two drops may coalesce if they spend enough time in close proximity. Thus, a dimensionless time,  $\tau$ , indicative of the minimum time required for a high probability of coalescence (or its efficiency) can be calculated as

$$\tau = \dot{\gamma} t_e, \quad (3.3)$$

where  $t_e$  corresponds to the duration of imposed flow of the experiment, while the shear rate,  $\dot{\gamma}$ , is *proportional* to the rate of collisions of drops of a given size. Please note that it is customary to consider Equation (3) as a deformation measure, but here, we prefer to associate the inverse of this dimensionless number to an efficacy or efficiency of coalescence. Dimensionless deformation measures are most appropriate when studying fluids with a homogeneous and continuous microstructure, such as polymer solutions (with an associated characteristic time-scale spectrum), etc. In contrast, for our experiments, a dimensionless time is more closely associated with inverse frequency of events. This may provide a better understanding between the statistics of the drops distributions and the experimental conditions. The inverse time for shear rate is associated here with a value proportional to the frequency of collision of drops and is not relevant as a measure of rate of deformation.

This interpretation allows us to compare different flow regimes, assuming that other present phenomena remain stationary. The proportionality constant for the rate of collisions is a rather complex function of the hydrodynamics of multiple interacting drops. For isolated pairs of drops (i.e., very dilute emulsions), the film

drainage model is frequently used, which is more suited for non-deformable surfaces (i.e., drops of high viscosity) [18,19].

For emulsions, mean field values for the drainage model are difficult to calculate. In contrast, when evaluating the evolution of the size distributions under flow, coalescence between the smallest of drops can be inferred rather easily, because the rate of decrease of frequency for the smallest drops is about twice the rate of increase of frequency of drops with double their volume. The same is true for the larger-size drops of multimodal distribution, as will be shown subsequently. Thus, the coalescence rate can be established by the product of the frequency of the drops' collision times the efficiency of coalescence [20].

For emulsions with a high fraction of the disperse phase —characterized by a broad size distribution and under weak shearing flows— the experimental information is difficult to interpret, due mainly to a high density of very small drops, especially at the onset of the flow. It is also evident that an upper limit to the drop size (spheroidal drops and for a given shear rate) exists when the kinetics of the rupture of the drops competes with the coalescence phenomenon, and the changes of the distribution of small drops vanish almost completely [21]. Given that the capillary number increases for the larger drops, then a maximum size exists, where coalescence dominates and rupture kinetics begin, cancelling each



other out. In the work of Grizzuti and Minale, it is suggested that the two processes coexist in the same system [19–27]. Therefore, a second critical capillary number should be observed —associated with the transition of coalescence to rupture— and defined when drops increasing in size undergo a breakage process [11,12,23,24]. The purpose of this work is to clarify the presence of coalescence and rupture processes under shearing flows by studying the evolution of the drop size distribution of the dispersed phase.

### 3.1.3. Breakup of Droplets under a Shearing Flow

The so-called critical capillary number required for the rupture of a vesicle,  $Ca_{rup}$  appears to depend principally on  $p$  for simple shear flows, as shown by Grace [16] and De Bruijn [17]. A broad set of data for drops deformation and break up, including a large class of two-dimensional (2D)-flows —covering from simple shear up to a purely elongational flow— was provided by Bentley and Leal [28]. More recently, for emulsions subjected to simple shear flows, Jansen [29] has shown that the critical capillary number decreases with increments of the fraction of the disperse phase:  $Ca_{rup}(p, \phi)$ . Droplet-breaking mechanisms and shapes of Newtonian liquid droplets have been extensively studied. If  $Ca \ll 1$ , the drop shape is slightly ellipsoidal, depending on  $p$ , and aligned at an orientation angle of  $45^\circ$  with respect to the direction of flow. As the capillary number increases, the

steady state elongation grows, and the drop rotates aligning itself along the direction of flow. For higher capillary numbers, beyond the critical value, rupture is observed with the breaking mode depending on the viscosity ratio. For  $p < 1$ , the drops assume an elongated highly cusped form, from which small drops (the so-called tip streaming phenomenon) are launched. For  $p$  approximately equal to 1, the central portion of the droplet forms a neck (or necks) followed by the breaking up into two daughter-droplets, with small satellite droplets between them.  $Ca \gg Ca_{rup}$ , droplets are deformed into long, thin filaments that eventually break up through the instability of the capillary wave mechanism. These mechanisms become more complex as the density of disperse phase drops increases.

## **3.2. Materials and Methods**

### **3.2.1. Constituents and preparation of emulsions**

Two immiscible fluids were prepared as the emulsion disperse-continuum components, looking for a pair of liquids with high viscosities and equal densities: an aqueous solution, as the dispersed phase, and a mixture of alkanes. The aqueous solution is (w/W) 10  $\mu$ M polyethylene oxide (with a viscosity-averaged molecular weight of  $M_v \sim 1,000,000$ , Sigma-Aldrich CAS#372781, Sigma-Aldrich, St. Louis, MO, USA) in 97 % ultra-pure water

(resistivity  $\geq 18.2 \text{ M}\Omega\cdot\text{cm}$ ;  $\rho = 0.997 \text{ g/mL}$ ) and 3 % 2-propanol (Sigma-Aldrich CAS#190764,  $\geq 99.5 \%$  Reagent grade). The continuum phase is a mixture of eicosane (Sigma-Aldrich CAS#219274), hepta-decane (Sigma-Aldrich CAS#128503), 1,2,4-trichlorobenzene (Sigma-Aldrich CAS#132047), and polybutadiene (Sigma-Aldrich CAS#181382). The alkane fluid is prepared by first mixing 7.56 % eicosane with 39.69 % heptadecane in a glass bottle, while maintaining it at  $30 \text{ }^\circ\text{C}$ , and then adding 46.5 % 1,2,4-trichlorobenzene and 6.25 % polybutadiene ( $M_n \sim 200,000$ ). The viscosities of the fluids were measured with an ARES G2 Rheometer (TA Instruments, New Castle, DE, USA) using the concentric cylinder geometry. The aqueous phase has a viscosity of  $0.57 \text{ Pa}\cdot\text{s}$  and the continuum phase a viscosity of  $2.08 \text{ Pa}\cdot\text{s}$  at  $30 \text{ }^\circ\text{C}$ ; the viscosity ratio is  $p = 0.27$ . The densities ( $\text{g/cm}^3$ , at  $30 \text{ }^\circ\text{C}$ ) are 0.98 and 0.95 for the aqueous phase and the continuum phase, respectively. By using 2-propanol (aqueous solution) and trichloro-benzene (alkane mixture), the density of the two fluids can be adjusted to minimize sedimentation in the emulsion. The interfacial tension  $\sigma$  was determined by the deformed drop retraction (DDR) method, as described by Guido and Villone [30], using the optical shear cell CSS450, which is the same cell that we use in this work. The measured averaged surface tension is  $0.11 \text{ mN/m}$ , evaluated for a set of 11 drops of aqueous fluid (40 %) in the oil phase. (Chapter 5).

The emulsion was prepared by mixing a 50 wt % oil phase with 50 wt % water phase using an homogenizer (Omni Inc., Kennesaw Georgia, GA, USA) with a generator probe 10 mm × 95 mm fine saw tooth (SKU#15051), spinning at 3000 rpm during 300 s, and at a constant temperature of 30 °C. Afterwards, the emulsion was placed in glass tubes (5 mm inner diameter) at rest for 48 h and at 30 °C. In this way, the stability of the emulsion was visually evaluated after 48 h, ensuring that trapped air bubbles were removed.

The sample of the emulsion “to-be-sheared” was placed on the bottom plate of the flow cell, and the top plate was carefully placed on top, afterwards the plates were slowly compressed (squeezed) to reduce the their separation until reaching a gap of 100 μm. This compression process reduces residual stresses while maintaining the homogeneity of the sample. Following loading, the cell was allowed to relax for a period of ~600 s. All flow experiments started with an initial pre-conditioning of the emulsion to eliminate possible residual stresses by subjecting it to a shear rate of 0.075 s<sup>-1</sup> for ~500 s. During this initial flow, the drop size data was dominated by a large count of very small drops –with diameters below the resolution of the optical arrangement ≤ 5 μm– and no comparison with the drop distribution after the loading of the cell is considered reliable. At this instant, we set  $\tau \equiv 0$ .

Subsequently, a ramp sequence of constant steady shear flows was applied for each sample. Each step of the ramp consisted of a steady flow applied during  $\sim 400$  s, followed by a no-flow rest time of  $\sim 18$  s, sufficiently long for drops to attain a spherical shape. The initial step of the ramp began with a flow of  $\dot{\gamma} = 0.75 \text{ s}^{-1}$ , and subsequent flows stepped up by increments of  $0.75 \text{ s}^{-1}$  up to  $4.5 \text{ s}^{-1}$ .

Toward the end of each steady shear stress —just before the flow was stopped— and a short time after the no-flow condition prevailed, a set of images was taken for the statistical analysis. For all the experiments, the no-flow rest time appears to have a negligible effect on the drop size distributions while facilitating the determination of the size of particles of a quasi-spherical shape. Thus, this multistep history of flow stresses is responsible for the changes in the distribution of drops in the sample. The influence of stopping the flow upon the global dimensionless time ( $\tau = \dot{\gamma} \cdot t_e$ ), as well as the structure of the distribution, can be considered negligible. Here, no inertia effects on the deformation of drops is expected given that the nominal Reynolds number —based on tangential velocity, cell gap, and viscosity of the continuum phase— are within  $3 \times 10^{-6} - 2 \times 10^{-5}$ , for all shear rates.

### 3.2.2. Smooth kernel distribution estimation

The smoothing of all drop size frequency histograms was done with the kernel density technique in order to obtain the probability density function with a known collection of frequency points. Here, the histogram area under the curve is assumed to be 1, and the probability of a drop diameter  $d_i$  corresponds to the area under the curve between those two points  $(d_i, d_i + \Delta d)$ , where  $\Delta d$  is the difference between diameters [31]. This tool provides a quick evaluation of the distribution as a continuous function; the smoothing parameter (*bandwidth*) used in all histograms is 1.25 [32]. We also evaluated the quality of polydispersity for the drop distributions via a polydispersity index based on the average drop size (diameter)  $D_{1,0}$ , the average volume size  $D_{4,3}$ , and the contributions of the tails of the distribution, respectively:

$$d_N = D_{1,0} = \frac{\sum_{i=1}^{\infty} n_i \cdot d_i}{\sum_{i=1}^{\infty} n_i}, \quad (3.4)$$

$$d_V = D_{4,3} = \frac{\sum_{i=1}^{\infty} n_i \cdot d_i^4}{\sum_{i=1}^{\infty} n_i \cdot d_i^3}, \quad (3.5)$$

$$skewness = \frac{n}{(n-1)(n-2)} \sum_{i=1}^n \left( \frac{d_i - \bar{d}}{sd} \right)^3, \quad (3.6)$$

$$kurtosis = \frac{n(n+1)}{(n-1)(n-2)(n-3)} \sum_{i=1}^n \left( \frac{d_i - \bar{d}}{sd} \right)^4 - 3 \frac{(n-1)^2}{(n-2)(n-3)}. \quad (3.7)$$

### 3.2.3. Size Distribution of the initial emulsion

The emulsions use in this work is the initial 50%/50% oil in water system, with no dilution. Figure 3.1 presents images for the pre-shearing phase of the experiment. In these images, many small drops can be observed, although with a high degree of uncertainty about their properties. The cell gap was set always at 100  $\mu\text{m}$ , implying that many small droplets may stack up along the optical path. That is, when using the 100  $\mu\text{m}$  gap it is highly probable that several small drops visually overlap at every pixel of the same image; for a bright field illumination microphotography, multiple scattering by many drops imply an image with almost no light reaching the detector.

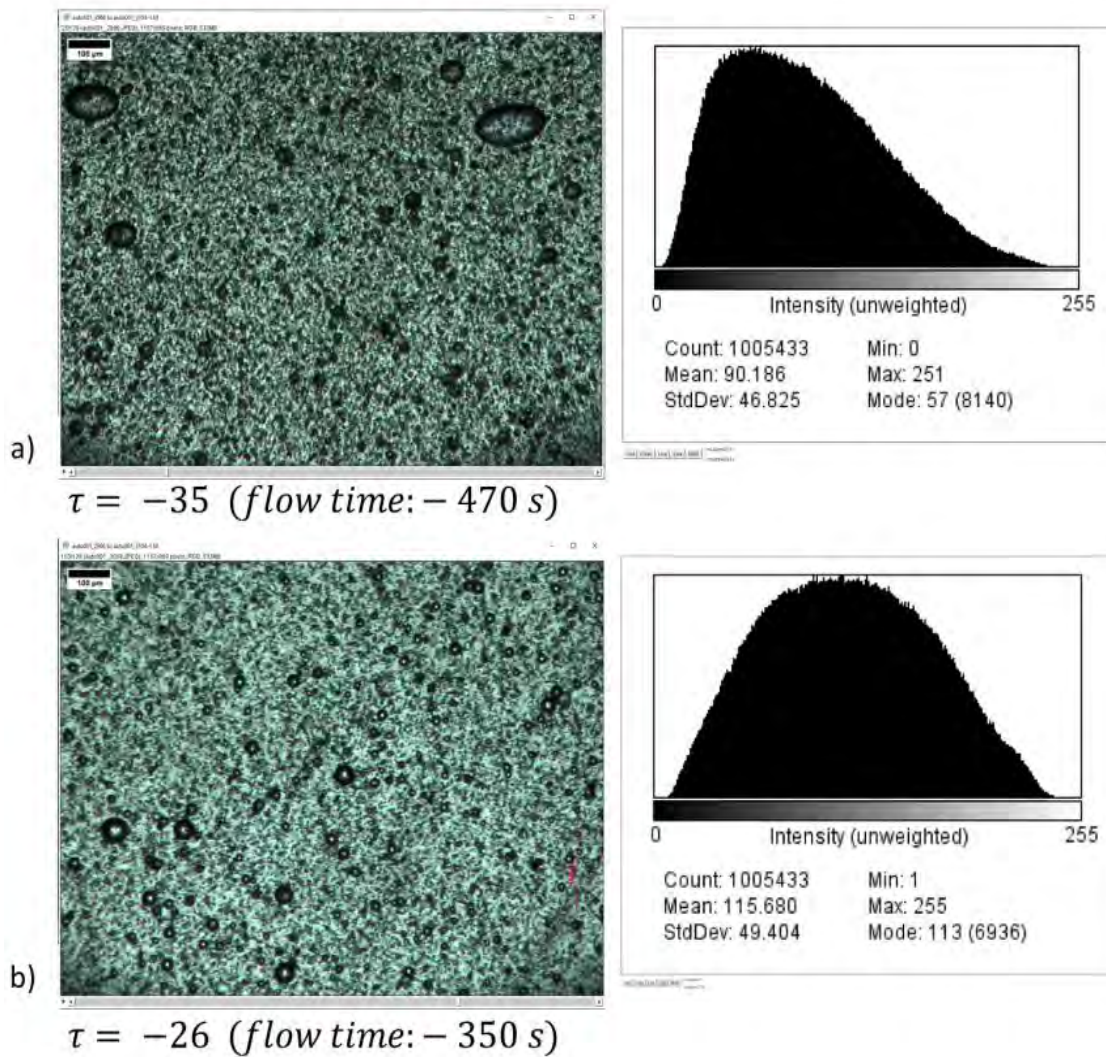
In these cases, histograms show an intensity function with a high dark value at most pixels, which varies slowly across the gray scale; i. e., a broad continuous curve of gray scale values (the initial hump) is the dominant feature of Intensity plots in Figure 3.1. During the pre-shearing phase, a continuous spatial distribution of intensity is always observed with no relationship to specific drops; see right side of Figure 3.1. These intensity distributions imply that most pixels have neighbors with values of the gray scale very close among themselves. Images with this condition become ill-defined for the selection of individual drops or determination of their

dimensions. The drop count algorithm fails to correctly provide reproducible results, as shown in the following Figures. All snapshots are made in the cell (CSS450).

A possible solution for this conundrum is to use a dilute sample, or a cell gap smaller than 100  $\mu\text{m}$ , for improving the determination of the distribution of drops. However, in this work an attempt was made to maintain the same fluid dynamics characteristics for all images and experiments. That is, collected data representing the same (mean) environment for drops, such that interactions —a velocity and stress field— between them does not alter the kinetics (and associated rates) of coalescence, rupture or capture of drops. This mean environment cannot be maintained if gap width or drop densities are modified during the experiment.

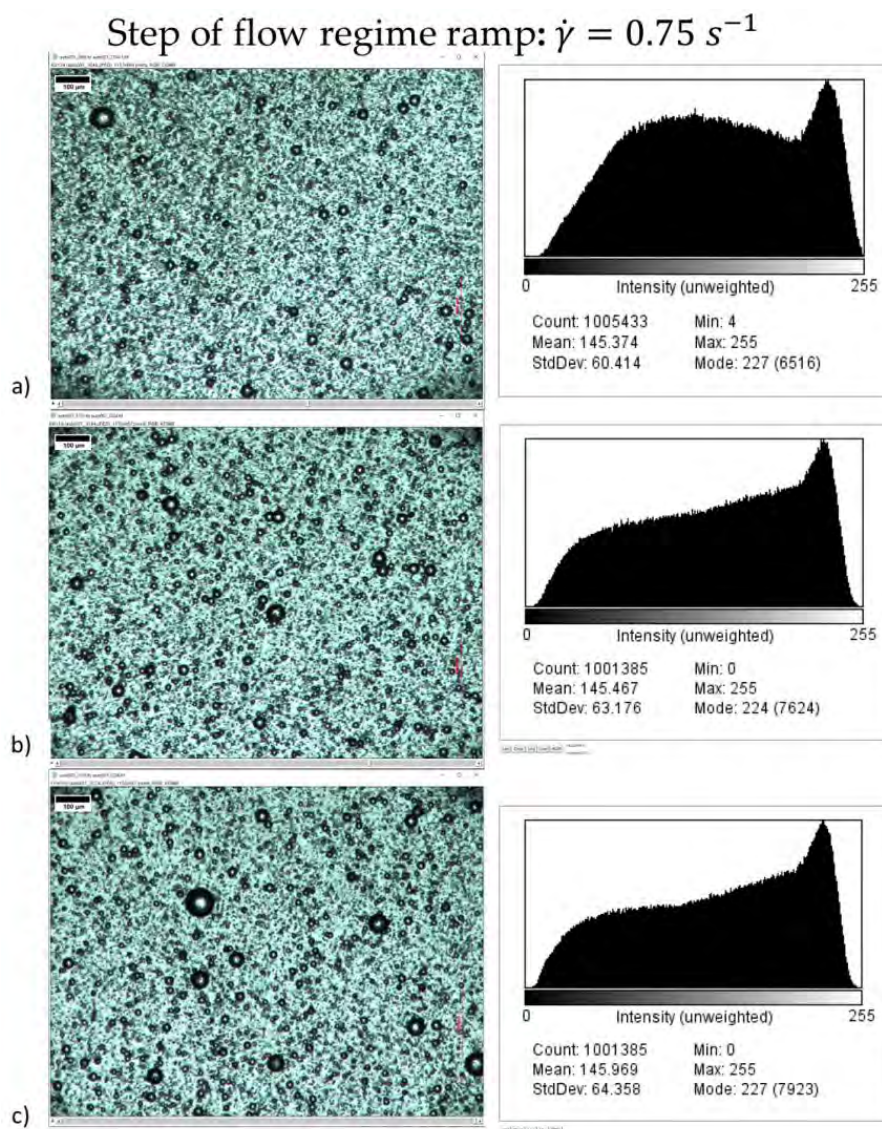
The droplet size distribution analysis was carried out using a set of snapshot at  $\sim 400$  s after the shear generation. As can be observed from Figure 3.1 the size distribution analysis during the complete duration of the pre-shearing stage — at  $0.075 \text{ s}^{-1}$ — does not provide useful information. That is, objects in these images always show poor contours, making it almost impossible to determine the correct size or count number, thus denying the possibility of evaluating a distribution of drops during the pre-shearing phase.





**Figure 3.1.** Images of the emulsion prior to flow experiments —during the pre-shearing stage,  $\tau \leq 0$ — and histogram of pixels count vs. light intensity: (a) Image of emulsion after  $t = 30$  s of pre-shearing flow of  $\dot{\gamma} = 0.075 \text{ s}^{-1}$ , and histogram with a high density of dark pixels. (b) Image after  $t = 150$  s; mean value of intensity of pixels 30 % brighter than previous image, although drop edges still poorly defined (i.e., a high probability of a continuous variation of intensity across neighboring pixels), implying a high density of overlapping droplet images.

In contrast, during each stage of the experimental ramp, images at multiple time points show that the drop size distribution *evolves continuously* during each stage of the flow regime as shown in Figure. 3.2.



**Figure 3.2.** Images of emulsion during the first step of the flow experiments –  $\tau \geq 0$ ; under a shearing flow of  $\dot{\gamma} = 0.75 \text{ s}^{-1}$ —and histograms of pixels count vs. light intensity. Intensity images show an histogram with a high rate of change of frequency vs. intensity, particularly around bright pixels, facilitating an accurate determination of the border of drops: (a) Images of emulsion after  $t = 43 \text{ s}$ , (b)  $t = 157 \text{ s}$  of flow, and (c)  $t = 415 \text{ s}$  (during the cessation of flow period after steady flow).

It is during the first shearing step –after  $t \gtrsim 40 \text{ s}$ – that meaningful statistical calculations are feasible, i.e., the initial broad hump becomes less dominant, and a high contrast peak appears on the bright pixels end; see middle and

bottom Intensity plots of Figure 3.2. The peak slopes can be associated to the changes of intensity at the border of objects; internal border have a slower variation of intensity vs. that of the outer border change of intensity. Images of emulsion after  $t = 157$  s of flow (Figure 3.2b), and during the no flow period,  $t = 415$  s (Figure.3.4c), have a sufficiently large number of drops and the intensity histogram suggest well defined border for drops in the emulsion. During flow conditions, drops have rather well defined ellipsoidal shapes, which limit the accuracy of the drop size determination.

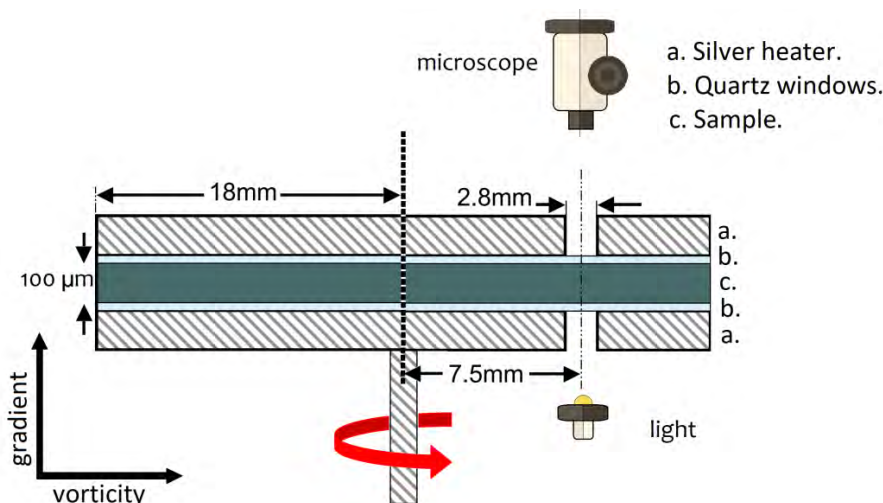
Hence, distributions obtained during the no-flow (rest) time can be used to determine the kinetics of the drop population. In Figure 3.2, during the first step of the flow ramp —at a shear rate of  $0.75 \text{ s}^{-1}$ —, images at times  $t = 43, 92$  and  $200$  s are shown, which clearly indicate the evolution of the emulsion. By looking at the Intensity plots (Figure. 3.2), it is clear that for times up to  $90$  s images still show a population with many small drops (mostly overlapping), with a poor definition of shape or size. Thus, in order to have drop size distributions of good quality (with a sample of sufficient counts of drops),  $400$  s of flow were applied during every flow step, with images presenting a population of drops of several hundreds. This protocol may reduce those artifacts due to a time evolving distribution, by eliminating the

initial time lapse of strong rate of change, although still being influence these events.

It is only during the shear rate of  $0.75 \text{ s}^{-1}$  that drops less than  $5 \text{ }\mu\text{m}$  are still observable at the bottom of the image (Figure 3.4a'). How this fraction of the population evolves (that is, elucidating the mechanism mediating this capture process) will require experiment with a different gap size. But on passing to the shear rate of 1.5, these drops are no longer observed; only drops greater than  $5 \text{ }\mu\text{m}$  are observed when the shear rate is 2.25, 3.0, 3.75 and  $4.5 \text{ s}^{-1}$  (Figure 3.4b' to f'). All size distributions are calculated when there is no flow; there were no coalescence or rupture processes observed after the flow is turned off and the distribution are also time independent.

#### **3.2.4. The experimental conditions**

All experiments were performed with the parallel plate geometry (Linkam CSS450, Linkam Scientific Instruments, Tadworth, UK), schematically shown in Figure 1. It consisted of two parallel quartz plates with a diameter of 36 mm, each in contact with flat silver heaters on the outside, with an observation window located at 7.5 mm radial position. The motion of the lower disc imposed a shearing stress field on the emulsion. Images were captured on the vorticity–velocity plane through the 2.8 mm observation window.



**Figure 3.3.** Schematic description of the shearing device: parallel-plate geometry with a diameter of 36 mm and a gap of 100  $\mu\text{m}$ . The observation plane is described by the velocity–vorticity axes. The motion of the lower disc imposes a simple shearing stress field on the sample.

The effects of the shearing and duration of the imposed shear flow were studied using a constant rotation rate with a speed control better than 1 % of the rotational speed and using a sequence of microstructure measurements at spaced events in time. In the present work, a gap spacing of 0.1 mm between disks and a temperature 30 °C was used.

Emulsion structures were visualized using an optical microscope Nikon SMZ-U (Nikon Corp., Tokyo, Japan). Capture of images was carried out with a Nikon Digital Sight DS-2 mV camera in a bright field illumination arrangement. All images were processed with the ImageJ<sup>®</sup> software (U.S. National Institutes of Health, Bethesda, MD, USA), manually and automatically. Pre-processing of drop images included assigning a threshold value, converting the image to a binary map, followed by an automatic count of drops with circularity better than  $> 0.94$ .

The statistical methods are later applied after verifying the reliability and veracity of the data obtained by the image processing.

Prior to the selection of an experimental run, the image capturing process was optimized in order to reduce the emulsion turbidity and proper exposure to light [33]. Thus, a full view image with the focus plane centered on the plane of the flow field was assured. In order to visualize the evolution of the microstructure, multiple images were taken towards the end of the shearing period and after the flow stopped and fully relaxed; images were spaced at intervals of 1 s for statistical analysis.

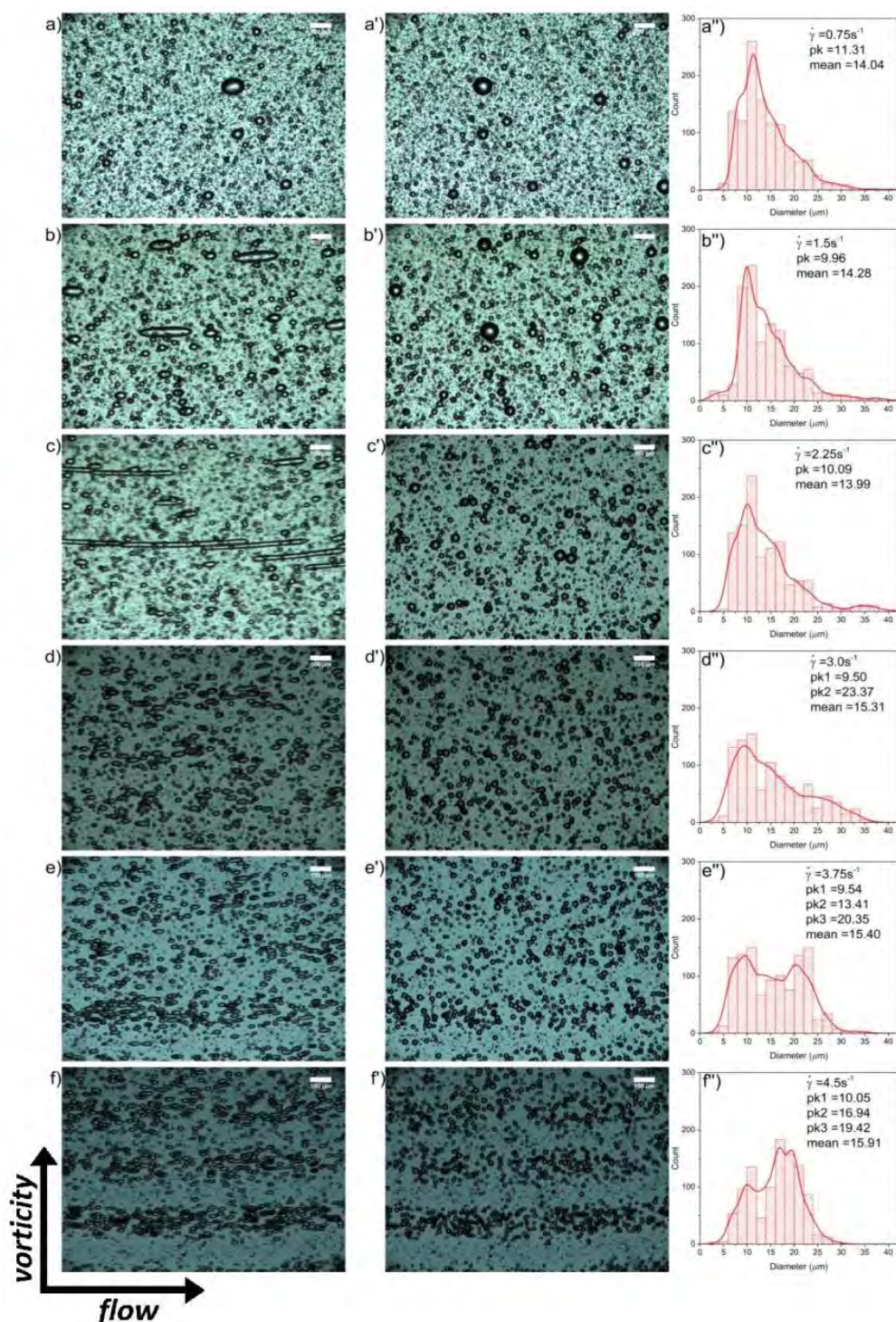
In order to obtain the droplet size distributions, mainly three operations were carried out (i.e., the image acquisition, pre-processing of digital images (involving cleansing, defining drop contours, etc.), and the statistical analysis of at least two (or multiple) images) to generate the frequency histograms. The observed droplets are those present only on the focal plane normal to the direction of the velocity-gradient. The depth of field for the optical arrangement is approximately 100  $\mu\text{m}$ , about the size of the gap between plates; thus, most drops in the flow field were observed, while the width of the field view of the microscope on the focal plane was 2–3 times larger than the captured image, thus minimizing magnification ratio variations away from the central axis.

### 3.3. Results

Figure 3.4 shows the images captured during flow and immediately after flow (unprimed and primed labels, respectively—left most columns). The applied shear rates were from  $0.75$  to  $4.5 \text{ s}^{-1}$ , top to bottom, respectively, with the corresponding density function of drop sizes—right most column. The objective is to show several of the possible structures in an emulsion induced by flow and observed during these experiments.

For  $\tau < 0$ , images would have shown many small drops, with several of them frequently overlapping along the optical path, making the correct determination of the size or the count numbers of the drops almost impossible. It is only for  $\dot{\gamma} = 0.75 \text{ s}^{-1}$  that drops less than  $5 \mu\text{m}$  are still observable at the bottom of the image (Figure 3.4a'). Understanding how this fraction of the population evolves (that is, attempting to elucidate the proper mechanism mediating this capture process) will require experiments with a smaller gap size.

Small drops, of diameter  $< 5 \mu\text{m}$  and below the lower limit of the resolution threshold [23] for this optical arrangement; these drops are not included in the distribution for the shear rate of  $\dot{\gamma} = 0.75 \text{ s}^{-1}$ . Indeed, these drops quickly disappear with increasing  $(\tau \geq 400)$ , as observed in the bottom of the images of Figure 3.4b''–f''.



**Figure 3.4.** The sequence of images shows the effects due to an increase of shear rates (top to bottom) on the evolution of the morphology (during flow, left, unprimed letters; after cessation of flow, center, and primed letters) for a (50/50) emulsion. All images are captured with the same magnification and at a temperature of 30 °C. For histograms (right plots, double primes)  $pk_n$  stands for the first, second, etc., the peak of the distribution; *mean* is the average size of drops.



Possible experiments with a weaker shear rate,  $\dot{\gamma} \leq 0.75 \text{ s}^{-1}$ , which may be most relevant for the smallest of drops, are not included here and are not considered to be relevant to the observed structural phenomena, which is the main objective of this work. Drops with a diameter larger than  $45 \mu\text{m}$  are only a few and were not considered significant to the values of the parameters of the distribution. The relative frequency of drops larger than  $45 \mu\text{m}$  is of the order of 0.00172.

One of the first effects of the shearing that was observed that can readily be evaluated occurred for the smallest bin of the population, when the frequency of the smallest of drops (about  $5\text{--}7.5 \mu\text{m}$ ) decreased and the frequency of drops with out twice the volume ( $8\text{--}10 \mu\text{m}$ ) clearly grew. This condition indicates that for flows with  $\dot{\gamma} \leq 2.25 \text{ s}^{-1}$  the critical time for *coalescence of the smaller* drops already occurred. That is, at  $\dot{\gamma} = 2.25 \text{ s}^{-1}$ , the number of small drops is reduced within a few minutes, with pairs of drops generating larger drops of about twice the volume.

As shown in Figure 3.4f,f', at larger shear rates, a poly-disperse emulsion with a multimodal distribution was generated. Here, Figure 3.4 shows that the average size of drops increased in time as the shear rate increased, accompanied by the formation of a (secondary) peak of larger drops and resulting in a *bi-modal* distribution. The same coalescence phenomenon appears to dominate the onset of the bi-modal distribution shown in Figure 3.4f'' from smaller size drops. At this

flow rate— $\dot{\gamma} = 4.5 \text{ s}^{-1}$ —the collision of drops with an average diameter close to 12–14  $\mu\text{m}$  gave rise to drops of about 16.5  $\mu\text{m}$  (double the volume of the smaller drops). From the histogram in Figure 3.4f'', it is clear that a new population phenomenon was at play: both frequencies of the 10–12  $\mu\text{m}$  and 12–14  $\mu\text{m}$  bins decreased significantly and simultaneously. It appears that pairs of drops of size 10–14  $\mu\text{m}$  may coalesce rapidly, until a more stable drop size is attained, both bins contributing to the appearance of the second and third peaks in the distribution at about 14–20  $\mu\text{m}$ .

Interestingly, Figure 3.4f also shows (a) the onset of *pearl necklace* structures—several drops of similar diameter, evenly spaced and roughly aligned along the flow direction—with ellipsoid-like drop shapes and a waist close to  $\sim 15 \mu\text{m}$ ; and (b) a banded, structured emulsion along the flow direction and perpendicular to the vorticity axis. The surprising feature of the collars and bands were their persistent lengths, several times the characteristic length scale of previous phenomena and several times the thickness of the channel (about 300  $\mu\text{m}$ ).

In these experiments, a few large drops were also observed—larger than 40  $\mu\text{m}$  in diameter, with an ellipsoid-like shape with an averaged waist size  $\sim 35 \mu\text{m}$ —at the onset of the flow regime that did not show up initially in the upper tail of the distribution. In Figure 3.4c, the highly elongated drops—similar to wire-structures—could be attributed to possibly larger drops that had reached a very

large deformation, only possibly due to confinement effects by neighboring drops and by the presence of the cell walls, simultaneously.

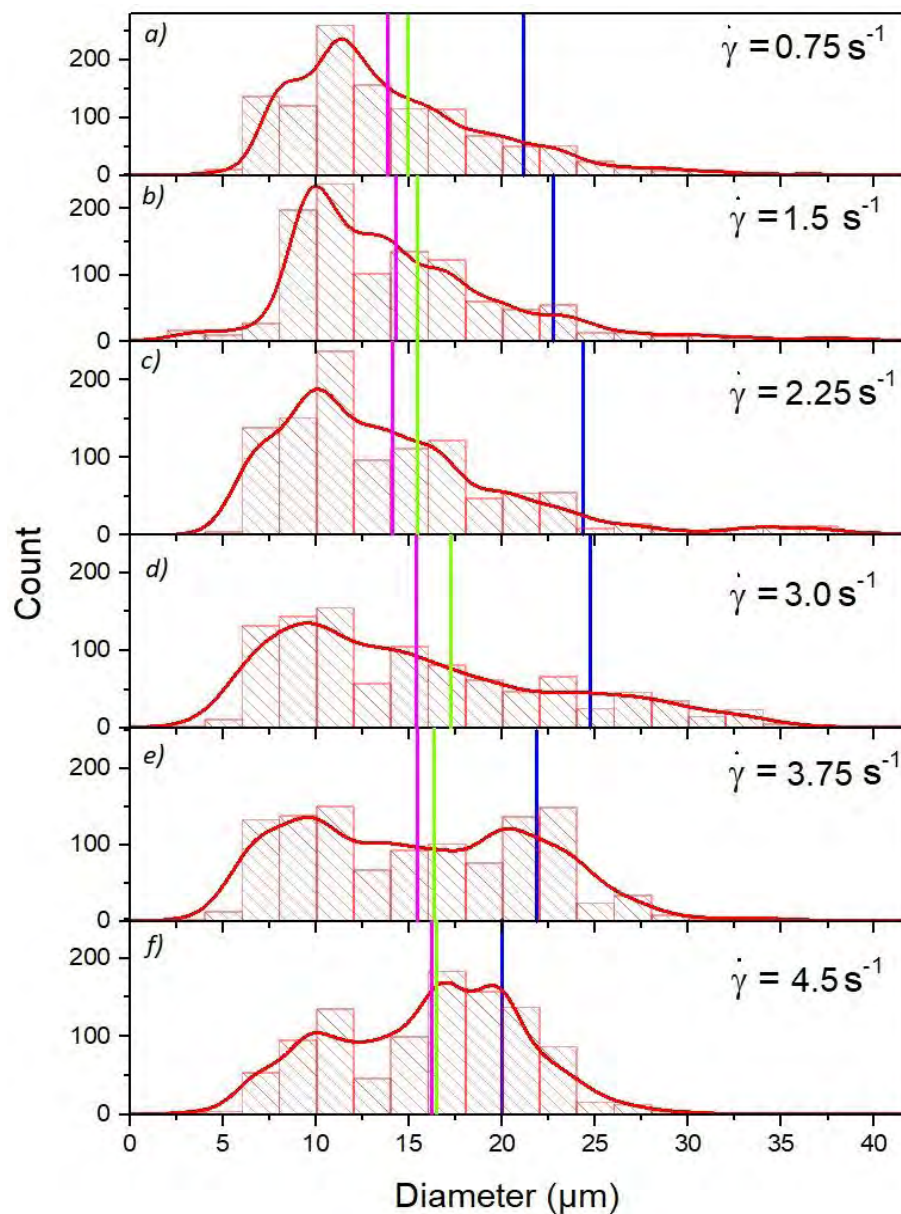
Shear Rate ( $s^{-1}$ )	Total Number Drops	Diameter Mean ( $\mu m$ )	Diameter Median ( $\mu m$ )	$D_{4,3}$ ( $\mu m$ )	$D_{3,2}$ ( $\mu m$ )	$D_{2,0}$ ( $\mu m$ )	$D_{1,0}$ ( $\mu m$ )	Distribution Properties	
								Skewness	Kurtosis
0.75	1148	14	12.9	21.1	18.6	15	13.9	1.2	1.82
1.5	1078	14.3	13.2	22.8	19.7	15.6	14.4	1.32	2.46
2.25	1084	14	13.2	24.3	20.6	15.6	14.2	1.44	2.49
3	1015	15.3	14.1	24.7	22.2	17.2	15.5	0.73	-0.39
3.75	1135	15.4	15	21.9	20.3	16.8	15.6	0.26	-0.86
4.5	1034	15.9	16.4	20	19	16.9	16.2	-0.12	-0.61

**Table 3.1.** Drop size distribution statistics for histograms shown in Figure 3.5.  $D_{4,3}$  is the volume or mass moment mean also known as the De Broucker mean diameter.  $D_{3,2}$  is the surface area moment mean or the Sauter mean diameter (SMD).  $D_{2,0}$  is the number-area mean diameter. Kurtosis measures the relative weight of the tails with respect to the central portion of the distribution

Table 3.1 presents the data used for each experiment of the most relevant parameters characterizing these distributions. Thus, approximately 1000 drops were captured for each drop size distribution, and several *measures of the diameter* were calculated. Of particular relevance are the mean ( $D_{1,0}$ ), as well as the Number-area and Number-volume mean diameter. The relevance of these numbers is further expanded upon in the Section of discussion.

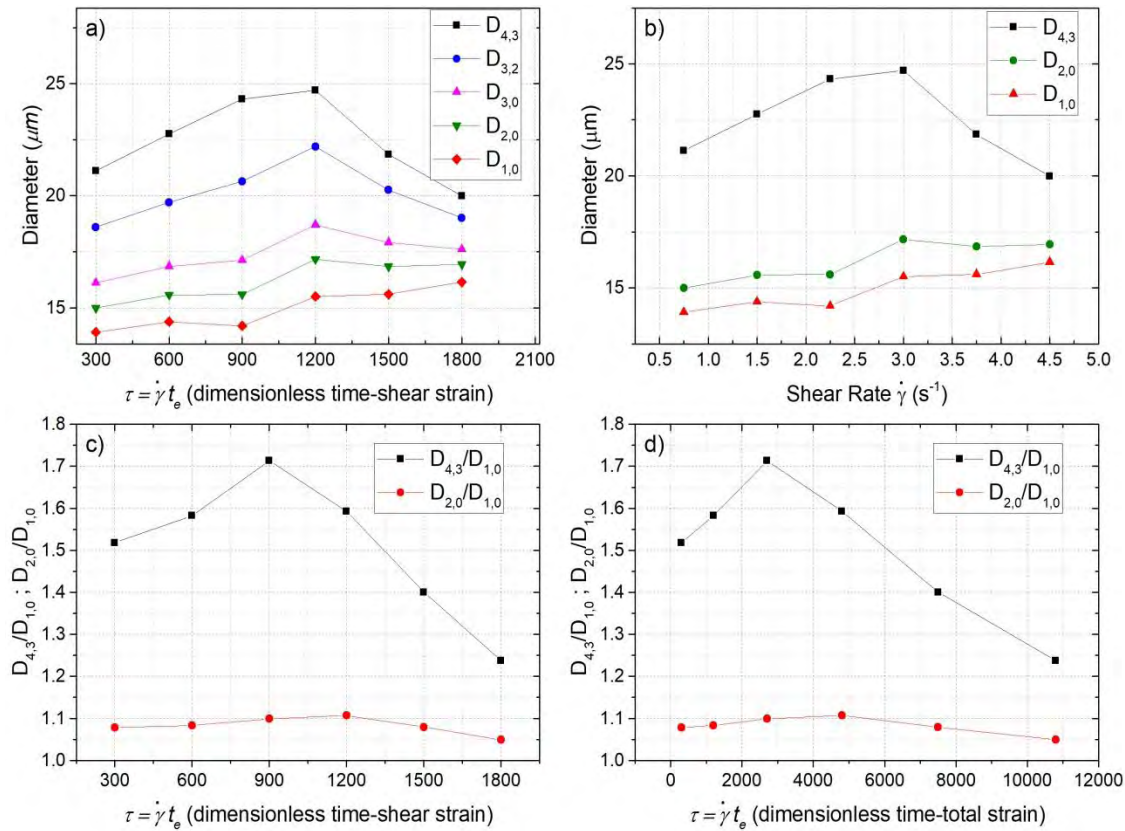
In Figure 3.5, the drop size distributions are shown with their corresponding smoothed kernels for all shear rates studied in this work. The horizontal axis is the bin average diameter and the vertical axis is the drop count. It is observed in Figure 3.5a–c that these size distributions are characterized by a single peak and positive

Kurtosis — with a single peak and relatively high weight of the distribution tails (see Table 3.1).



**Figure 3.5.** Droplet size distribution and the smoothing kernels for all shear rates studied. For the first three (lower) shear rates (a–c), the size distributions are characterized by a single peak and positive Kurtosis [34–37]; with rather broad distributions. The magenta bar corresponds to the mean diameter for the distribution, the green bar to the  $D_{2,0}$  value, and the blue bar corresponds to the value of  $D_{4,3}$ . In histogram (d), the maximum value of  $D_{4,3}$  is reached (see Table 1). Histograms (e,f) show a rapid decrease in the value of  $D_{4,3}$ , characteristic of distributions with a high top and a smaller contribution from outliers.

Please note that for a flow cell with a gap of  $100\ \mu\text{m}$ , drops with diameters as large as  $100\ \mu\text{m}$  should be observed; although, very few are seen during these experiments, which do not significantly alter the Kurtosis of the distribution. Most drop diameters are constrained to less than  $40\ \mu\text{m}$ . In Figure 3.5d, the maximum value of  $d_V = D_{4,3}$  is reached (blue vertical bar).



**Figure 3.6.** (a) Mean diameters of the distributions — $D_{1,0}$  up to  $D_{4,3}$ — vs. the dimensionless time  $\tau_i$  incurred during each flow regime; (b)  $D_{1,0}$ ,  $D_{2,0}$  and  $D_{4,3}$  vs. the applied shear rate during each regime; (c) and (d) are, respectively, the dimensionless *normalized* mean drop size vs. dimensionless time in each cycle and for the *total* duration of the flow  $\sum \dot{\gamma}_i t_i$ .

In Figures 3.5e,f, a rapid decrease in the value of  $D_{4,3}$  (Figure 3.6) is shown. This effect is mainly due to a rather broad peak, which here becomes evident by the presence of a second peak that emerges from right to left, and a Kurtosis measure

that changes sign. For the drop size distribution generated when  $\dot{\gamma} = 4.5 \text{ s}^{-1}$ , the skewness parameter becomes negative indicating a larger (secondary) peak at higher diameters

Figure 3.6 presents the evolution of the mean drop size using the suggested averages (values shown in Table 3.1). Figure 4a presents the diameter evolution with respect to the dimensionless time (or as a function of the applied shear *strain* by the flow); Figure 3.6b corresponds to the same data vs. the applied shear rate. It is clear that  $D_{1,0}$  and  $D_{2,0}$  remain essentially constant at 14 and 15.5  $\mu\text{m}$ , respectively, for times less than  $\tau \leq 800$ , abruptly increasing to means of 15.5 and 17  $\mu\text{m}$ , respectively, under a faster flow and a longer duration of the flow.

Figure 3.6c,d correspond to the normalized average size ( $D_{4,3}/D_{1,0}$  and  $D_{2,0}/D_{1,0}$ ) versus the dimensionless time and the *accumulated dimensionless time* (total imposed strain). Therefore, the base line for these two plots corresponds to  $D_{1,0}$ , a two-step function with rather constant lower and upper values (i.e., 14  $\mu\text{m}$  and 15.5  $\mu\text{m}$  (see Figure 3.6a)). The droplets generated during the preparation of the emulsion grew constantly within the initial 675 units of dimensionless time and then evolved rapidly to an average mean diameter of 15.5  $\mu\text{m}$ . In most experiments, close to 300–10,000 units of dimensionless time are necessary to reach a reproducible size distribution of the emulsions. The longer times are especially

the case for global anisotropic structures, which may require a *total dimensionless time* longer than 8000, as shown in Figure 3.6d.

### 3.4. Discussion

The distributions of drops appear to change mainly due to two processes, coalescence and rupture, with little evidence of Oswald ripening. The lack of evidence for the latter may be due to the fact that drops larger than 35–40  $\mu\text{m}$  were not evaluated. In contrast, the presence of the coalescence phenomenon can be inferred at several instances in the evolution of the distributions, which may be due to different hydrodynamic processes albeit operating simultaneously. As pointed out in the description of the coalescence kinetics, the most likely case corresponds to two of the smaller drops (about equal size) generating a drop with about twice their volume. This was clearly the case for the smaller drops in Figure 3.5a–d. But coalescence may also be the dominant mechanism for the reduction of probability observed in the first peak and in the dawning of the second peak. During collision of these larger drops, those of  $\sim 10 \mu\text{m}$  disappear, with the 15  $\mu\text{m}$  bin growing and during a subsequent coalescence, becoming drops of about 20  $\mu\text{m}$ . Coalescence seems to be the dominant mechanism for critical dimensionless time less than  $\tau \leq 700$ , with an associated critical shear rate

of about  $\dot{\gamma} \leq 2.25 \text{ s}^{-1}$ . Coalescence occurs simultaneously with rupture up to  $\tau \approx 8000$  and  $\dot{\gamma} \leq 4.5 \text{ s}^{-1}$ .

A second possible mechanism for the onset of the secondary peak is break up, particularly for the heavier tail, with the disappearance of the much larger drops (less than  $40 \text{ }\mu\text{m}$ ) producing smaller drops of about half their volume (i.e.,  $\sim 27 \text{ }\mu\text{m}$  (as shown when  $\dot{\gamma} = 3.0 - 3.75 \text{ s}^{-1}$  (Figure 3.5d,f))). These drops, in turn, break up again, producing an increase in frequency for drops sizes of about  $22 \text{ }\mu\text{m}$ . The rupture mechanism appears to depend on dimensionless time and on a critical shear rate of the order of  $\dot{\gamma} = 3.0 - 3.75 \text{ s}^{-1}$ , not being observed for smaller drops. The simultaneous contribution of these two mechanisms makes it possible to explain the appearance of the second peak of the bimodal distribution.

Figure 3.6 presents the evolution of the mean drop size (with five different measures) versus its shear rate history. Initially, droplets generated during the preparation of the emulsion grew constantly, from sizes less than the threshold of the image processing, but attained values that can be readily evaluated with the statistical measures proposed for  $\tau \geq 300$ , as shown in Figure 3.6. The mean value  $D_{1,0}$  remained at a constant value for shear rates less than  $\dot{\gamma} \leq 2.25 \text{ s}^{-1}$ —the same behavior is observed for  $D_{2,0}$ —while  $D_{3,2}$   $D_{4,3}$  increased linearly with



dimensionless time up to  $900\tau$  units, followed by a monotonic decrease of the mean size for the total accumulated dimensionless time  $\tau \geq 3000$ .

For dimensionless time between 675–900 and under an increment of  $\dot{\gamma} > 2.25 \text{ s}^{-1}$ , the mean value  $D_{1,0}$  (and  $D_{2,0}$ ) appeared to remain at a new constant value of  $D_{1,0} = 15.5 \text{ }\mu\text{m}$  (and  $D_{2,0} = 17.5 \text{ }\mu\text{m}$ ) approximately. This jump in mean diameter correlated with the time and shear rate in these experiments. An interesting observation is that the ratio of these two means was essentially constant for the complete range of values of the shear rate (see Figure 3.6c) regardless of the dimensionless time or shear rate. In contrast, measures  $D_{3,2}$  and  $D_{4,3}$  did change significantly ( $-25\%$ ) after  $\tau \geq 675$  or under an increase of  $\dot{\gamma} > 3.0 \text{ s}^{-1}$ . This abrupt collapse of  $D_{3,2}$  and  $D_{4,3}$  values correlated with the behavior of other statistical measures, indicating a dominant breakup mechanism of the larger drops. The rupture mechanism was most clearly associated with the appearance of pairs of satellite drops (of about half volume) that did not appear to influence the low end of the distribution. Hence, under these flows, the drops attained deformations associated with dumbbell shapes before breaking up, with a few of them reaching a significantly elongated waist capable of generating smaller satellite drops.

In most cases, 100–10,000 units of strain are necessary to reach a size distribution of the emulsion with low tail populations. Figure 3.6d shows a *total time* longer than  $\tau \geq 8000$ , a time scale that is representative of the anisotropic global structures observed in this emulsion. By increasing the shear rate, the arithmetic average value increased at a rather constant rate. However, the position of the peaks was not affected in a forceful way and appeared to be independent of time, contrary to the behavior of the width of each of the main peaks, which became broader over time while keeping the area under the curve approximately equal. This phenomenon may have been the result of the disappearance of the smallest droplets, as shown in Figure 3.5f. For the large drops, the formation of a secondary peak from right to left was observed (see Figure 3.5d–f), resulting in the decrease of the height of the first peak and the increase of its width and vice versa for the second peak.

Figure 4d shows a *total time* longer than  $\tau \geq 8000$ . In order to evaluate in detail the *global structure* shown in Figure 3.4e,f, associated with  $\tau \sim 8000$  global times, future experiments may require times significantly longer than the length of time considered here, as well as a new statistical analysis for evaluation of the anisotropic character of the distribution of particles in the sample.

### 3.5. Chapter Conclusions

This emulsion showed good stability when left to rest. However, under flow conditions, the size distribution changed significantly in terms of the mean values, as well as other characteristics, such as mono- to bimodal distributions or measures of skewness and kurtosis. Besides coalescence and rupture as possible explanations of the observed behavior at lower shear rates, other possible structures are readily observable, such as necklaces and banded structures. Evidence of necklaces appear at a transition  $\dot{\gamma} \sim 3.0 \text{ s}^{-1}$  in a single band to transient chains of drops in the flow direction and in several layers at a shear rate of  $\dot{\gamma} \sim 3.75 \text{ s}^{-1}$ .

These experiments also elucidate two possible mechanisms for the evolution of the size distribution of drops in highly concentrated emulsions at low shear rates. The first is coalescence, dominant for smaller drops at low shear rates and short times. The arithmetic mean of 14.0–14.3  $\mu\text{m}$  under a shear rate of about 0.75–1.5  $\text{s}^{-1}$  can be explained by coalescence of the smallest drops, while indicating a poor stability to flow induced perturbations. The behavior of the small drops indicates a high frequency of close neighbor encounters, promoting coalescence during this stage. Due to the fact that the efficiency of coalescence decreases with the increasing difference in the size of the colliding drops [2,24], coalescence tends to be less

likely at longer times. These results are in agreement with the qualitative works of Grizzuti and Bifulco [25] and Rusu and Peuvrel-Disdier [23].

The weak increase of the  $D_{1,0}$  value of the distribution as the shear rate grows may indicate that it is independent of time, which is in contrast to the behavior of the width of each of the main peaks, which increase as time passes while keeping the area under the curve approximately constant. Observing the evolution of the peaks and width of peaks in Figures 3.5d–f, it becomes evident that the largest drops rupture, giving rise to smaller ones. These dynamics may induce the appearance of the second peak (of larger drops) in Figure 3f. Here, Figures 3.6c,d show that the  $D_{4,3}$  measure decreases significantly relative to the mean value when the tail of the distribution for large drops is decreasing and rupture is a prevalent mechanism. This hypothesis may be correct; although, we have not addressed this point in detail, we may do it in future work. The tails of the distribution are less dominant as shown by the skewness and kurtosis values.

### 3.6. References

- [1] Berg, J.C. Fluid interfaces and capillarity. In *An Introduction to Interfaces & Colloids: The Bridge to Nanoscience*; World Scientific: Singapore, 2010; pp. 30–80, ISBN 978-9-81-429307-5.
- [2] Park, J.Y.; Blair, L.M. The effect of coalescence on drop size distribution in agitated liquid-liquid dispersion. *Chem. Eng. Sci.* 1975, 30, 1057–1064.
- [3] Sundararaj, U.; Macosko, C.W. Drop breakup and coalescence in polymer blends: The effects of concentration and compatibilization. *Macromolecules* 1995, 28, 2647–2657.
- [4] Leal, L.G. Flow induced coalescence of drops in a viscous fluid. *Phys. Fluids* 2004, 16, 1833–1851.
- [5] De Bruijn, R.A. Tipstreaming of drops in simple shear flows. *Chem. Eng. Sci.* 1993, 48, 277–284.
- [6] Rumscheidt, F.D.; Mason, S.G. Particle motions in sheared suspensions XII. Deformation and burst of fluid drops in shear and hyperbolic flow. *J. Colloid Sci.* 1961, 16, 238–261.
- [7] Rumscheidt, F.D.; Mason, S.G. Particle motions in sheared suspensions XI. Internal circulation in fluid droplets (experimental). *J. Colloid Sci.* 1961, 16, 210–237.
- [8] Delaby, I.; Ernst, B.; Germain, Y.; Muller, R. Droplet deformation in polymer blends during uniaxial elongational flow: Influence of viscosity ratio for large capillary numbers. *J. Rheol.* 1994, 38, 1705–1720.
- [9] Caserta, S.; Sabetta, L.; Simeone, M.; Guido, S. Shear-induced coalescence in aqueous biopolymer mixtures. *Chem. Eng. Sci.* 2005, 60, 1019–1027.
- [10] Frith, W.J.; Lips, A. The rheology of concentrated suspensions of deformable particles. *Adv. Colloid Interface Sci.* 1995, 61, 161–189.
- [11] Vinckier, I.; Moldenaers, P.; Terracciano, A.M.; Grizzuti, N. Droplet size evolution during coalescence in semiconcentrated model blends. *AIChE J.* 1998, 44, 951–958.
- [12] Lyu, S.P.; Bates, F.S.; Macosko, C.W. Coalescence in polymer blends during shearing. *AIChE J.* 2000, 46, 229–238.
- [13] Taylor, G.I. The viscosity of a fluid containing small drops of another fluid. *Proc. R. Soc. Lond. A.* 1932, 138, 41–48.
- [14] Utracki, L.A.; Shi, Z.H. Development of polymer blend morphology during compounding in a twin-screw extruder. Part I, Droplet dispersion and coalescence—A review. *Polym. Eng. Sci.* 1992, 32, 1824–1833.

- [15] Torza, S.; Cox, R.G.; Mason, S.G. Particle motions in sheared suspensions XXVII. Transient and steady deformation and burst of liquid drops. *J. Colloid Interface Sci.* 1972, 38, 395–411.
- [16] Grace, H.P. Dispersion phenomena in high viscosity immiscible fluid systems and application of static mixers as dispersion devices in such systems. *Chem. Eng. Commun.* 1982, 14, 225–277.
- [17] De Bruijn, R.A. Deformation and Breakup of Drops in Simple Shear Flows. Ph.D. Thesis, Eindhoven University of Technology, Eindhoven, The Netherlands, 1989.
- [18] Chesters, A. Modelling of coalescence processes in fluid-liquid dispersions: A review of current understanding. *Chem. Eng. Res. Des.* 1991, 69, 259–270.
- [19] Abid, S.; Chesters, A.K. The drainage and rupture of partially-mobile films between colliding drops at constant approach velocity. *Int. J. Multiph. Flow* 1994, 20, 613–629.
- [20] Coualaloglou, C.A.; Tavlarides, L.L. Description of interaction processes in agitated liquid-liquid dispersions. *Chem. Eng. Sci.* 1977, 32, 1289–1297.
- [21] Ramic, A.J.; Stehlin, J.C.; Hudson, S.D.; Jamieson, A.M.; Manas-Zloczower, I. Influence of block copolymer on droplet breakup and coalescence in model immiscible polymer blends. *Macromolecules* 2000, 33, 371–374.
- [22] Liao, Y.; Lucas, D. A Literature review on mechanisms and models for the coalescence process of fluid particles. *Chem. Eng. Sci.* 2010, 65, 2851–2864.
- [23] Rusu, D.; Peuvrel-Disdier, E. In Situ characterization by small angle light scattering of the shear-induced coalescence mechanisms in immiscible polymer blends. *J. Rheol.* 1999, 43, 1391–1409.
- [24] Lyu, S.; Bates, F.S.; Macosko, C.W. Modeling of coalescence in polymer blends. *AIChE J.* 2002, 48, 7–14.
- [25] Grizzuti, N.; Bifulco, O. Effects of coalescence and breakup on the steady-state morphology of an immiscible polymer blend in shear flow. *Rheol. Acta* 1997, 36, 406–415.
- [26] Minale, M.; Mewis, J.; Moldenaers, P. Study of the morphological hysteresis in immiscible polymer blends. *AIChE J.* 1998, 44, 943–950.
- [27] Minale, M.; Moldenaers, P.; Mewis, J. Effect of shear history on the morphology of immiscible polymer blends. *Macromolecules* 1997, 30, 5470–5475.
- [28] Bentley, B.J.; Leal, L.G. An experimental investigation of drop deformation and breakup in steady, two-dimensional linear flows. *J. Fluid Mech.* 1986, 167, 241–283.
- [29] Jansen, K.M.; Agterof, W.G.; Mellema, J. Droplet breakup in concentrated emulsions. *J. Rheol.* 2001, 45, 227–236.
- [30] Guido, S.; Villone, M. Measurement of interfacial tension by drop retraction analysis. *J. Colloid Interface Sci.* 1999, 209, 247–250.

- [31] Silverman, B.W. The kernel method for univariate data. In *Density Estimation for Statistics and Data Analysis*, 1st ed.; Routledge: New York, NY, USA, 1986; pp. 34–74, ISBN 0412246201.
- [32] Scott, D.W. Kernel Density Estimators. In *Multivariate Density Estimation: Theory, Practice, and Visualization*, 2nd ed.; John Wiley & Sons: Hoboken, NJ, USA, 2015; pp. 137–216, ISBN 1118575482.
- [33] Caserta, S.; Simeone, M.; Guido, S. 3D optical sectioning and image analysis of particles in biphasic systems. *Microsc. Anal.* 2005, 19, 9–11.
- [34] Wang, H. Path factors of bipartite graphs. *J. Graph Theory* 1994, 18, 161–167.
- [35] Kurtosis in Probability Distributions. Available online: <https://en.wikipedia.org/wiki/Kurtosis> (accessed on 22 April 2018).
- [36] Kim, T.H.; White, H. On more robust estimation of skewness and kurtosis. *Financ. Res. Lett.* 2004, 1, 56–73.
- [37] Moments. Available online: <https://www.originlab.com/doc/X-Function/ref/moments> (accessed on 22 April 2018).

## ***Chapter 4: Morphology of Banded, Anisotropic Structures***

In this Chapter, a study of *the formation of bands of drops along the direction of the vorticity* in a concentrated emulsion is presented. That is, the observed anisotropic structures are characterized by regions of high concentration of drops interspaced with regions of about equal width where hardly any particles are present. These particle distributions are a clear departure to what has previously reported for this emulsion. These patterns are induced by the effect of a simple flow in circular parallel plate geometry (CSS450-Linkam), but only after a prolonged time after the inception of the flow. That is, the observation of bands in emulsions appears only after various other phenomena occur in the emulsion.

The flow geometry used is described in detail In Chapter 2. The emulsion composition and preparation is described as well in Chapter2. The flow history, previous



to the appearance of the banded structure, is that described in detailed in the latter Chapter. That is, the separation of the flow cell plates is 100  $\mu\text{m}$ , and the observation of bands occurs within the interval of shear rates of 3.0 to 4.5  $\text{s}^{-1}$ , but only after a long evolution of the initial structure with a series of flows of 0.75 to 2.25  $\text{s}^{-1}$ . This Chapter contains ideas similar to those presented by Caserta and Guido [1, 2], although *these banded structures appear to require a previous evolution of the drop distributions and structure*, before the onset of these bands, albeit other differences.

#### **4.1. Introduction**

The formation of oriented structures in two-phase systems, as in this study, and in particular the formation of bands of droplets, is a phenomenon that attracts a considerable interest in the scientific and industrial fields. Its vast set of applications is directed to the fields of microfluidics, the food industry, as well as granular materials, among other possibilities.

Some band formation studies have been reported in the literature for different types of samples, such as granular materials [3], stiff particle suspensions [4], liquid crystals [5], polymer solutions [6] and attractive emulsions [7,8]. The formation of bands in dilute emulsions is reported mainly in the geometry of concentric rollers

[9]; where band formation can occur in all three directions (the direction of the flow, of the velocity gradient, and in the direction of vorticity). These bands may depend on the flow on different variables and under very specific and different conditions.

The essential difficulty of understanding of band formation in biphasic systems is the simultaneous presence of physicochemical, hydrodynamic and mechanical effects. Also, It is quite common that banded structure materials show length scales covering several decades. For example, the characteristic length scales observed in composites for car-fenders is as small as 0.3  $\mu\text{m}$  while its macroscopic features are larger than several millimeters. In technologies of the order of micro and nano, where biphasic mixtures play an essential role, these physical processes are still poorly understood [10].

The trend of studies in this field have been recorded for a couple of decades, and it is considered that *it occurs in complex fluids whose relaxation times are slow* [11-13]. But there are recent reports in which the phenomenon can also be evidenced in relatively "simple" systems, as are two Newtonian liquids, immiscible and without surfactants [14]. Thus, the slow relaxation mechanisms can not be inferred from the dynamics of individual constituents. The slow mechanisms are the result of a collective dynamics that is not easily determined or understood. Next,

I systematically study the formation of bands in a water-in-oil emulsion, with a 50/50 fraction and under a simple shearing flow.

#### **4.1.1. Shear banding in the emulsion**

The first reports of bands formation by flows emphasize the correlation with the shearing rate in solid samples, then in mixtures of molten polymers and finally in emulsions. However, in the field of emulsions the work of Caserta, et al. [2] is the most recent and addressing the *relationship of structure and flow properties*. Consequently, the phenomenon of bands in emulsions is a rather new and poorly studied phenomenon, even though it is of highly relevant in advance manufacture of medical and optical devices, whose motivation lies in minimizing its components. From a purely conceptual perspective, the essential objective is to understand the relationship of physical phenomena of large scales with the microscale of its structure, and, more importantly, of the microscale at the macro scale [15]. That is, understanding a coupling of time- and length-scales induced by a non-equilibrium flow condition. First, a brief explanation of the states by which the emulsion must evolve to reach the formation of bands. It is important to say that the following description is the result of a systematic consultation of observed phenomena related to the morphology of biphasic systems.

When an emulsion is subjected to a simple flow, the observed structural phenomena depend on a set of multiple variables. But to favor the phenomenological understanding of the banding structure, we will focus on three variables specifically; the confinement ( $Co = 2R / H$ ), the viscosity ratio ( $p$ ) and the shear rate ( $\dot{\gamma}$ ). The confinement ( $Co$ ) is the ratio between the diameter of the drop and the separation of the circular plates. This dominant dimensionless scale has its origin on the definition frequently used with diluted systems, for example, an isolated drop. In the literature, we find banded systems with  $p \sim 1$  and values of  $0.2 < Co < 0.56$  [16]. From which the phenomenological idea is extracted to create the scenarios in the formation of bands.

The scenarios of the morphological evolution induced by flow are, initially, the alignment and elongation of drops; the second may be the coalescence of drops and the third, when highly elongated its rupture into multiple smaller drops. These phenomena may happen simultaneously. And after a long time, the evolution may show (fourth scenario) the formation of bands.

The bands appear from an initial emulsion, visibly homogeneous. Prior to the observation of bands other measurable phenomena dominate the emulsion structural evolution. Bands are ordered, equally spaced and intercalary along the direction of vorticity. The first visible band is from the outside in, on the vorticity

axis. This scenario is for  $p = 0.27$  and a critical capillary  $Ca_{cr} \sim 0.21 \pm 0.07$ , explained next.

#### 4.1.2. The breakup of droplets under a shearing flow

The so-called critical capillary number required for rupture of a vesicle,  $Ca_{cr}$ , expresses the minimum flow stresses required for a large elongation and break up of a drop.  $Ca_{cr}$  appears to depend principally on  $p$  for simple shear flow, as shown by Grace's work [17] and the by De Bruijn [18]. A broad set of data for drops deformation and break up, including a large class of 2D-flows – covering from pure shear up to a purely elongational flow – was provided by Bentley and Leal [19]. Furthermore, for emulsions subjected to simple shear flow flows, Jansen [20] has recently shown that the critical capillary number decreases as well with increments of *the fraction of the disperse phase*; that is:  $Ca_{cr}(p, \phi)$ .

Single droplet breaking mechanisms and shapes of Newtonian liquid have been extensively studied. If  $Ca \ll 1$ , the shape of the drop is slightly ellipsoidal, depends on the value of  $p$ , and the drop is aligned at an angle of  $45^\circ$  with respect to the flow direction. As the capillary number increases, the steady state elongation grows, and the drop rotates considerably, aligning itself along the direction of flow. For higher capillary numbers, beyond the critical value, rupture is observed with the breaking mode depending on the viscosity ratio. For  $p < 1$ ,

the drops assume an elongated highly cusped form, from which small drops (the so-called tip streaming phenomenon) are launched. For  $p$  approximately equal to 1, the central portion of the droplet forms a neck (or necks) until followed by the breaking up into two daughter-droplets, with small satellite droplets between them.  $Ca \gg Ca_{cr}$ , droplets are deformed into long, thin fiber filaments that eventually break up through the capillary wave instability mechanism. These mechanisms become more complicated as the density of disperse phase drops increases, and length scales of different object overlap considerably, including non-negligible effects due to the presence of the flow cell walls.

## **4.2. Materials and Methods**

### **4.2.1. Constituents and preparation of emulsions**

Two immiscible fluids were prepared as the emulsion disperse-continuum components looking for a pair of liquids with high viscosities and equal densities: an aqueous solution, as the dispersed phase, and a mixture of alkanes as the oil base fluid as the continuum phase, as described in Chapter 2.

The aqueous phase has a viscosity of  $0.57 \text{ Pa} \cdot \text{s}$ , and the continuum phase has a viscosity of  $2.08 \text{ Pa} \cdot \text{s}$  at  $30 \text{ }^\circ\text{C}$ ; the viscosity ratio is  $p = 0.27$ . The fluids densities ( $\text{g}/\text{cm}^3$ , at  $30 \text{ }^\circ\text{C}$ ) are 0.98 and 0.95 for the aqueous phase and the continuum phase,

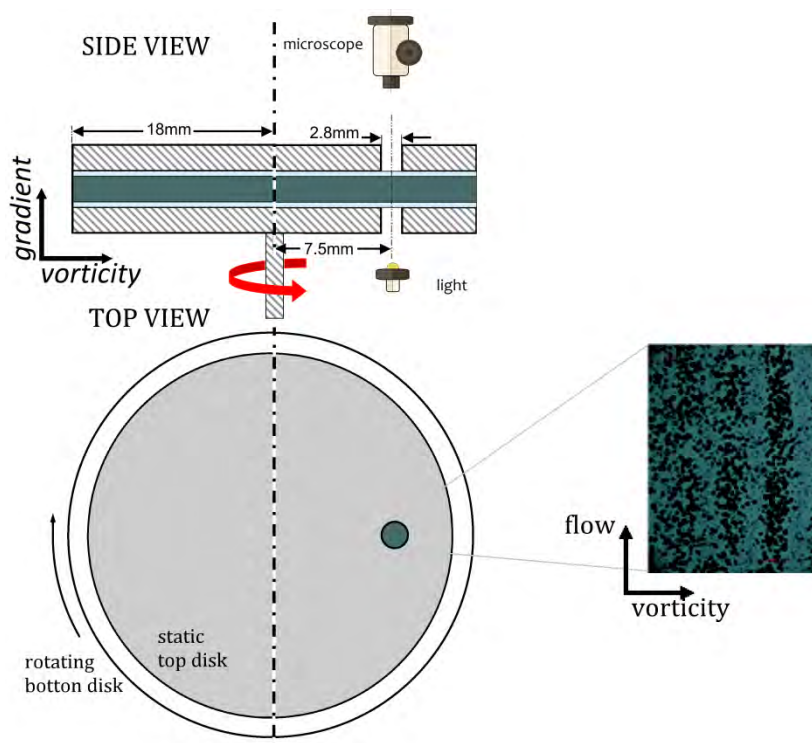
respectively. For the aqueous-oil mixture, the density of the two fluids can be adjusted by altering the composition of the low molecular weight liquids, while the high molecular weight polymers are used to adjust the relative viscosity. These two characteristics make this sample a good working fluid mixture for simulations of oil-water emulsions such as crude oil and water. The interfacial tension  $\sigma$  was determined by the method of DDR as described by Guido and Villone [30]. The measured averaged surface tension is 0.11 mN/m, evaluated for a set of 11 drops of aqueous fluid (40 %) in the oil phase.

Samples of this emulsion manifest a banded structure of drops, *after a previous flow history* is used, as described in Chapter 3. Even though, a steady change of the drop size distributions occurs previously to the application of a flow with a shear rate of  $3.0 \text{ s}^{-1}$ , here reported are banded structures after other important changes are observed, the former having been reported in Chapter 3. These earlier changes do not show any banded structure as the ones to be describe in this Chapter. All flow experiments started with an initial pre-conditioning of the emulsion, which corresponds to a series of steady flows, beginning with a shear rate of  $0.75 \text{ s}^{-1}$  up to  $3.0 \text{ s}^{-1}$  for  $\sim 500 \text{ s}$  each step. Preconditioning flow manifests a complex dynamic for the structure. However it does not allow inferring a drastic change such as the subsequent evolution into bands. The loading of the flow cell is carried out as in

previously described experiments. Following loading, the cell was allowed to relax for a period of  $\sim 600$  s.

#### 4.2.2. Parallel disks cell/device

All experiments were carried out using the parallel plate geometry (Linkam CSS450, Linkam Scientific Instruments Manufacturer, Tadworth, UK), schematically shown in Figure 4.1. The motion of the lower disc imposed a shearing stress field on the emulsion. Images were captured on the vorticity–velocity plane through the 2.8 mm observation window. In the present work, a gap spacing of 0.1 mm between disks and a temperature of 30 °C was used.



**Figure 4.1.** Schematic description of the shearing device: parallel-plate geometry with a diameter of 36 mm and a gap of 100  $\mu\text{m}$ . The velocity–vorticity axes describe the observation plane. The lower disc motion imposes a simple shearing field on the sample.

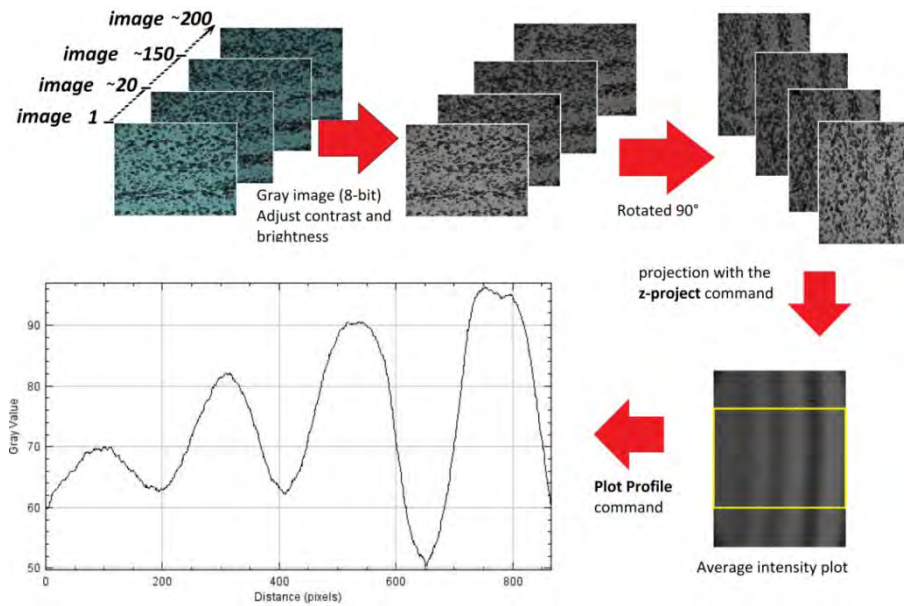


Images of the banded structure of the emulsion are experimentally observed through a small hole of the flow device — which cover a surface of only 0.6% of the total area of the geometry — and captured images (1000 x 1340  $\mu\text{m}$ ) corresponds to 0.02 % of the flow field area. Thus, the real extension in the flow of these bands cannot be inferred from these experiments, precluding a better understanding the role that large time- and length-scales may play in this phenomenon. In Appendix C, the location of the captured image in the observation hole is described. The formation of the vorticity axis bands (parallel to the flow axis), as shown in Figure 4.1, appear to arise in the centripetal direction. The width of the first band changes with time and is related to (is of the order of) the separation of the plates.

Emulsion structures were visualized using an optical microscope Nikon SMZ-U (Manufacturer Nikon Corp., Tokyo, Japan) as previously described. Capture of images was carried out with a Nikon Digital Sight DS-2mV camera in a bright field illumination arrangement. All images were processed with the ImageJ® software (U.S. National Institutes of Health, Bethesda, MD, USA, City, Country), manually and automatically. Before the selection of an experimental run, the image capturing process was optimized to reduce the emulsion turbidity and proper exposure to light [33]. Thus, a full view image with the focus plane centered on the plane of the flow field was assured.

### 4.2.3. Images analysis

To visualize the evolution of the microstructure, multiple images were taken towards the end of the shearing period and after the flow was stopped and fully relaxed; images were spaced at intervals of 1 s for statistical analysis, as shown in Figure. 4.2.



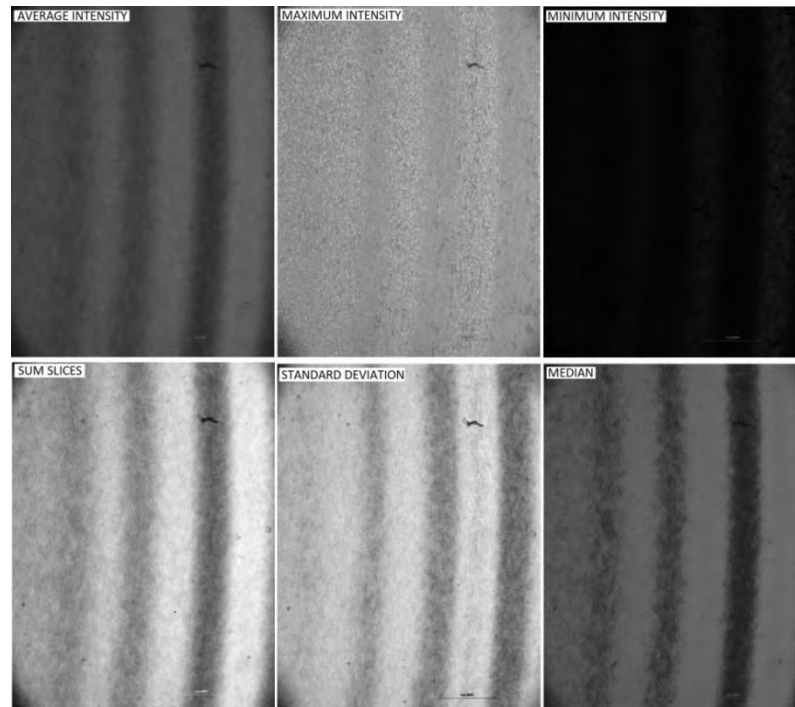
**Figure 4.2.** Scheme of the image analysis procedure, for the description of the evolution of band formation. It is essential to include the flow direction with an arrow. The stacking of images correspond to the shear rate of  $4.5 \text{ s}^{-1}$ .

To extract the information from the captured images, we proceed in steps. These steps are: (a) The capture: this stage is the experimental arrangement, the camera, the zoom; the details are described in Section 2.6. (b) The pre-processing: where the noise of images is reduced, and those details that are not of interest in the experiment are eliminated. (c) The segmentation: here the drops to be measured are evaluated according to a size and shape criteria. The extraction of the

characteristics: here we proceed to obtain the chosen measurements of each of the objects, images, and stacks.

The observation of bands in the direction of vorticity is analyzed quantitatively using ImageJ® software and compared systematically against changes due to increments in the applied shear rate. The stage of pre-processing, segmentation and extraction of the images are shown in Figure 4.2. The ~200 images captured during the flow are collected for each shear, i.e., six collections of approximately 200 images each. These ~200 images are stacked, and rotated 90° in an anti-clockwise direction, to favor the analysis and subsequent visualization of the results. Subsequently, the stack is converted to an 8 bit grayscale, also adjusting the contrast and brightness of the stack.

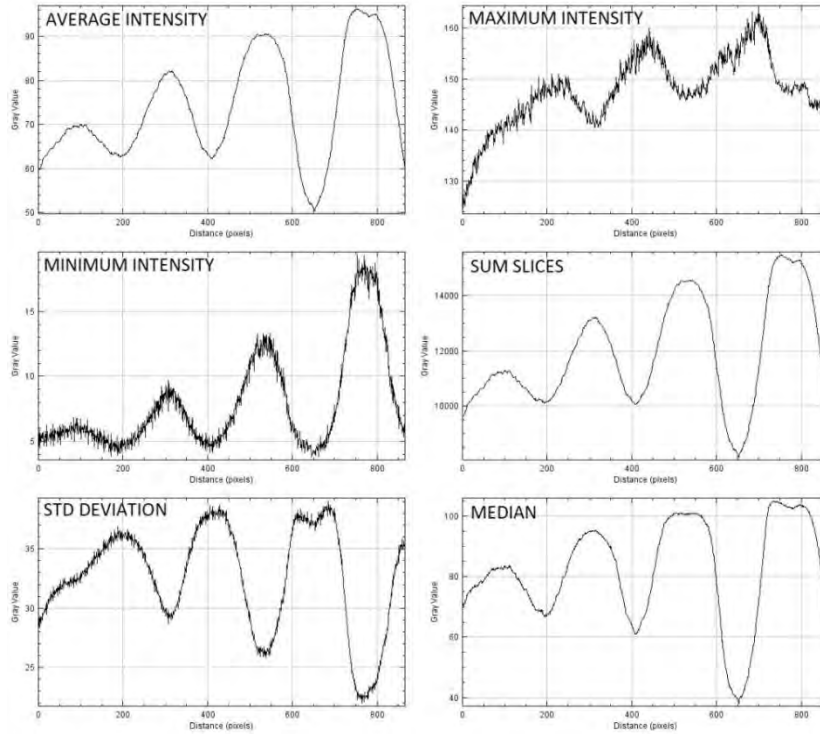
Later, a projection with the z-project command is made, —remember that the z-project command analyzes stacks by applying six different methods of projection of pixels of the stack. The six techniques of the z-project command are shown in Figure 4.3, where each of the images is the result of applying the z-project command to the same shear rate (of  $4.5 \text{ s}^{-1}$ ) image. In Figure 4.3, all six techniques are presented. Each technique allows us to visualize the formation of bands in a different way, for example, in some cases, the band is shown in black and others in white, or is not visible.



**Figure 4.3.** The z-project techniques for banding analysis. From left to right: average intensity, maximum intensity, minimum intensity, sum slices, standard deviation, and median.

To determine which of the techniques is the most favorable for our purposes, a graph of each technique of intensity vs. radial distance of the whole image is made with the plot profile function as can be seen in Figure 4.4. The graph obtained of intensity vs. radial distance shows undulations; where intervals of intensity—where 0 is equal to black and 255 to white— are used.

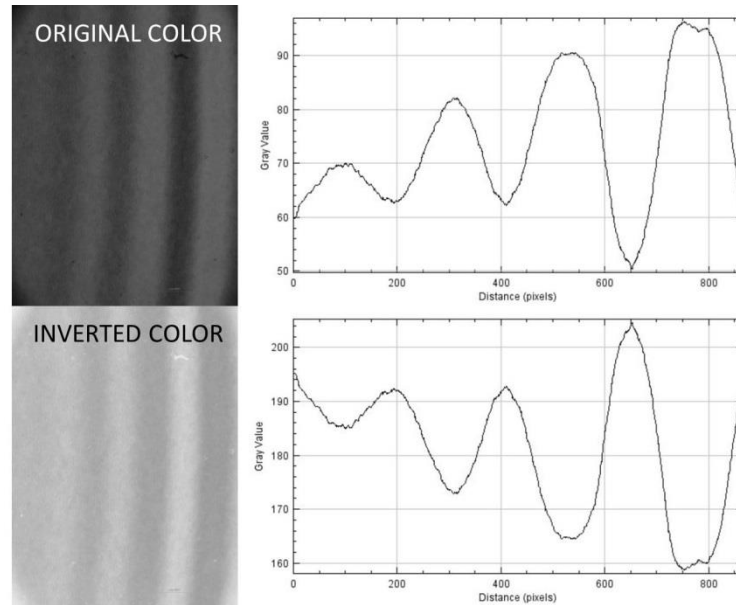
For example, when using Average, minimum sum and median graphs, valleys represent areas (regions) with the highest droplet population during flow, and crests, vice versa. Conversely, the same happens with the techniques of maximum intensity and standard deviation.



**Figure 4.4.** The plot of the Intensity vs. radial distance graph of z-project techniques for banding analysis. From left to right: average intensity, maximum intensity, minimum intensity, sum slices, standard deviation, and median.

For example, when using Average, minimum sum and median graphs, valleys represent areas (regions) with the highest droplet population during flow, and crests, vice versa. Conversely, the same happens with the techniques of maximum intensity and standard deviation.

Thus, the average intensity technique is chosen here for the analysis, for it provides the most accurate method for our purposes. The noise is minimal and allows identifying the evolution of the population of droplets at the borders of the bands. To facilitate understanding of the data, the gray hue of the average intensity technique is inverted.

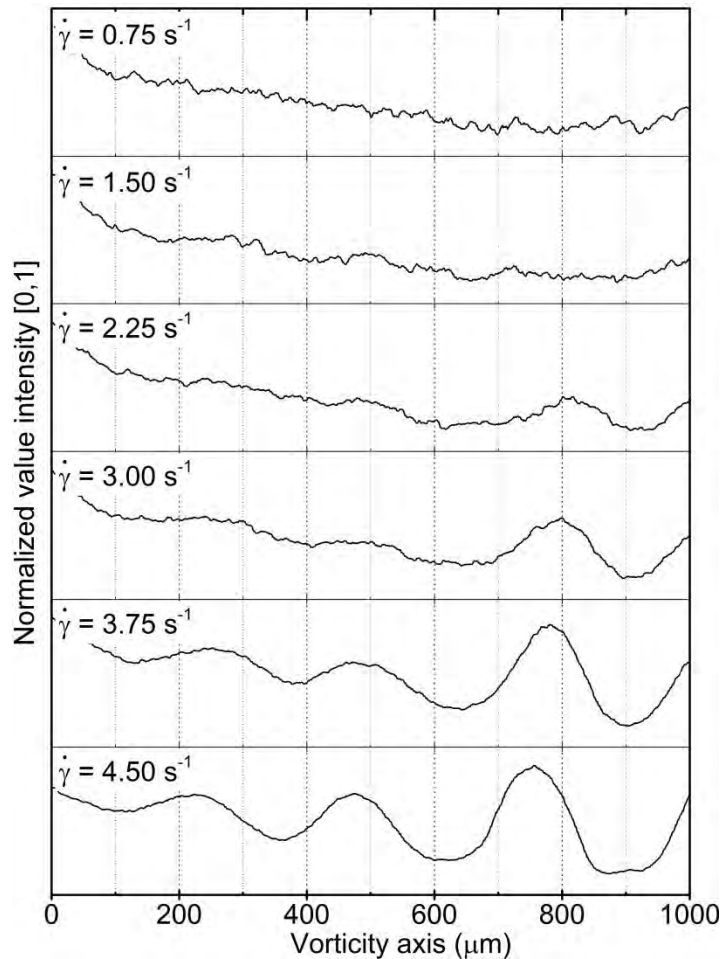


**Figure 4.5.** Image obtained with the average intensity technique with color inversion (left side) and its graph of intensity vs. radial distance (px) for shear rate of  $4.25 \text{ s}^{-1}$  (right plots). In the image of inverted colors, valleys correspond to a low population of drops and peaks to a high population of drops.

In this manner, at the moment of making intensity vs. radial distance graphs, each valley represents the low population of drops and each peak the high population of drops, as shown in Figure. 4.5. Hence, the projection on the perpendicular axis of the image plane is made with the average intensity technique, for each single shear rate.

The described methodology is applied to each of the studied shear rates, as shown in Figure 4.6. To improve the visualization of the information, the abscissa corresponds to the position along the vorticity axis, while the ordinate contains data of the normalized intensities [0, 1]. Image processing provides information on the average position of the peak of the band at all times of the evolution. As

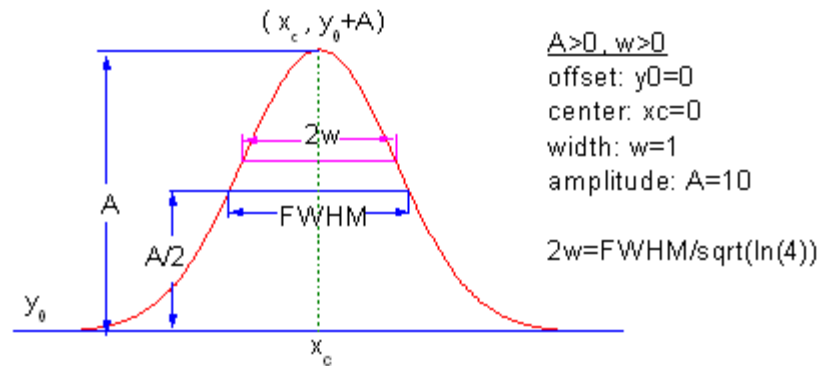
well, it is possible to make a qualitative comparison of the number of drops in each zone by evaluating the *relative* height of each peak (wrt. the intensity of the valley). Figure 4.6 shows the profiles obtained from stacking images for various shear rates. Only shear rates higher than  $3.0 \text{ s}^{-1}$  show, clearly, band formation.



**Figure 4.6.** Intensity vs. radial distance graph from  $0.75$  to  $4.5 \text{ s}^{-1}$ , each  $0.75$  (top to bottom). Formation and displacement of the bands. The intensity axis was normalized from 0 to 1.

In order to determine the long times evolution of each band, a second statistical analysis is carried out. The objective is to characterize the intensity data by adjusting a Gaussian curve with parameters shown in Figure 4.7. The Full Width

at Half Maximum (FWHM), the amplitude (A) and the position of the peak ( $X_c$ ) are the parameters taken into account for the acquisition of the width of the band, the population of the drops and the possible displacement of the peak.



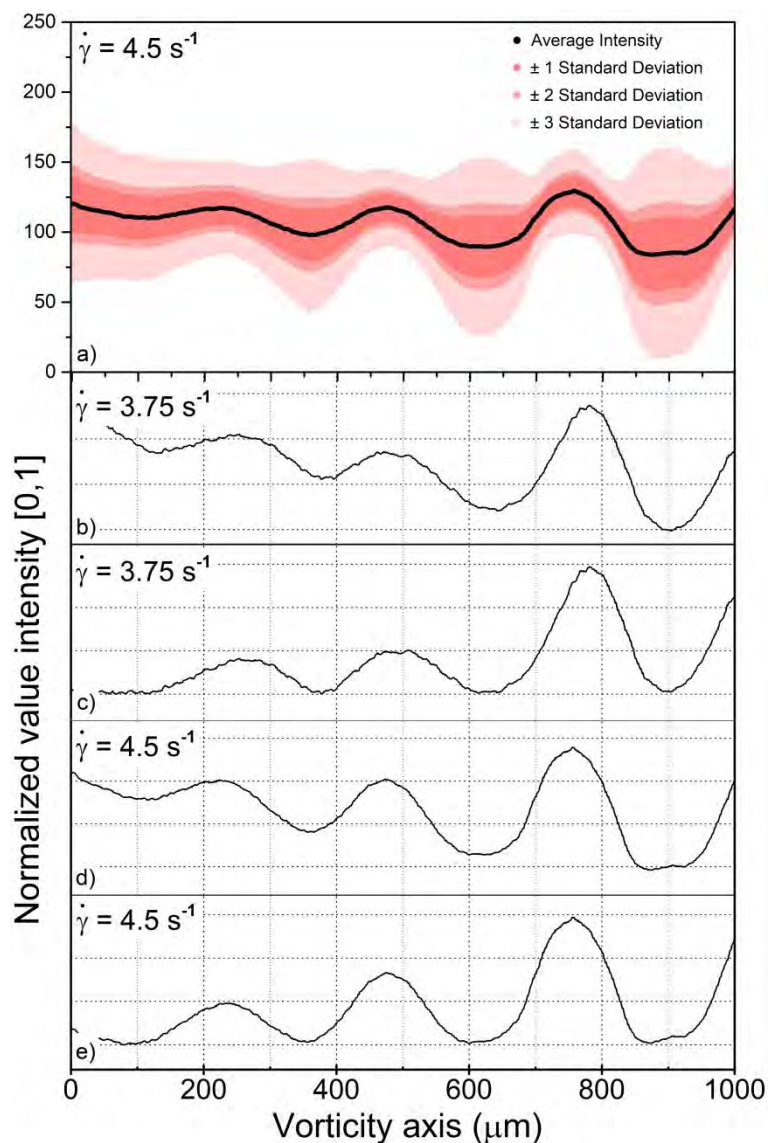
**Figure 4.7.** Plot the average intensity of 10 images (1 fps) for a shear rate of  $4.5 \text{ s}^{-1}$ . The parameters obtained from the adjustment of a Gaussian curve are indicated.

Figure 4.8 shows the four parameters that characterized the dynamics about each peak. Each Intensity vs. position plot is composed of 867 columns (aligned with the flow direction), and each column has 1155 intensity values. Thus, each plot of the graph —plots Figure 4.8b and 4.8d— represents the mean value of the intensity for 11,550 readings produced with 10 images, at a specific time in the evolution of the drops distribution.

The black trace in Figure 4.8a corresponds to the mean intensity value for that column. Intense (and light) red bands show the uncertainty range at each column, indicating that large fluctuations are due to large number of drops passing by. But as is shown in Figure 4.6, fitting a Gaussian curve to peaks on intensity plots

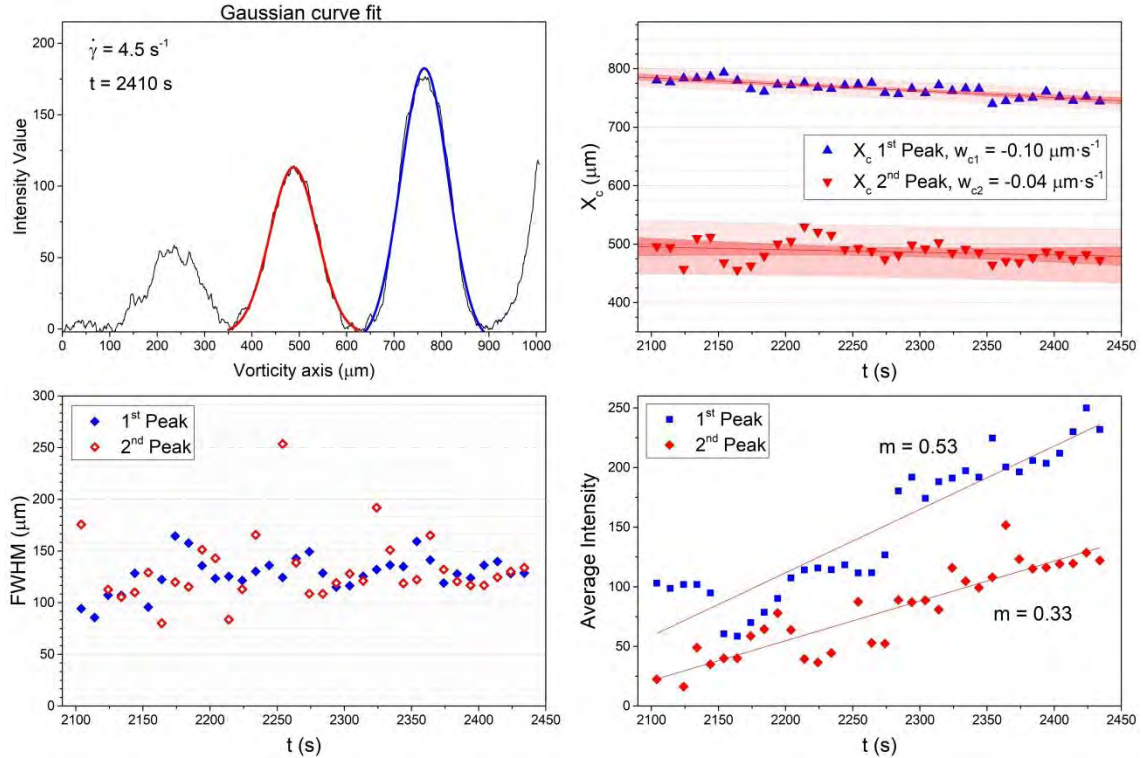


requires setting a common baseline at both ends of the curve; i.e., traces shown in Figure 4.8c and 4.8e.



**Figure 4.8.** Intensity vs. vorticity axis ( $\mu\text{m}$ ) of a pack of 10 images (1 fps) for  $\dot{\gamma} = 3.0 \text{ s}^{-1}$  and  $4.5 \text{ s}^{-1}$ . Plot (a) shows the black trace for the mean intensity at each column, while red bands correspond to their uncertainties. Plots (b) and (d) correspond to raw intensities, while (c) and (e) to intensities with a baseline correction.

Thus, Figure 4.9 shows the adjustment carried out for the two highest shear rates.



**Figure 4.9.** On the left upper side is the graph of intensity vs. vorticity axis ( $\mu\text{m}$ ) of a pack of 10 images (1 fps) after a mean time of  $t = 2410 \text{ s}$  from the beginning of the experiment, for two peaks. Top and right graph corresponds to the peak position displacement observed for all 34 ministacks, i.e.,  $x_c$  vs. time for the two most significant peaks. On the lower side are the graph of FWHM and of intensity vs. time, respectively. Blue data points correspond to the right most peak and red point to the middle peak.

For the analysis shown in Figure 4.9, the plots are the average intensity (vs. position along the vorticity axis) with an adjusted baseline. The *time tag* for this data set corresponds to 10 images, around 2410 s, after the onset of flow at  $4.5 \text{ s}^{-1}$ . These images corresponding to 10 s of flow, with total time of 337 images for the full stack. Thus, the information is coalesced into 34 mini-stacks (34 data point) to track the complete time evolution of the peak dynamics, i.e., duration of the experiment.

The blue and red solid traces (Figure 4.9a) are the adjusted Gaussian curves that best describes the intensities about those bands. Properties for the Gaussian trace indicate that its FWHM width remains roughly constant at  $135\ \mu\text{m}$  after 2150 s of flow, for both bands. In contrast, the growing amplitude indicates that the number of drops on the band is still increasing, but at a rate proportional to its height.

The trace of  $x_{ci}$  vs. *time* measures the leftward displacement of the peak beginning at 2000 s after the onset of flow. The mean lateral displacement velocity of the peak is higher for the right peak at  $-w_{c1} = 0.10\ \mu\text{m}\cdot\text{s}^{-1}$  (toward the center of rotation of the flow cell). In the Results and Discussion Sections, these findings are further analyzed.

#### **4.2.4. The Horizontal Distribution of Drops. The velocity field of the developed flow on the x-w plane.**

The observed accumulation of drops on a banded structure seems to imply that there is an underlying complex velocity field of the flow, possibly a fully 3-dimensional flow field. That is, on one hand, for the simplest model for the viscosity of a mixture,  $p \leq 1$  implies a lower viscosity for regions of a high fraction of aqueous phase. Thus, regions of low drop counts will indicate a rather high viscosity with respect to neighboring regions of high concentration of drops. On

the other hand, if drop interactions are significant due to closeness among themselves, then a higher viscosity could be associated to higher concentration of drops. In both cases, the relative viscosity along the vorticity axis should be an oscillating function of position. Hence the *horizontal profile of the velocity field* along the flow direction may also show a sinusoidal variation along the z-axis—the vorticity axis—with a periodicity similar to that shown in Figure 4.8e.

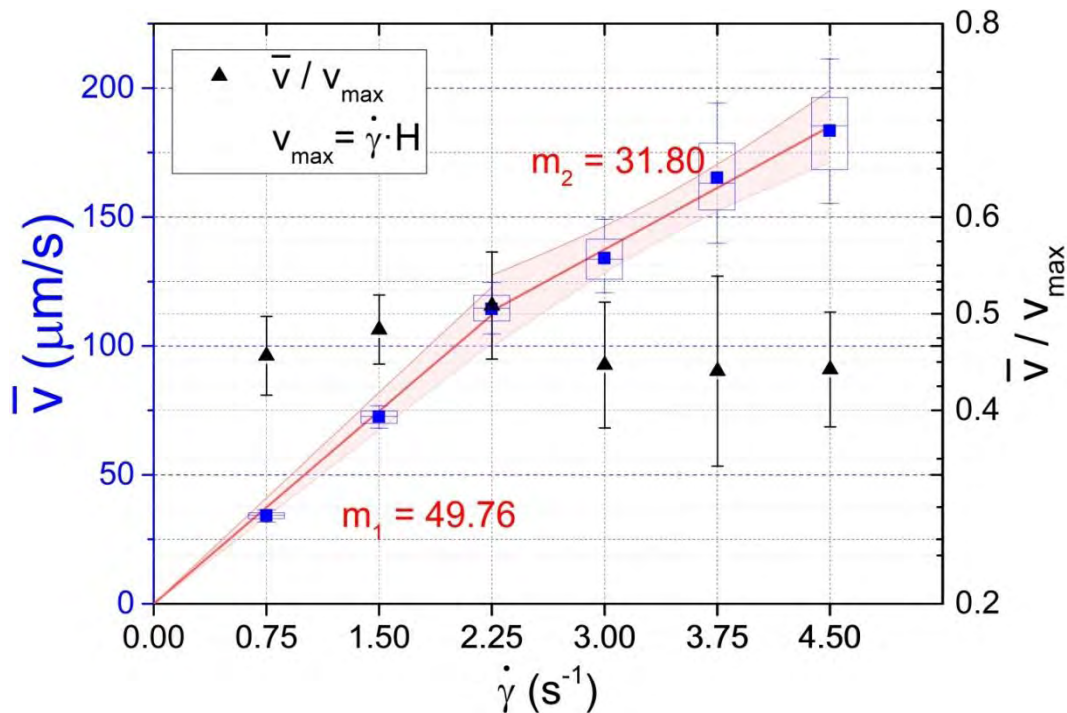
Consequently, during the constant flow regime (towards the end of the transient state and for each shear rate), the velocity of individual drops along the flow direction is determined, and mean values calculated. As well, the spatial variability of the mean velocity —across columns that belong to valleys or peaks— is evaluated. For the present analysis, the time of each frame is 1 s.

Shear Rate (s <sup>-1</sup> )	Total Number Drops	Velocity Mean (μm/s)	Standard Deviation (μm/s)	Relative Deviation
0.75	127	34.24	1.40	0.04
1.5	143	72.55	2.60	0.04
2.25	140	114.40	6.35	0.06
3	175	134.09	8.74	0.07
3.75	105	165.23	16.25	0.10
4.5	198	183.52	15.98	0.09

**Table 4.1.** Velocity of drops (randomly selected) observed for different shear rates.

Table 4.1 summarizes the observed velocities for a selection of drops for which its velocities are unambiguous. These velocity measurements are carried out with the ImageJ® software.

Figure 4.10a shows the mean velocity obtained for all shear rates, showing a linear behavior of the velocity with respect to  $\dot{\gamma}$  for the weakest flows:  $\dot{\gamma} \leq 2.25 \text{ s}^{-1}$ . The rate of increase slows down once the banded structure appears  $\dot{\gamma} \geq 3.0 \text{ s}^{-1}$ , with twice the uncertainty of evaluated speeds (See Table 4.1; right most column).



**Figure 4.10.** Average speed of drops over the complete flow domain, chosen for each shear rate: left ordinate. Also, the middle quartiles and the error bars are shown. The normalized dimensionless mean velocity wrt. the velocity of the shearing plate ( $v_{\text{max}} = \dot{\gamma} \cdot H$ ); right ordinate. Slopes  $m_1 = v \cdot \dot{\gamma}^{-1} = 50 \mu\text{m}$ , and  $m_2 = 31.8 \mu\text{m}$  attest to a slow down of the flow speed once the banded structure of the emulsion occurs. Accordingly, the slow down of the normalized velocity is homogeneous and of about 10 % for the 3 highest shear rates.

The observed increase on the standard deviation values, as the shear rate increases, is due to intrinsic difficulties in evaluating the average speed of drops in a flow that is no longer laminar, as indicated in Table 4.1, and shown in Figure 4.9. Uncertainties for measured velocities increase, especially for those flow structures

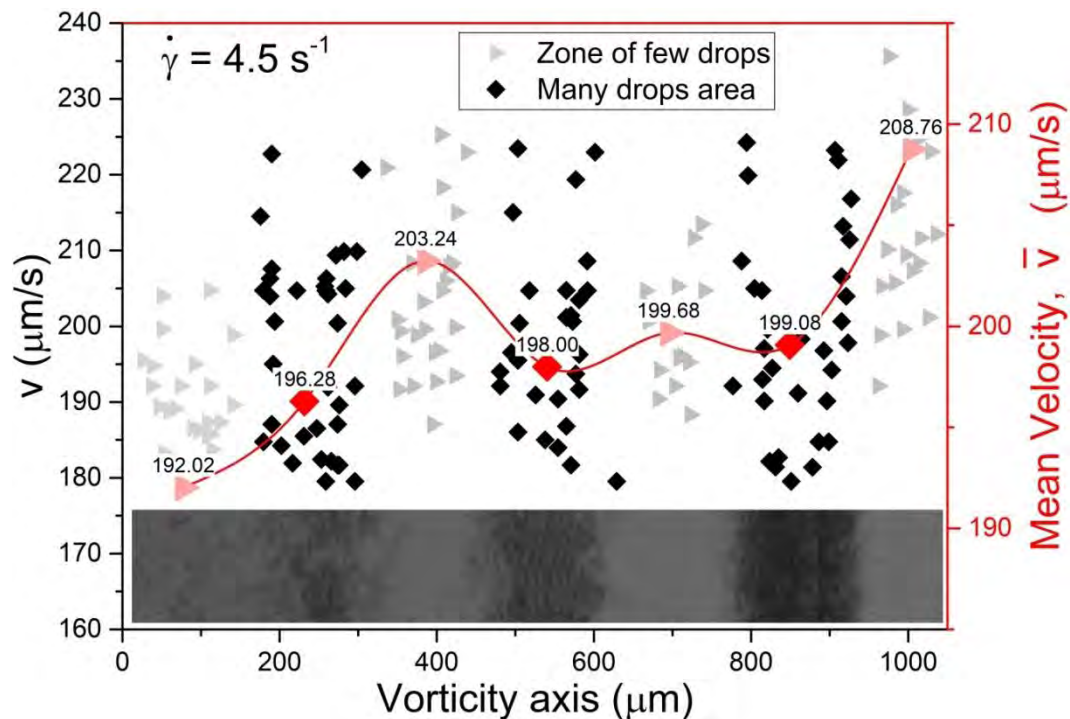
with a banded distribution of drops. This may imply two phenomena at play. *The first* one is simply an increase of collision rate between drops —in particular in the high concentration regime regions, inducing a slowdown of the measured velocity of individual drops. And *the second* may be due to a concentration-of-drops-dependent viscosity, with regions of low drop concentration associated to lower viscosity, thus, a higher velocity for a drop.

This scenario implies that the velocity profile for a lamella on the flow-vorticity plane shall show an oscillatory pattern as well. This pattern ought to be similar to the concentration of drops profile, normal to the vorticity axis. Even more, the velocity profile shall match the spacing of bands, and having higher velocities in regions of lower drop volumetric concentration.

In Figure 4.11 regions of low concentration do not have many available drops; hence, the number of data points is low. In contrast regions of high concentration of drops may present many possible candidates for their velocity calculation, but constant interaction with many neighbors limit the number of useful candidates.

As well, Figure. 4.11 shows the oscillatory character of the *mean velocity of drops* within a given region, across the vorticity axis; see red trace. Even more, the mean velocity profile shall match the spacing of bands, and having higher velocities in

regions of lower drop volumetric concentration, which can be inferred from the image of banded structure of the emulsion, at the bottom of the graph.



**Figure 4.11.** Drop velocities along the flow direction vs. their position across the vorticity axis. Left ordinate: plots the measured velocity for individual drops, for each marker. Right ordinate: the average velocity over the valley or peak of the drop distribution profile. Higher velocities coincide with regions of lower concentration of drops.

Thus, the information from Figures 4.8, 10 and 11 allow as to propose that the profile of velocities along the flow direction, spanning the full vorticity direction (that is, the  $xw$ -space or vorticity-flow plane), is non-homogenous, with a speed oscillation characterized by the same spatial frequency than the concentration of drops of the banded structure.

#### 4.2.5. The Vertical distribution of drops. The velocity field of the developed flow on the x-y plane.

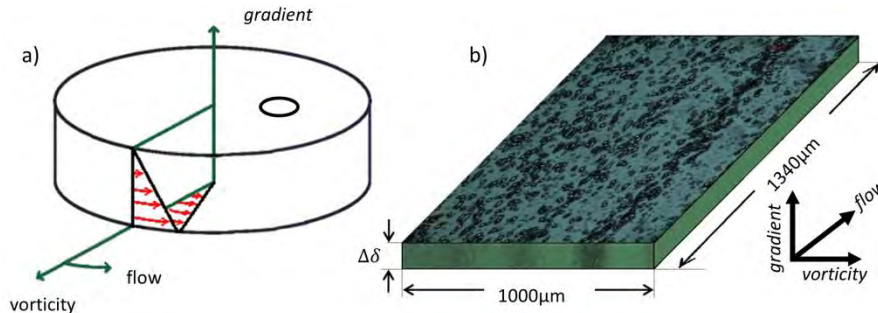
If the horizontal distribution of drops observed in Figure 4.8 induces a velocity distribution (an oscillatory velocity profile as shown in Figure 4.11) along the flow direction for all drops, then *the character of the flow field may be fully three dimensional*, even when it is generated by a flow cell with perfectly flat parallel surfaces. This assumption can be plausible due to several effects, which may occur simultaneously. Consequently, these phenomena may also indicate that *the vertical velocity profile is no longer linear*, mainly, due to a slowdown in the central lamella of the flow, as shown in Figure 4.10 for shear rates  $\dot{\gamma} \geq 3.0 \text{ s}^{-1}$ .

Even more, the slowdown of the mean flow is clearly non-homogeneous across the lamella, as seen in Figure. 4.11. These two pieces of information are very important, and suggest that the velocity along the vorticity axis is no longer zero or homogeneous. In fact, this assumption could be plausible and could be explained by the oscillatory character of the flow field that induces a lateral component of the velocity —along the vorticity direction (inducing gradients of the concentration of drops, observed in the banded structure).

That is, there must be a component of the velocity field along the vorticity direction, which is weak but characterized by an oscillatory manner, as well. This

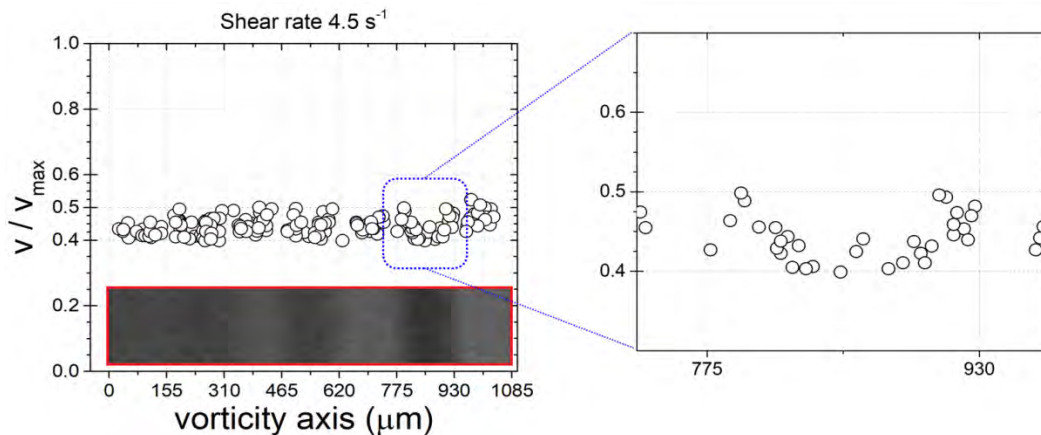


normal component of the velocity field assures the development of a banded structure. The deceleration along the flow direction plus the appearance of a lateral (vorticity) component may also indicate that the vertical velocity profile will be three-dimensional.



**Figure 4.12** (a) Scheme of the velocity profile in the flow-vorticity plane and in the gradient-flow plane, and (b) The captured image view in 3D: flow-vorticity plane about the center of the flow cell, thickness =  $\Delta\delta$ ; and side, in the gradient-vorticity plane.

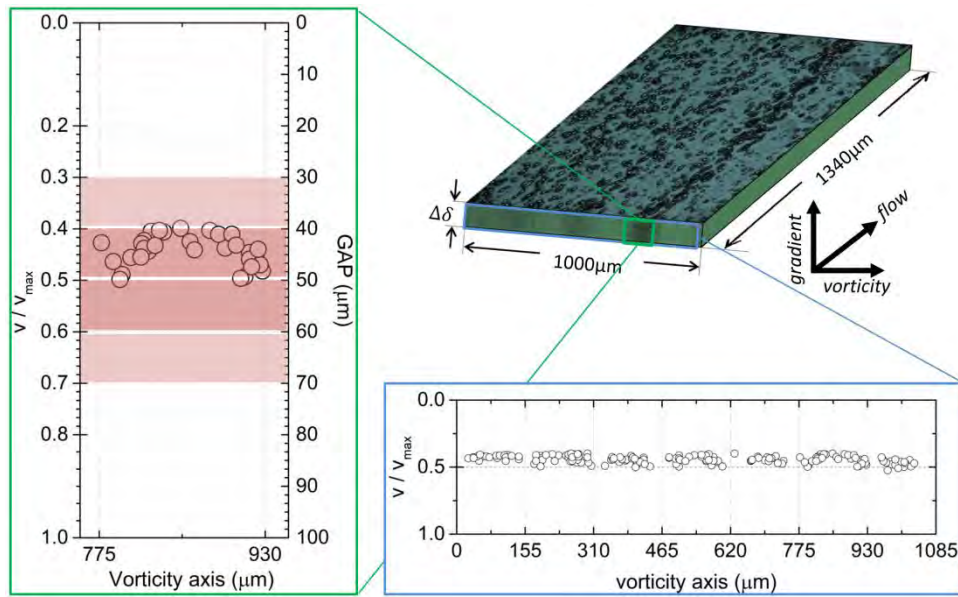
In order to study the profile of concentration of drops and the vertical velocity profile of the bands, Figure 4.12 shows the geometry of the flow cell in three dimensions and *the initial assumption of a linear, unidirectional velocity profile*. In the lower part of the profile is the maximum speed and in the upper part the zero speed (static top plate). Figure 4.12 shows velocity measurement across the vorticity axis. Please note that the plate translating at constant velocity, i.e., the lower plate of the flow cell is actually corresponds to the top value shown in Figure 4.13. It is possible to identify different bands that are separated by an approximate width of  $\sim 155 \mu\text{m}$ .



**Figure 4.13** Dimensionless speed across the vorticity direction. Bottom insert in (a) shows the zones of the better defined bands. (b) is an expanded view of the selected region (blue square region) of the most dense band.

Carrying out a characterization of *the vertical velocity of drops profile*, as shown in Figure 4.13, it is now possible to determine *the profile of the concentration of drops in a band, but now in the gradient-vorticity plane*, at least for the better defined bands. That is, this analysis attempts to elucidate whether the band structure occurs from plate to plate of the shearing cell. But given that the concentration of drops is quite large—actually, sufficiently high to preclude observation of the velocity of drops near the bottom of the flow cell—, then measurement of velocities of drops corresponds to those in the upper half of the flow field, only.

Thus, based on the velocity of individual drops and using its normalized velocity to infer its vertical position on the band, it is possible to propose a vertical profile for the concentration of drops within a high concentration band. Figure 4.13 shows possible position of drops and the corresponding upper layer where drops are located.



**Figure 4.14** Determination of the thickness of the band in the vorticity-gradient plane.

The concentration of drops inside the dotted red lamella, shown in Figure 4.14, is posited by symmetry considerations of what can only be determined with the measurement of speed of drops. The red layer is the thickness of the band without taking into account the diameters of the drops, while the green one corresponds to the suspected thickness of the high concentration of drops layer when the diameter of the drops is taken into account. The observed diameter of droplets within this band area is of the order of 17 to 20  $\mu\text{m}$ , and is also taken into account to delimit the green layer thickness. In this way, a possible (actually the minimum) complete profile is predicated, which is only a fraction of the wall-to-wall separation, implying rather thick regions above and below with only a few drops (while the lamella maintains a high concentration of drops). The

confinement parameter of the band as a whole is of  $Co = 0.4$ , which is considered in the literature as moderate confinement [21].

### 4.3. Discussion of Results

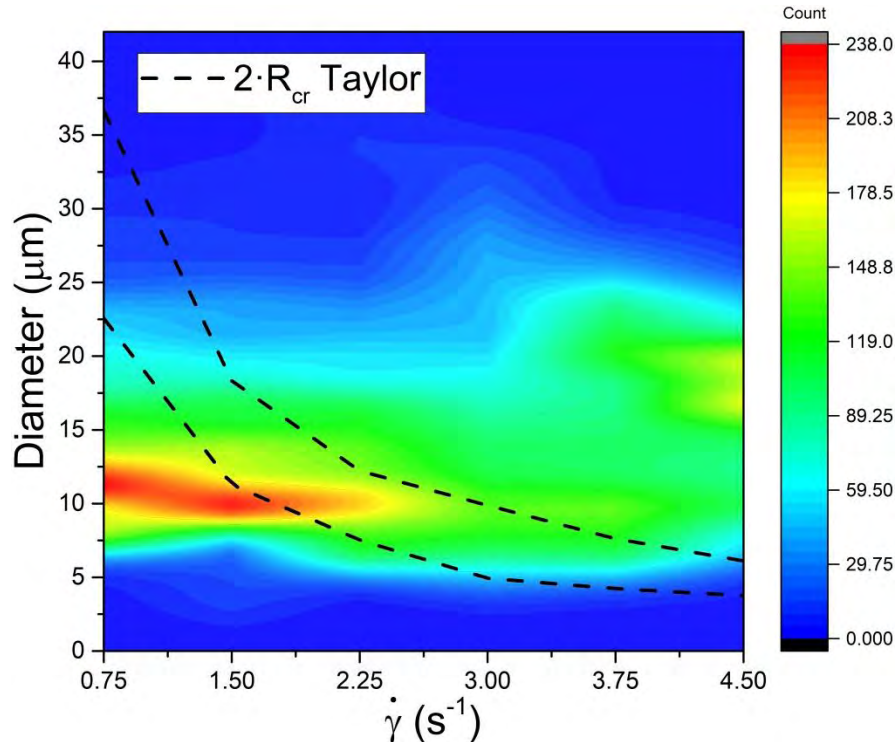
#### 4.3.1. Critical capillary in concentrated emulsions

For a single drop embedded in a continuum, with a viscosity ratio of  $p \sim 0.28$  and drop size  $r \sim 18 \mu\text{m}$ ; the literature estimates that reasonable values of the critical capillary number in a simple shear flow are about  $Ca_{cr} \sim 0.51$  [22]. In the present work, the critical capillary is  $Ca_{cr} \cong 0.21 \pm 0.07$ , which may imply that other perturbation from nearby drops can induce rupture of drops at a lower  $Ca_{cr}$ .

Recalling Taylor's model prediction for the critical capillary, for a system with a constant value of  $p$ , the value of  $Ca_{cr}$  implies that the critical radius (the largest radius value up to drops of stable shape) and the shear rate are inversely proportional. The observed discrepancy of these two values can now be used to understand a portion of the dynamics observed in the relation to the bands structure.

In other words, the critical radius of a drop decreases as the shear rate increases as shown in Figure 4.15 (the region delimited between the black dashed lines). These upper and lower limits of the critical diameter values are analytical results valid

for slow flows, according to Taylor's predictions. This Figure also shows the complete evolution of the histograms of drop size distribution for the full set of shear rates studied; the colored information portrays the histograms evaluated in Figures 3.4 and 3.5, and plotted vs.  $\dot{\gamma}$ .



**Figure 4.15.** Distribution of size of drops in the emulsion vs. the complete range of shear rates used in the experiments; frequency of drops – color coded. Comparison of the  $Ca_{cr}$  obtained for Taylor's model: Black dashed region; the delimited area represents the range of stability for single drop.

Please note that no drops smaller than 5  $\mu\text{m}$  appear, as well as drops larger than 35  $\mu\text{m}$ . The highest frequency occurs at low shear rates and for diameters of about 12  $\mu\text{m}$ . Drop elongation and rupture of these drops does not occur until  $\dot{\gamma} = 1.75 \text{ s}^{-1}$ , when  $Ca_{cr} \sim Ca_{Taylor}$ . Higher shear rates preclude the observation

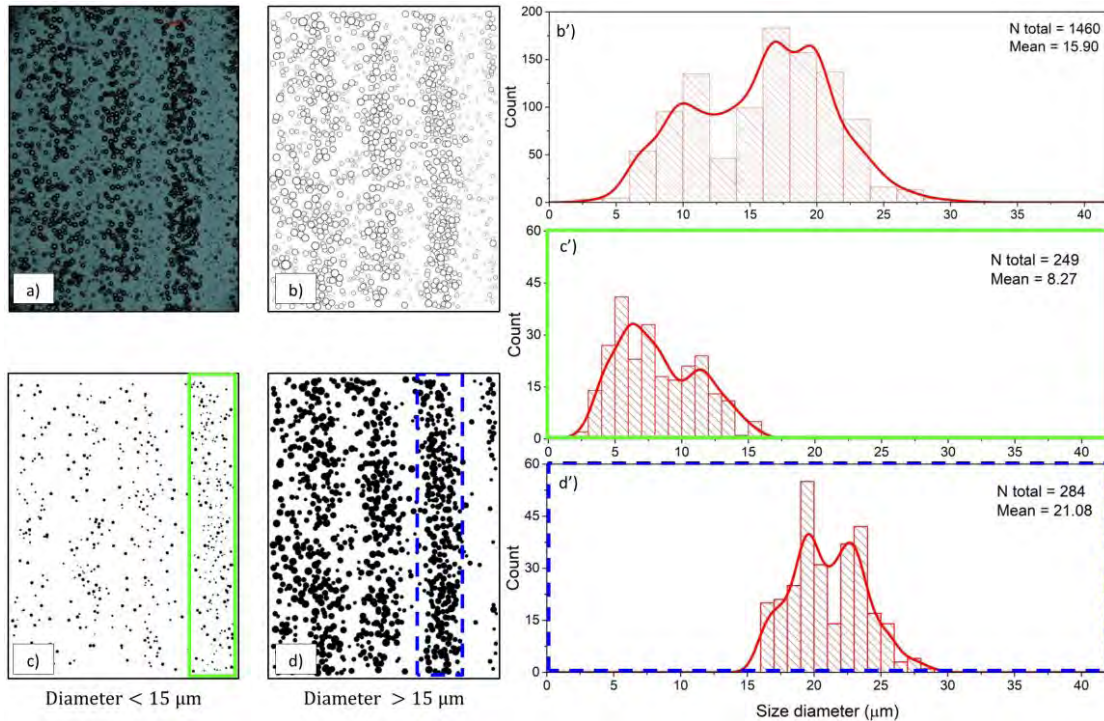
of drops with a diameter of approx.  $12\ \mu\text{m}$ , hence a coalescence mechanism for growth of drops must be balance by another of elongation and rupture of drops.

For shear rates  $\dot{\gamma} \leq 2.75\ \text{s}^{-1}$ , no drop shall be stable for diameters larger than  $12\ \mu\text{m}$ , implying that the observed stability of larger drops (i.e., about  $16\text{-}20\ \mu\text{m}$ ) should be due to other stabilizing phenomena, mainly from nearby drops and a more complex flow regime. And for  $\dot{\gamma} \sim 4.5\ \text{s}^{-1}$ , drops larger than  $8\ \mu\text{m}$  only exist when strong interaction with other drops occurs and the flow regime is more complex than simple shear flow. Even more, these mechanisms appear to inhibit the existence of drop larger than  $25\ \mu\text{m}$ .

Figure 4.16 shows the location of the larger drops inside the image, which are mostly contained within the high concentration band while smaller ones appear mainly inside the valleys between bands. The average diameter of the drops inside the bands is above the critical diameter of the single drop Taylor model (See Figure 4.15). In this way,  $Ca_{cr} < Ca_{Taylor}$  even in this dilute regime, and  $Ca_{cr} \ll Ca_{Taylor}$  for drops confined in concentrated regions.

Therefore, in this Chapter is presented another possible explanation for the observed behavior in concentrated emulsions with bands present. This explanation is based more on the fact that the observed concentration gradients is concomitant of correlated gradients of the velocity field along the direction of the

flow, as well as the appearance of a non-zero component of the velocity field along the direction of the vorticity.



**Figure 4.16.** Correlation of position of a drop inside a slice of the flow-vorticity plane and the expected diameter of the drop; a) experimental data; b) processed image selecting spherical drops only: sum of all spherical drops, color coded by size: total number of drops counted  $n_{drops} = 1460$ , with volume  $V_{drops} = 4.6 \times 10^7 \mu\text{m}^3$ ; c) selection of drops with diameters  $< 15 \mu\text{m}$ , contained in green area; d) selection of drops of diameters  $> 15 \mu\text{m}$ , contained in blue area; and b') initial (top) histogram for drops after 2410 s, at  $\dot{\gamma} = 4.5 \text{ s}^{-1}$ , c') histogram of drops in valleys (middle) and d'') histogram for flow region of high concentration (bottom).

Previous attempts to explain the observed distributions of drops were based upon the critical capillary number criteria. That is, this idea was reported by Macosko in 1995 [27] and rests upon the assumption that emulsions are slightly concentrated systems, where the limiting case of Taylor's model can be referenced. But it is important to emphasize that the opposite is also stated in the literature by Jansen [28]. In this work, drops inside the bands exceed the critical size due to a dynamic

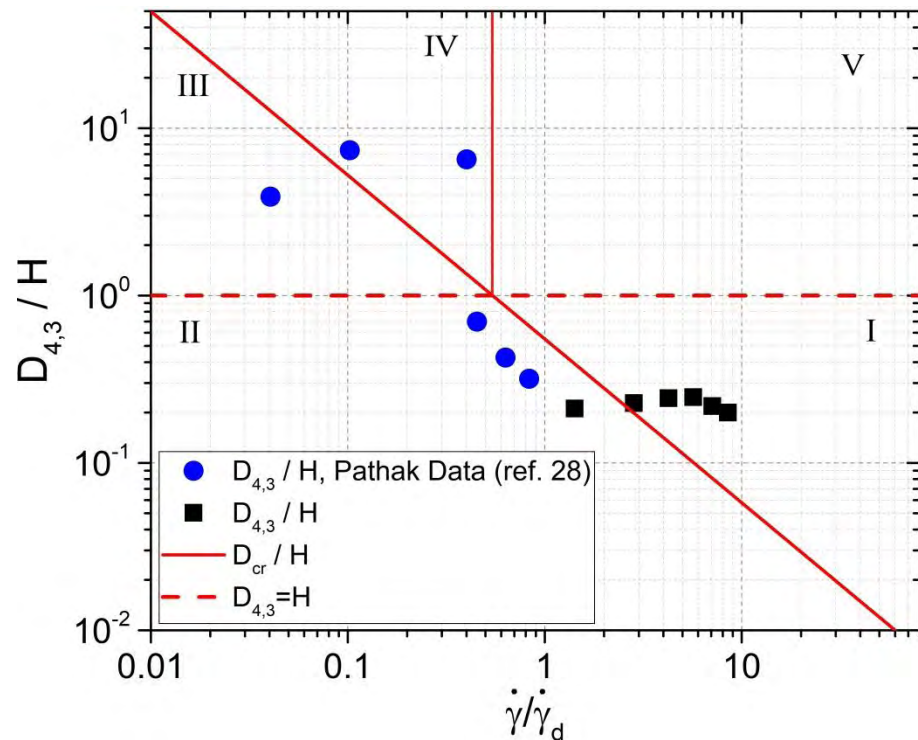
equilibrium, between the mechanisms that modify the morphology and the stress fields (by nearby neighbors, non-shearing motion, etc.), and eventually increases *the mean viscosity within the band* [24-26].

The probability of contact for drops inside the bands is highest, giving coalescence a probable role, while close neighbors modified the stress field about a drop, decreasing rupture. It is then plausible that the average diameter of drops grows to a value that would not be expected taking into account a reduced model for the emulsion, and more if we compare it with the simplest system: the Taylor's model. However, a band of drops may impose a flow regime outside its core that is similar to that of a drop in the string of necklace form.

In Pathak's observations [28], four regimes are proposed, shown in Figure 4.17. Pathak attempts to predict possible morphologies in concentrated dispersions. The regimes classification is based on the dimensionless and *normalized* shear rate and the volumetric relation of the diameter of drops  $D_{4,3} / H$ . The first regime corresponds to capillary number of drops exceeding the critical capillary, while the diameter of the drops is much less than the separation of the plates. The second regime corresponds to the case when the capillary number of drops is less than the critical capillary, and they are sufficiently dispersed that no hydrodynamic interaction is relevant in relation to neighbors or walls. The third



regime is the case of highly deformed drops (i.e., oblate ellipsoids). The fourth regime is the case where the capillary number of drops (based on Taylor's model) is higher than the critical capillary, and the diameter of drops is greater than the separation of the plates. In this regime, drops with a highly deformed shape — strings or necklaces— are present, and provide a similar hydrodynamic environment to the banded structure of the emulsion. Moreover, the last regime (the fifth), is for the case where the diameter of the strings are below the separation of the plates, but the associated capillary number when strings are observed is less than the critical capillary of the strings, in conditions of low confinement.



**Figure 4.17.** Adaptation of Pathak's representation of the regimes in the scenarios of concentrated emulsion morphologies.  $\dot{\gamma}_d$  is the shear rate at which Taylor theory predicts the maximum droplet radius ( $\dot{\gamma}_d = \sigma_{12}/(H \cdot \eta_m)$ ).

In Figure 4.17, the results of the experiments reported in this Chapter are indicated with data (black squares) points. Pathak's data (Figure 11, ref [28]) correspond to data (blue circles) points and corresponds to the behavior observed when an emulsion shows long strings. In principle, the results presented here correspond to Pathak's First Case, where drops are agglutinated and unstable because they stretch and break. However, the detailed structure and possible flow consideration that may induce such spatial distributions has not been studied experimentally, as far as it has been consulted in the literature, which is significant.

These data clearly do not match, but under these conditions, both, strings, like bands, present stability, which might occur due to the influence of the confinement of the walls effect (on the band or the strings). This confinement leads to the existence of large drops that overcome the rupture, in both cases: Pathak with strings and the work presented in this Chapter with bands. These anisotropic structures are undoubtedly part of a transient state, which can be a consequence of deformations in bulk or in concentrated emulsion.

The width of the bands is approximately  $155\ \mu\text{m}$  measured directly from the images. The bands move in a centripetal direction. The centripetal movement is a product of the accommodation of the areas of higher viscosity and those of lower

viscosity [23-26]. At the present time it is not possible to propose a mechanism that explains this phenomenon.

#### 4.4. Chapter Conclusions

The formation of bands, perpendicular to the direction of the vorticity axis, is not well understood [2, 17, 20]. The phenomenon of band formation is produced with relative simplicity, as is the case when mixing two immiscible Newtonian fluids, with a low viscosity ratio  $p < 1$ , without surfactants and for specific shear rate values [10]. A relatively plausible explanation is to attribute to the competing effect of coalescence and rupture, wherein values of  $p$  less than one the coalescence predominate [19], and then the formation of large drops of a size determined by the separation of the discs [11], will end in the formation of the pearl neck structures, as evidenced in the images of the previous Chapter (Figure 3.4). However, it is an open subject of study.

In this Chapter it is hypothesized that the curvature of the flow field has no significant role in the formation of bands, as posited by Caserta, et al. [1,2] — although more work is required and thus still unconfirmed— work that is projected into the future. Extrapolating the observations and taking as reference the work of Jeffrey Byars [30], it can be hypothesized that the observed bands

corresponds to a sector of an Archimedean spiral [30]. We still cannot answer this question: if these bands are concentric rings or are spirals and this quest was not part of objectives of this work.

However, here I show that a detailed analysis of the dynamics of the bands structures is possible, as well as measurement of the flow field anomalies that are simultaneously observed. That the *local viscosity* of the emulsion increases in areas of higher concentration of drops, and regions of lower concentration of drops imply a lower viscosity, which causes the morphology of the emulsion to change macroscopically.

## 4.5. References

- [1] Caserta S, Simeone M, Guido S. Shear banding in biphasic liquid-liquid systems. *Physical review letters*. 2008 Apr 3;100(13):137801.
- [2] Caserta S, Guido S. Vorticity Banding in Biphasic Polymer Blends. *Langmuir*. 2012;28(47):16254-62.
- [3] Wilkins GM, Olmsted PD. Vorticity banding during the lamellar-to-onion transition in a lyotropic surfactant solution in shear flow. *The European Physical Journal E*. 2006 Oct 1;21(2):133.
- [4] Highgate D. Particle migration in cone-plate viscometry of suspensions. *Nature*. 1966 Sep;211(5056):1390.
- [5] Van der Gucht J, Lemmers M, Knoben W, Besseling NA, Lettinga MP. Multiple shear-banding transitions in a supramolecular polymer solution. *Physical review letters*. 2006 Sep 7;97(10):108301.
- [6] Ciamarra MP, Coniglio A, Nicodemi M. Shear instabilities in granular mixtures. *Physical review letters*. 2005 May 11;94(18):188001.
- [7] Olmsted PD. Perspectives on shear banding in complex fluids. *Rheologica Acta*. 2008 Apr 1;47(3):283-300.
- [8] Olmsted PD, David Lu CY. Phase coexistence of complex fluids in shear flow. *Faraday Discussions*. 1999;112:183-94.
- [9] Fielding SM. Complex dynamics of shear banded flows. *Soft Matter*. 2007;3(10):1262-79.
- [10] Migler KB. String formation in sheared polymer blends: Coalescence, breakup, and finite size effects. *Physical Review Letters*. 2001 Feb 5;86(6):1023.
- [11] Salmon JB, Colin A, Manneville S, Molino F. Velocity profiles in shear-banding wormlike micelles. *Physical review letters*. 2003 Jun 6;90(22):228303.
- [12] Simeone M, Sibillo V, Tassieri M, Guido S. Shear-induced clustering of gelling droplets in aqueous biphasic mixtures of gelatin and dextran. *Journal of Rheology*. 2002;46(5):1263-78.
- [13] Montesi A, Peña AA, Pasquali M. Vorticity alignment and negative normal stresses in sheared attractive emulsions. *Physical review letters*. 2004 Feb 6;92(5):058303.
- [14] Osuji CO, Weitz DA. Highly anisotropic vorticity aligned structures in a shear thickening attractive colloidal system. *Soft Matter*. 2008;4(7):1388-92.
- [15] Pathak JA, Davis MC, Hudson SD, Migler KB. Layered droplet microstructures in sheared emulsions: finite-size effects. *Journal of colloid and interface science*. 2002 Nov 15;255(2):391-402.

- [16] Migler KB. String formation in sheared polymer blends: Coalescence, breakup, and finite size effects. *Physical Review Letters*. 2001 Feb 5;86(6):1023.
- [17] Grace HP. Dispersion phenomena in high viscosity immiscible fluid systems and application of static mixers as dispersion devices in such systems. *Chemical Engineering Communications*. 1982 Mar 1;14(3-6):225-77.
- [18] De Bruijn RA. Tipstreaming of drops in simple shear flows. *Chemical engineering science*. 1993 Jan 1;48(2):277-84.
- [19] Leal LG. Flow-induced coalescence of drops in a viscous fluid. *Physics of fluids*. 2004 Jun;16(6):1833-51.
- [20] Jansen KM, Agterof WG, Mellema J. Droplet breakup in concentrated emulsions. *Journal of rheology*. 2001 Jan;45(1):227-36.
- [21] Vananroye A, Van Puyvelde P, Moldenaers P. Effect of confinement on droplet breakup in sheared emulsions. *Langmuir*. 2006 Apr 25;22(9):3972-4.
- [22] Karam HJ, Bellinger JC. Deformation and breakup of liquid droplets in a simple shear field. *Industrial & Engineering Chemistry Fundamentals*. 1968 Nov;7(4):576-81.
- [23] Taylor GI. The viscosity of a fluid containing small drops of another fluid. *Proc. R. Soc. Lond. A*. 1932 Oct 1;138(834):41-8.
- [24] Taylor GI. The formation of emulsions in definable fields of flow. *Proc. R. Soc. Lond. A*. 1934 Oct 1;146(858):501-23.
- [25] Choi SJ, Schowalter WR. Rheological properties of nondilute suspensions of deformable particles. *The Physics of Fluids*. 1975 Apr;18(4):420-7.
- [26] Sundararaj U, Macosko CW. Drop breakup and coalescence in polymer blends: the effects of concentration and compatibilization. *Macromolecules*. 1995 Apr;28(8):2647-57.
- [27] Jansen KM, Agterof WG, Mellema J. Droplet breakup in concentrated emulsions. *Journal of rheology*. 2001 Jan;45(1):227-36.
- [28] Pathak JA, Migler KB. Droplet- String Deformation and Stability during Microconfined Shear Flow. *Langmuir*. 2003 Oct 14;19(21):8667-74.
- [29] Mckinley GH, Öztekin A, Byars JA, Brown RA. Self-similar spiral instabilities in elastic flows between a cone and a plate. *Journal of Fluid Mechanics*. 1995 Feb;285:123-64.
- [30] Byars JA, Öztekin A, Brown RA, Mckinley GH. Spiral instabilities in the flow of highly elastic fluids between rotating parallel disks. *Journal of Fluid Mechanics*. 1994 Jul;271:173-218.



## *Chapter 5: In situ measurement of interfacial tension of an emulsion*

The measurement of the interfacial tension by dynamic methods has assumed importance in the last decades [12], by overcoming the experimental difficulties of the conventional methods (pendant drop, sessile drop and spinning drop methods), as they are the equality in the densities of the polymeric materials (phases) and their high viscosities. Of the dynamic methods to determine the value of interfacial tension is used in the present chapter is the deformed drop retraction (DDR) method. The following chapter describes the interfacial tension measurement of isolated drops of the diluted emulsion, in the flow cell (CSS450) (see chapter 2). The GAP used for this experiment is 100  $\mu\text{m}$ , and the shear rate for the steady state is  $1.5 \text{ s}^{-1}$  before stopping the flow. The interfacial tension is



measured by the observation of the evolution (relaxation) of the shape of a drop, previously deformed by a simple flow.

### 5.1. Deformed Drop Retraction Method

The Deformed Drop Retraction (DDR) allows determining the interfacial tension between two liquids, from the relaxation of a drop, initially deformed [1]. Assuming that the shape of the deformed drop is an ellipsoid of revolution and its final shape is a sphere of radius  $R_0$ . The equation 5.1, describes the evolution of the shape of a drop after the cessation of the flow. This equation is obtained from Taylor's theory [5] of the first order according to Rallison's formulation.

$$D = D_0 \cdot \exp \left\{ -t \cdot \left[ \frac{40(p+1)}{(2p+3) \cdot (19p+16)} \cdot \frac{\sigma_{12}}{\eta_m \cdot R_0} \right] \right\}$$

$$D = D_0 \cdot \exp \left\{ -\frac{t}{\tau_{DDRM}} \right\},$$
(5.1)

with  $D = (L' - B)/(L' + B)$ ,  $p$  is the viscosity ratio,  $\eta_m$  is the viscosity of the matrix,  $\sigma$  is the interfacial tension between the two liquids in contact,  $D_0$  is the deformation at  $t = 0$ . This equation is valid for small deformations, i.e.,  $D_T$  less than 0.35.

When plotting  $\ln(D_T / D_0)$  vs  $t$ , a straight line is observed, and the slope of the straight line is given by equation 5.2 from which the interfacial tension can be determined.

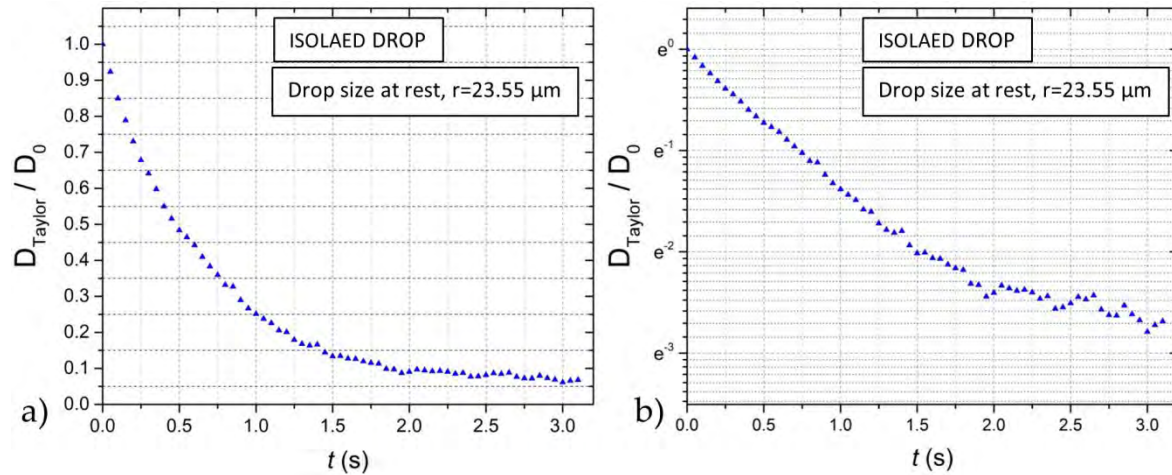
$$\tau_{DDRM} = \frac{1}{slope} = - \left[ \frac{(2p + 3) \cdot (19p + 16)}{40(p + 1)} \cdot \frac{\eta_m \cdot R_0}{\sigma_{12}} \right]. \quad (5.2)$$

In principle, this equation is only valid for Newtonian systems. However, work with viscoelastic liquids is reported [19].

## 5.2. Time Constant

The constant time is the time it takes a system to decay 63.2 % of its maximum value. Similarly, the constant time for the present work is the time required for the droplet to reach a deformation of 37.8 % [20].

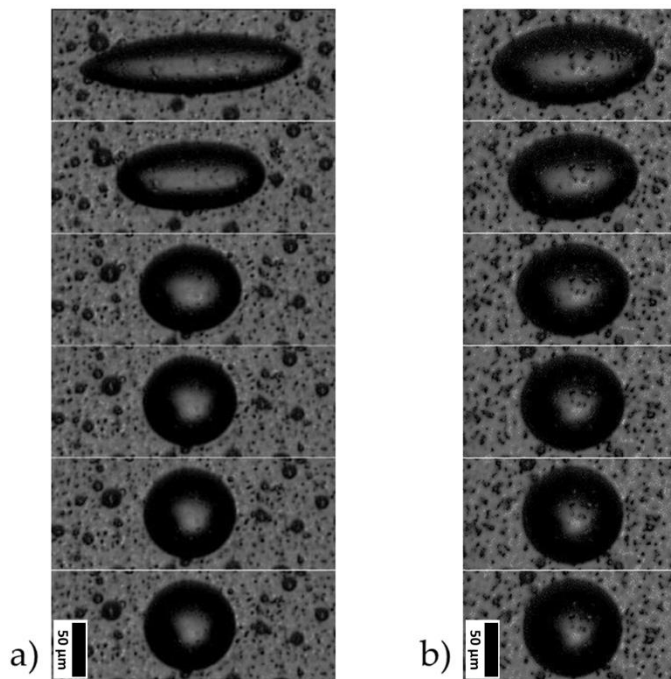
Physically, the time constant represents the elapsed time required for the droplet retraction response to decay to zero if the system had continued to decay at the initial rate, because of the progressive change in the rate of decay the response will have actually decreased in value to  $1/e^\tau \approx 36.8\%$  in this time (say from a step decrease) [21]



**Figure 5.1.** a) Taylor deformation parameter normalized by the initial deformation of an isolated drop of radius  $23.55 \mu\text{m}$ , b) The same deformation in logarithmic scale. The shear rate for the steady state is  $1.5 \text{ s}^{-1}$ .

Figure 5.1a shows the Taylor deformation parameter and in Figure 5.1b the Taylor deformation parameter is linearized with the logarithmic scale. It also shows the existence of an experimental limit in the resolution of the measurement of the droplet axes when retracting, this is observed when (see figure 5.1b) the behavior of the Taylor deformation parameter, is no longer linear; which happens after  $t \cong 2.5$ .

In this chapter, the representation of constant time is used to determine the ranges and apply the DDR method for the determination of the interfacial tension. The used  $\tau$  ranges to determine the interfacial tension are:  $1 < \tau < 1.5$ ,  $1.5 < \tau < 2$ ,  $2 < \tau < 2.5$  and  $1 < \tau < 2$ . These times are chosen, considering that the deformations of the droplets must be small ( $D_T < 0.35$ ) so that their behavior is linear.



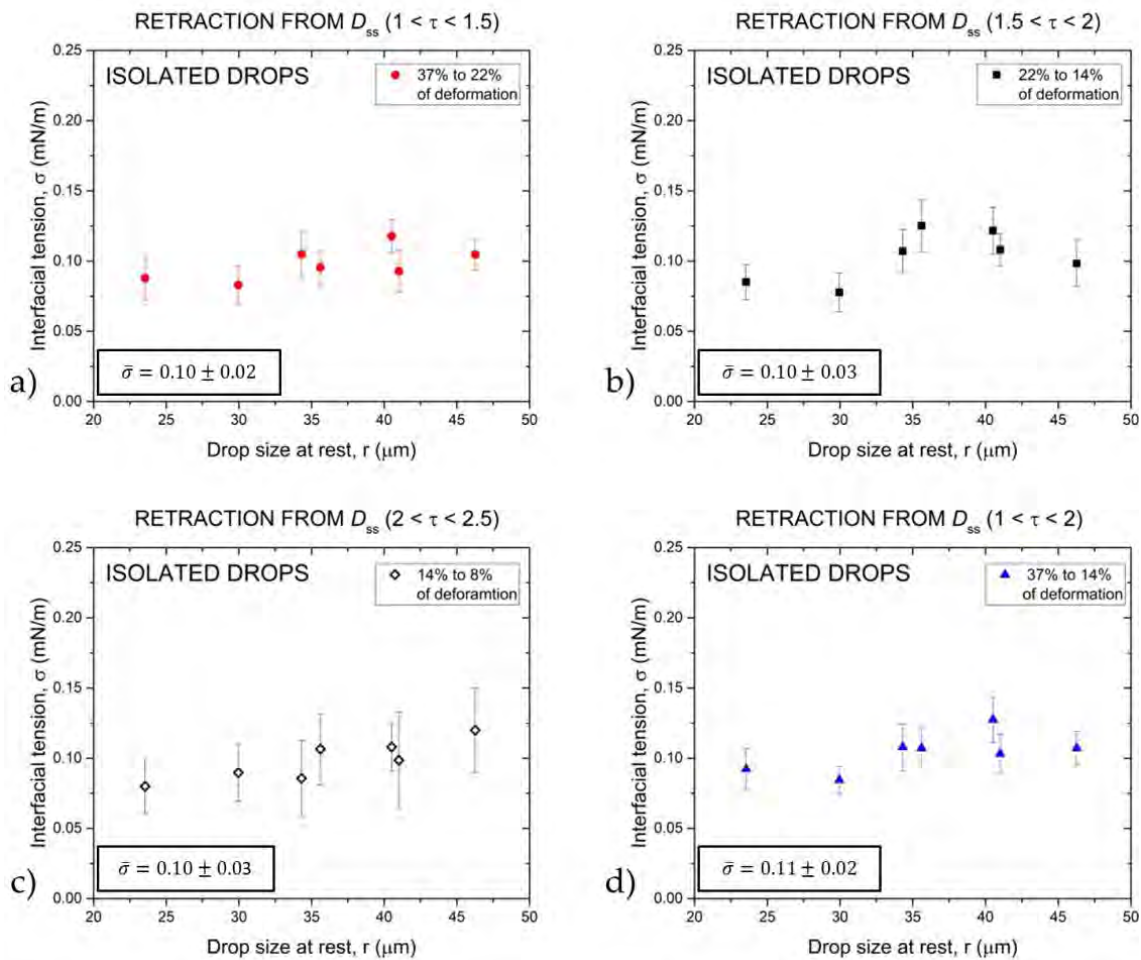
**Figure 5.2.** Shows the retraction of a drop of a)  $r = 34.31 \mu\text{m}$  and b)  $r = 35.61 \mu\text{m}$  for the shear rate of  $3.0 \text{ s}^{-1}$  and  $1.5 \text{ s}^{-1}$  respectively for  $\tau = 0, \tau = 0.5, \tau = 1, \tau = 1.5, \tau = 2$  and  $\tau = 2.5$  (top-down)

In the figure 5.2 two sequences of images of two drops are shown at a shear rate of  $3.0 \text{ s}^{-1}$  and  $1.5 \text{ s}^{-1}$ ; for times  $\tau = 0, \tau = 0.5, \tau = 1.5, \tau = 1.5, \tau = 2$  and  $\tau = 2.5$ . It is observed that the deformations in the steady state are different, for this reason the measurement of the interfacial tension for small deformations is emphasized ( $\tau > 1$ ).

### 5.3. Measurement of the interfacial tension

For the realization of this section of the work experimental, a change of camera is made to capture images, to achieve 20 fps black and white video, and thus more information is obtained in the relaxation of the droplets. The camera used for this

section is the Pixelink PL-B953U; specifications are detailed in Chapter 2. The observations were made for two shear rates,  $1.5 \text{ s}^{-1}$  and  $3.0 \text{ s}^{-1}$ ; but the measurements were made for the shear rate to  $1.5 \text{ s}^{-1}$ . The interfacial tension measurement it is performed, with the isolated drops.



**Figure 5.3.** Measurement of the interfacial tension for small deformation ( $D_T < 0.35$ ), in isolated drops. a) Interfacial tension values for the deformation range from 37 % to 22 %. b) Interfacial tension values for the deformation range from 22% to 14%.c) Interfacial tension values for the deformation range from 14% to 8%. d) Interfacial tension values for the deformation range from 37% to 14%.

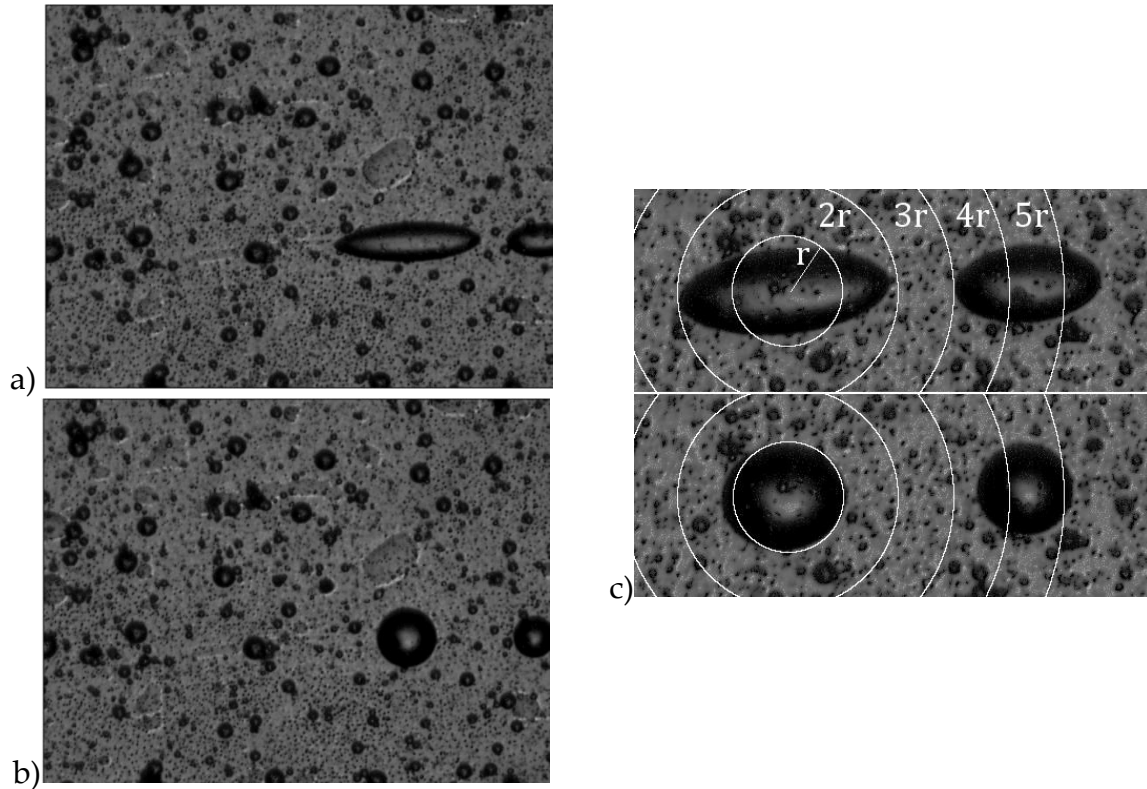
In the figure 5.3 shows the calculated value of the interfacial tension; considering equation 5.2. The shear rate for the steady state is  $1.5 \text{ s}^{-1}$ . Figure 5.3 shows the

interfacial tension measurement for the  $1 < \tau < 1.5$ ,  $1.5 < \tau < 2$ ,  $2 < \tau < 2.5$  and  $1 < \tau < 2$ ; which correspond to 37 % to 22 %, 22 % to 14 %, 14 % to 8 % and 37 % to 14 % of deformation respectively. The mean value of the interfacial tension for each range is observed in the lower left of each graph.

The methodology for future work is proposed in the following sections. For future work, the relationship between the measurement of the interfacial tension and the presence of neighboring droplets and the degree of confinement,  $Co$ . Some aspects of the experimental work have been advanced, this are described in the following section.

#### **5.4. Experimental progress of the proposal**

The shear rate that was worked in principle (it is expected to expand the range) was,  $\dot{\gamma} = 1.5 \text{ s}^{-1}$  and  $\dot{\gamma} = 3.0 \text{ s}^{-1}$ . The separation between the plates remains the same,  $100 \text{ }\mu\text{m}$ . Repeat the procedure explained in Chapter 3 to place the sample. It starts with a shear rate of  $1.5 \text{ s}^{-1}$  and is maintained for approximately 300 s where the flow stops, and the relaxation of the drops in the field of vision is observed, in figure 5.4 it is shown just before the flow stops and when the drops are at complete rest. This procedure is repeated with 10 drops for each shear rate. In figure 5.4 a-b, the largest drop, its radius is  $30 \text{ }\mu\text{m}$ .



**Figure 5.4.** a) Just when the flow stops, b) When the drop recovers its spherical shape, the time between a) and b) is 8 s and c) presents the distance in which they are considered neighbors. For stationary flow, the separation distance is of the two drops is  $r$  and in steady state  $\sim 2.5r$ .

After the capture of images from the stationary deformation of the drop to its spherical shape, it is maintained for approximately 200 s to restart the flow, when the drops that are observed achieve a stationary deformation, the flow is stopped again. The procedure is repeated twenty times for each shear rate. Fourteen drops were chosen for a shear rate effort of  $1.5 \text{ s}^{-1}$  and 10 drops for a shear rate of  $3.0 \text{ s}^{-1}$ . In each group of shear rate, they were classified into two groups, with a neighbor, and without a neighbor.

	<b>R<sub>0</sub></b> <b>(<math>\mu\text{m}</math>)</b>	<b>Shear Rate 1.5s<sup>-1</sup></b> <b>D<sub>0</sub>'<sub>Taylor</sub></b>	<b>R<sub>0</sub></b> <b>(<math>\mu\text{m}</math>)</b>	<b>Shear Rate 3.0s<sup>-1</sup></b> <b>D<sub>0</sub>'<sub>Taylor</sub></b>
<b>Isolated drop</b>	23.55	0.11	21.41	0.30
	29.96	0.33	27.61	0.36
	34.31	0.14	28.03	0.43
	35.61	0.14	30.73	0.46
	40.51	0.35	31.63	0.45
	41.01	0.31	32.94	0.51
	46.27	0.33	33.42	0.51
<b>Neighbors present</b>	17.11	0.06	28.07	0.51
	28.90	0.18	36.05	0.45
	29.78	0.20	38.70	0.47
	29.80	0.21		
	40.63	0.29		
	41.36	0.28		
	50.49	0.43		

**Table 5.1.** Data of the drops with neighbors and isolated. The radius of the droplets is shown when their relaxation is total (0% deformation, spherical drop)

A drop is defined as having neighbors when the distance between its centers in a state of rest is less than five times its radius. And without neighbors when the distance between their centers is greater than five times their radius, as shown in Figure 5.4c the distance between the drops is considered to be smaller in a steady state of flow. Image processing after capture is done with the ImageJ® software and numerical processing of the data obtained is done with the Originlab® software.

There is a series of definitions in the literature for the deformation (relaxation) of a drop. They are shown below to identify which differences and their correlation with the use of the DDR method. The initial deformations for each of the definitions are defined below:



Deformation of Taylor 
$$D'_{Taylor} = \frac{L' - W}{L' + W} \quad (5.3)$$

Deformation of Hencky 
$$\Gamma' = \ln\left(\frac{L'}{2R_0}\right) \quad (5.4)$$

Deformation of Mo 
$$D'_{Mo} = L'^2 - W^2 \quad (5.5)$$

Deformation (Nameless) 
$$D' = \ln\left(\frac{L'^2}{(2R)^2}\right) \quad (5.6)$$

Deformation (Nameless) 
$$D' = \frac{L'^2 - W^2}{(2R)^2} \quad (5.7)$$

All these deformations tend to zero in the process of droplet retraction, the initial condition for the use of the Method.

## 5.5. Some Results

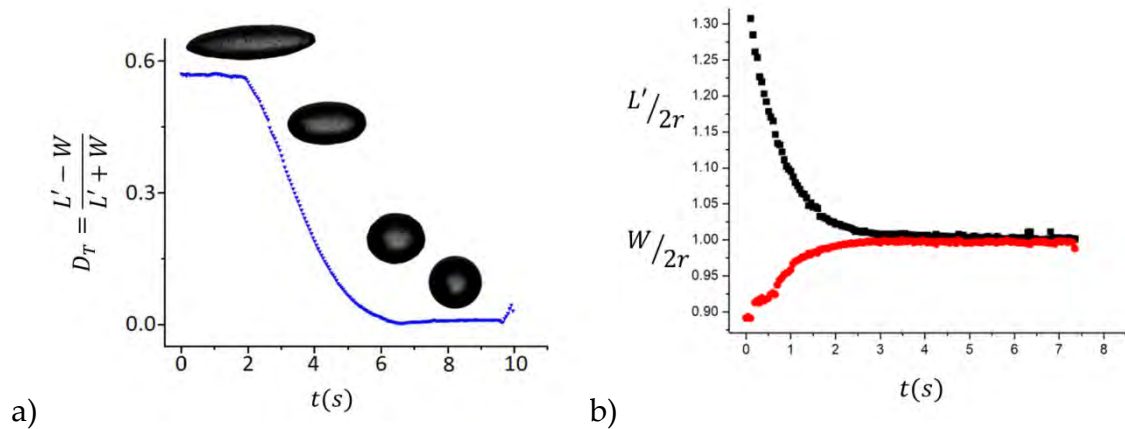
Two shear forces  $1.5 \text{ s}^{-1}$  and  $3.0 \text{ s}^{-1}$  are used to measure the interfacial tension of the emulsion. The presence of neighboring droplets at the time of stopping the flow is classified as illustrated in Figure 5.4c; the aim is to determine the variation of the interfacial tension value by the DDR method with and without neighbors. For each of the drops, the projected Taylor deformation is calculated until it reaches its spherical shape. In all deformation definitions (equation 5.3 to 5.7) they

are set to a constant decay exponential. Figure 5.3a shows the two-drop image sequences at a shear rate of  $1.5 \text{ s}^{-1}$ ; for times  $\tau = 0, \tau = 0.5, \tau = 1.5, \tau = 1.5, \tau = 2$  and  $\tau = 2.5$ . The initial deformation and interfacial tension values are shown in table 5.2.

		$\dot{\gamma} = 1.5 \text{ s}^{-1}$					$\dot{\gamma} = 3.0 \text{ s}^{-1}$						
		100-61	100-37	22-14	14-8	100-61	100-37	22-14	14-8	100-61	100-37	22-14	14-8
		%	%	%	%	%	%	%	%	%	%	%	%
	$R_0$	$D_0$ Taylor	$\sigma_1$	$\sigma_2$	$\sigma_3$	$\sigma_4$	$R_0$	$D_0$ Taylor	$\sigma_1$	$\sigma_2$	$\sigma_3$	$\sigma_4$	
	( $\mu\text{m}$ )		(mN/m)	(mN/m)	(mN/m)	(mN/m)	( $\mu\text{m}$ )		(mN/m)	(mN/m)	(mN/m)	(mN/m)	
Isolated drop	23.55	0.11	0.07	0.06	0.13	--	21.41	0.30	0.16	0.17	0.12	0.12	
	29.96	0.33	0.05	0.05	0.04	0.09	27.61	0.36	0.16	0.18	0.30	0.21	
	34.31	0.14	0.10	0.12	0.12	0.07	28.03	0.43	0.12	0.15	0.18	0.13	
	35.61	0.14	0.15	0.13	0	--	30.73	0.46	0.11	0.13	0.25	0.26	
	40.51	0.35	0.06	0.07	0.14	--	31.63	0.45	0.17	0.20	0.18	0.27	
	41.01	0.31	0.06	0.07	0.08	0.10	32.94	0.51	0.10	0.13	0.20	0.29	
	46.27	0.33	0.06	0.08	0.10	0.12	33.42	0.51	0.10	0.12	0.26	0.24	
Neighbors present	17.11	0.06	0.09	0.09	0.06	--	28.07	0.51	0.09	0.12	0.21	--	
	28.90	0.18	0.07	0.08	0.11	0.17	36.05	0.45	0.13	0.15	0.26	0.21	
	29.78	0.20	0.09	0.09	0.03	--	38.70	0.47	0.12	0.15	0.23	0.22	
	29.80	0.21	0.08	0.08	0.09	0.06							
	40.63	0.29	0.10	0.09	0.19	0.14							
	41.36	0.28	0.06	0.08	0.12	0.08							
	50.49	0.43	0.05	0.06	0.10	--							

**Table 5.2.** Interfacial tension values by the DDR method, for the times  $\tau = 0, \tau = 0.5, \tau = 1.5, \tau = 1.5, \tau = 2$  and  $\tau = 2.5$ .

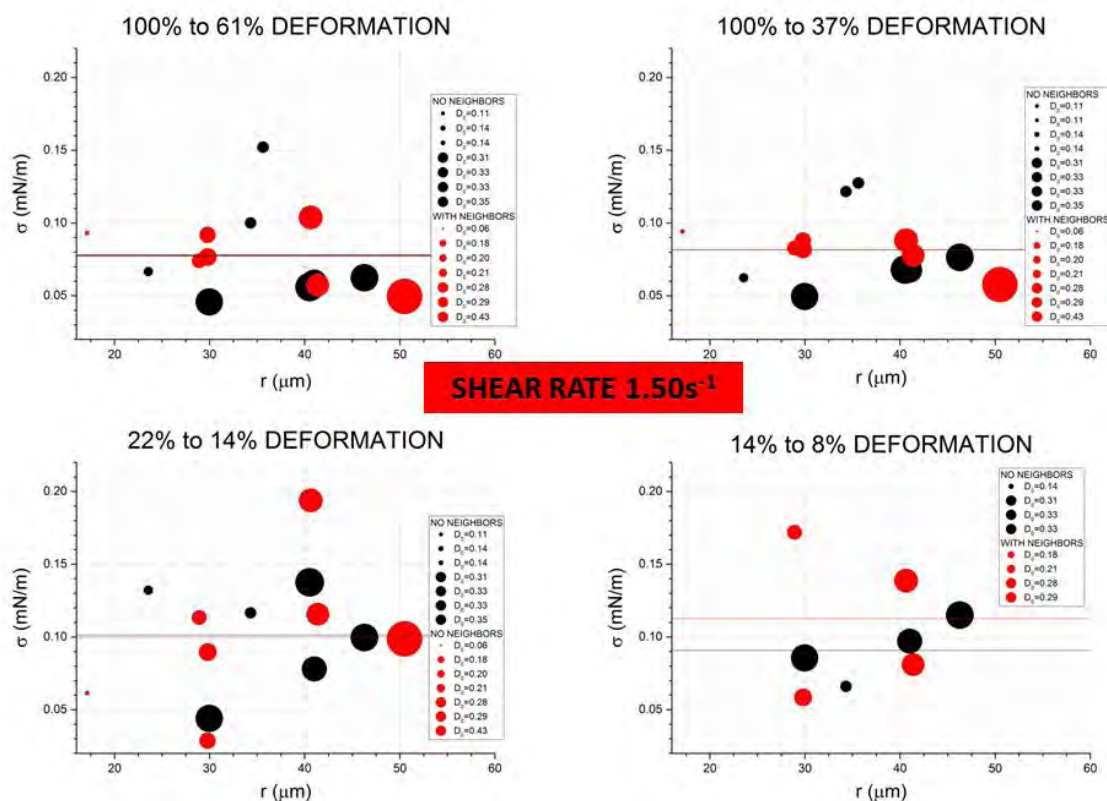
In each retraction, the Taylor deformation is calculated and graphically displayed on a logarithmic scale, and the slope is determined, and the corresponding clearance is made to obtain the value of the interfacial tension. Figure 5.5 shows the Taylor deformation (equation 5.3) graph for a drop of  $r = 28 \mu\text{m}$  in linear scale and the evolution of the  $L'$  and  $W$  axes of the ellipsoid of revolution associated with the drop retraction.



**Figure 5.5.** a) Taylor deformation for a drop of  $r=28\mu m$ , concerning to time. b) the evolution of the axes  $L'$  and  $W$  for the same drop.

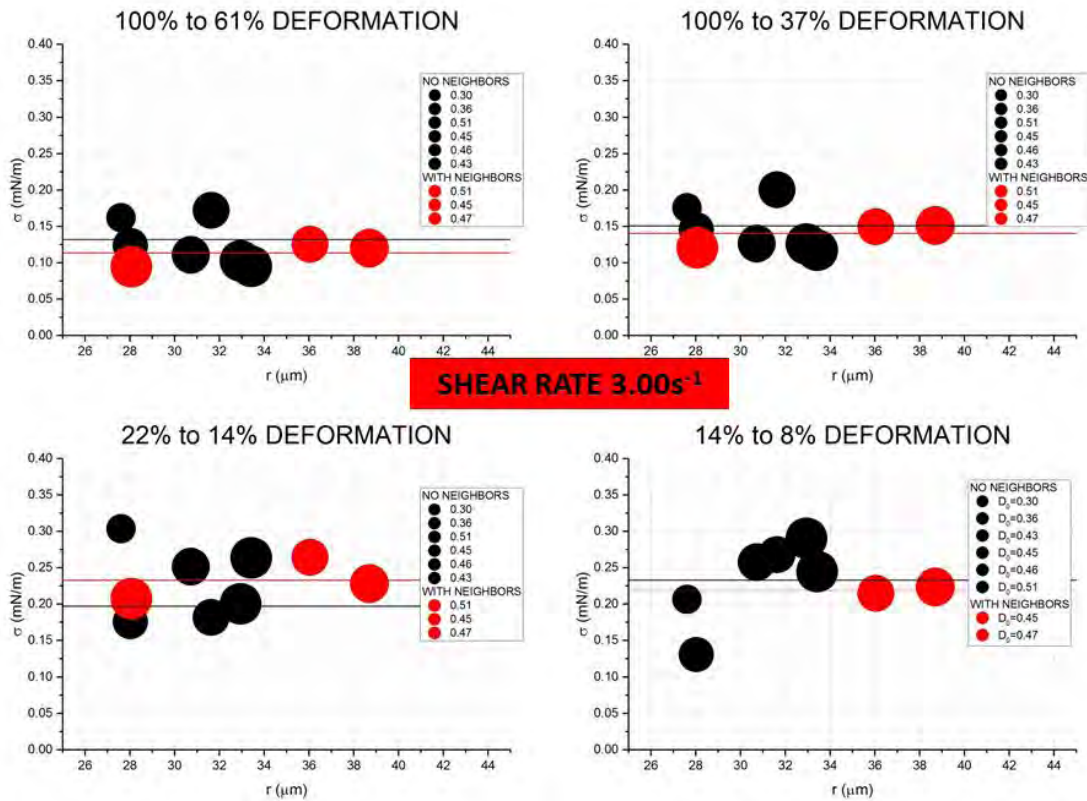
For the calculation of interfacial tension in each drop four measurements are made, the first one from 100 % to 61 % of the deformation which is equivalent to an interval of  $0 < \tau < 0.5$ ; the second from 100 % to 37 % of the deformation, which is equivalent to an interval of  $0 < \tau < 1$ ; the third is from 22 % to 14 % of the deformation, which is equivalent to an interval of  $1.5 < \tau < 2$  and the fourth is from 14 % to 8 % of the deformation, which is equivalent to an interval of  $2 < \tau < 2.5$ . as shown in figure 5.5.

The average for the first two ranges analyzed is 0.08 mN/m with neighbors and, the same value for isolated drops. For the next ranges are 0.10 mN/m for isolated drops and 0.11 mN/m with neighbors drops.



**Figure 5.6.** The averages (horizontal lines) of the interfacial stress measurement calculations for the analyzed ranges are presented. The size of each circle equals the initial deformation of the droplet just before stopping the flow.

For the shear rate of  $3.0 s^{-1}$  the measurements are made in the same ranges, with an average of  $0.14 mN/m$  with neighbors and  $0.13 mN/m$  without neighbors and for the third and fourth range of  $0.23 mN/m$  with neighbors and the same value without neighbors, are summarized in figure 5.6. These results are very diverse, therefore they are substantially disregarded. But its behavior is interesting to continue investigating the effect of the confinement between drops (concentrated emulsions) and the measurement of interfacial tensions by dynamic methods.

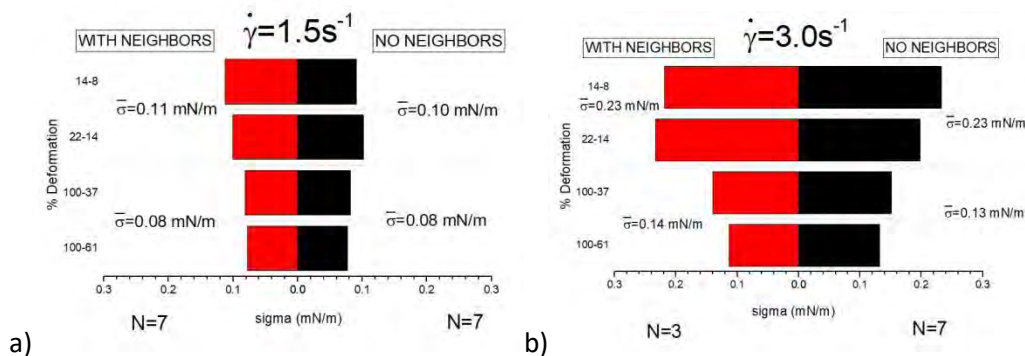


**Figure 5.7.** The averages (horizontal lines) of the interfacial stress measurement calculations for the analyzed ranges are presented. The size of each circle equals the initial deformation of the droplet just before stopping the flow.

In the same way, the initial deformation was plotted where it is possible to see are presented in the following table (table with standard deviations and more error data).

## 5.6. Discussion of Results

The interfacial tension calculations are presented in four time ranges using the DDR method, differences in their value are presented for conditions with neighbors and conditions of the isolated, an increase in the nominal value of the interfacial tension is presented, this can be seen as follows



**Figure 5.8.** Summary of the interfacial stress averages in the two shear forces and the neighbor and neighbor rating.

In calculating the interfacial tension of an emulsion, this is undoubtedly a complex problem, and even more so when it is required to be performed in situ. For a better understanding of the phenomenology of interfacial tension behavior, which is fundamental for multiple processes in the industry. The measurement of the interfacial tension by the DDR method, presumably is affected by the degree of confinement of the drop (or drops), in this way an idea is presented to identify the correlation between confinement and interfacial tension in concentrated emulsions..

## 5.7. References

- [1] Luciani A, Champagne MF, Utracki LA. Interfacial tension in polymer blends. In *Macromolecular Symposia* 1998 Jan 1 (Vol. 126, No. 1, pp. 307-321). Hüthig & Wepf Verlag.
- [2] Mo H, Zhou C, Yu W. A new method to determine interfacial tension from the retraction of ellipsoidal drops. *Journal of non-newtonian fluid mechanics*. 2000 Jul 1;91(2-3):221-32.
- [3] Sigillo I, Di Santo L, Guido S, Grizzuti N. Comparative measurements of interfacial tension in a model polymer blend. *Polymer Engineering & Science*. 1997 Sep;37(9):1540-9.
- [4] Guido S, Villone M. Measurement of interfacial tension by drop retraction analysis. *Journal of Colloid and Interface Science*. 1999 Jan 1;209(1):247-50.
- [5] Taylor GI. The viscosity of a fluid containing small drops of another fluid. *Proc. R. Soc. Lond. A*. 1932 Oct 1;138(834):41-8.
- [6] Taylor GI. The formation of emulsions in definable fields of flow. *Proc. R. Soc. Lond. A*. 1934 Oct 1;146(858):501-23.
- [7] Tjahjadi M, Ottino JM, Stone HA. Estimating interfacial tension via relaxation of drop shapes and filament breakup. *AIChE Journal*. 1994 Mar 1;40(3):385-94.
- [8] Tretheway DC, Leal LG. Deformation and relaxation of Newtonian drops in planar extensional flows of a Boger fluid. *Journal of Non-Newtonian Fluid Mechanics*. 2001 Jul 1;99(2-3):81-108.
- [9] Lerdwijitjarud W, Larson RG, Sirivat A, Solomon MJ. Influence of weak elasticity of dispersed phase on droplet behavior in sheared polybutadiene/poly (dimethyl siloxane) blends. *Journal of Rheology*. 2003 Jan;47(1):37-58.
- [10] Utracki LA. Compatibilization of polymer blends. *the Canadian journal of chemical Engineering*. 2002 Dec;80(6):1008-16.
- [11] Sibillo V, Simeone M, Guido S, Greco F, Maffettone PL. Start-up and retraction dynamics of a Newtonian drop in a viscoelastic matrix under simple shear flow. *Journal of Non-Newtonian Fluid Mechanics*. 2006 Mar 10;134(1-3):27-32.
- [12] Xing P, Bousmina M, Rodrigue D, Kamal MR. Critical experimental comparison between five techniques for the determination of interfacial tension in polymer blends: a model system of polystyrene/polyamide-6. *Macromolecules*. 2000 Oct 17;33(21):8020-34.
- [13] Rundqvist T, Cohen A, Klason C. The imbedded disk retraction method for measurement of interfacial tension between polymer melts. *Rheologica Acta*. 1996 Sep 1;35(5):458-69.

- [14] Carriere CJ, Cohen A, Arends CB. Estimation of interfacial tension using shape evolution of short fibers. *Journal of Rheology*. 1989 Jul;33(5):681-9.
- [15] Carriere CJ, Cohen A. Evaluation of the interfacial tension between high molecular weight polycarbonate and PMMA resins with the imbedded fiber retraction technique. *Journal of Rheology*. 1991 Feb;35(2):205-12.
- [16] Cohen A, Carriere CJ. Analysis of a retraction mechanism for imbedded polymeric fibers. *Rheologica Acta*. 1989 May 1;28(3):223-32.
- [17] Sigillo I, Di Santo L, Guido S, Grizzuti N. Comparative measurements of interfacial tension in a model polymer blend. *Polymer Engineering & Science*. 1997 Sep 1;37(9):1540-9.
- [18] Elemans PH, Janssen JM, Meijer HE. The measurement of interfacial tension in polymer/polymer systems: The breaking thread method. *Journal of Rheology*. 1990 Nov;34(8):1311-25.
- [19] Palierne JF. Linear rheology of viscoelastic emulsions with interfacial tension. *Rheologica Acta*. 1990 May 1;29(3):204-14.





## ***Chapter 6: General conclusions***

In this thesis, we focus on the influence of the shear rate on the morphology and microstructure of an emulsion, water in oil (W/O). The investigation was carried out along three lines. The first line is the statistical characterization of the data obtained in the emulsion and its evolution when the shear rate is increased. A non-parametric, smooth kernel distribution (SKD) method is used to fit to the evolution of the droplet size in steady state. The second line is the description of the formation of bands that appear when the shear rate is large. The third is the measurement of interfacial tension considering the deformed drop retraction (DDR) method.

## 6.1. Statistical Characterization of the Data of the Diameters of the Emulsion.

We considered six values of the shear rate to study the statistical evolution of the diameters of the emulsion. Each shear rate was increased from  $0.75 \text{ s}^{-1}$  to  $4.5 \text{ s}^{-1}$ , in steps of 0.75. We reach the following conclusions:

- Coalescence and rupture processes occur as a result of the imposed shear rate, affecting the emulsion morphology. for shear rates larger than  $3.0 \text{ s}^{-1}$  the formation of stable pearl necklaces is detected. this phenomenon is because the capillary number corresponding to the radii of the drops is slightly higher than the critical capillary for a single drop.
- The distribution at low shear rates has one significant mode; as a result of the two effects, the size distribution becomes bi-modal. The single-mode distribution results from the radius of the drops and the capillary number. That is to say that the drops are in the range of sizes because of the rupture of filaments: daughter droplets are of the same size. this fact has been reported in the literature, but the critical capillary number is about three times that of the single isolated droplet size.

- The behavior of drops of smaller size than the critical one and mono-modal distribution, favor the frequency of collision and therefore the coalescence. Due to this fact, the collision frequency decreases when the distribution is poly-dispersed.

## 6.2. Band Formation

The formation of concentration bands in the emulsion was observed when shear rate was applied.

- Band formation occurred for the case when the two fluids were newtonian, when the shear rate was relatively large and when the ratio of viscosities was smaller than unity.
- The separation of the plates is a crucial factor to observed the formation of bands. This conclusion was reached from previous studies of confinement in the literature [ref.20, Chapter 2].
- The zone of high concentration of drops is of higher viscosity than the zone of lower concentration of drops [ref. 23, Chapter 4]. However, there is an explicit dependence on the viscosity ratio and the shear rate.

- Using the simple model of a linear velocity profile we determine the effect of confinement in the band. However, due to the formation of the band itself, the linear velocity profile assumption is most likely inaccurate. Further detail measurements of the profile would be necessary.

### **6.3. Measurement of Interfacial Tension in Situ**

The use of dynamic methods for measuring the interfacial tension is only applicable for isolated drops. In this case, a comparison was made when the retraction of the drop is in confinement by neighboring drops. It is determined that the relaxation times are more significant when the neighbors are present, in comparison to the isolated case.

### **6.4. Suggestions for Future Work**

In this work, it was possible to identify the formation of bands in a concentrated emulsion. It is the first time that the formation of bands in parallel circular plates is reported. Then, the pending work would be to understand the correlation between the viscosity ratio and concentration with the formation of bands in situ. The evolution of the band in time would be the other line of work and to achieve a better understanding of the formation, permanence, and disappearance of the bands in concentrated emulsions. Also, it would be important to determine the

morphology of such bands. In particular, it is not known whether or not the bands are rings or spirals. A more in-depth analysis of the 3-D structure of the bands would have to be conducted.

Besides, and as an idea that "can" illuminate the way to a possible hypothesis. Is the average velocity field 3D ?, if it is, we could associate the last published works (Hof-Science 2004) that describe the processes of turbulence, which appears when there are normal components to the flow direction, (condition of the system study). The physics may be different, but the mathematical description must possibly be comparable.



**APPENDIX A****Sample Size**

Sample volume for the CSS450-LINKAM flow cell, and quantitative comparison of the number of drops in samples smaller than 0.5 milliliters.

Lower Lid Radius (mm)	GAP (mm)	GAP ( $\mu\text{m}$ )	Sample Volume ( $\text{mm}^3$ )	Sample Volume (mL)
20.5	0.01	10	13.20	0.01
20.5	0.04	40	52.81	0.05
20.5	0.09	90	118.82	0.12
20.5	0.1	100	132.03	0.13
20.5	0.16	160	211.24	0.21
20.5	0.25	250	330.06	0.33
20.5	0.36	360	475.29	0.48
20.5	0.49	490	646.92	0.65
20.5	0.64	640	844.96	0.84
20.5	0.81	810	1069.41	1.07
20.5	1	1000	1320.25	1.32
20.5	1.21	1210	1597.51	1.60
20.5	1.44	1440	1901.17	1.90
20.5	1.69	1690	2231.23	2.23
20.5	1.96	1960	2587.70	2.59
20.5	2.25	2250	2970.57	2.97



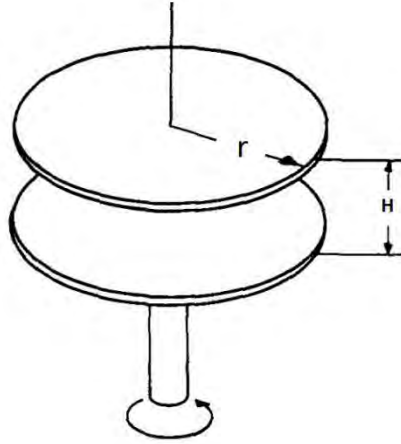
FOR OUR CASE							
Sample Volume (mL)	GAP	Volume Observed Under The Microscope ( $\mu\text{m}^3$ )	Drop Size Diameter ( $\mu\text{m}$ )	Number Of Drops Per Sample (50/50) ( $\text{g}^{-1}$ )	Number Of Drops Possible To Observe (50/50) ( $\text{g}^{-1}$ )	Surface Area Observed ( $\text{m}^2$ )	Surface Area Of The Sample ( $\text{m}^2$ )
0.13	100	1E+08	40	1.9E+06	2009	0.00001	9.75E-03
0.13	100	1E+08	35	2.9E+06	2999	0.00001	1.11E-02
0.13	100	1E+08	30	4.6E+06	4763	0.00001	1.30E-02
0.13	100	1E+08	25	7.9E+06	8230	0.00002	1.56E-02
0.13	100	1E+08	20	1.6E+07	16075	0.00002	1.95E-02
0.13	100	1E+08	15	3.7E+07	38104	0.00003	2.60E-02
0.13	100	1E+08	10	1.2E+08	128600	0.00004	3.90E-02
0.13	100	1E+08	5	9.9E+08	1028803	0.00008	7.80E-02

Drop Size Radius ( $\mu\text{m}$ )	Number Of Drops Per Gram Of Dispersed Phase ( $\text{g}^{-1}$ )	Surface Area Per Gram Of Dispersed Phase ( $\text{m}^2\text{g}^{-1}$ )
100	2.5E+05	0.0312
10	2.5E+08	0.312
1	2.5E+11	3.12
0.1	2.5E+14	31.2
0.01	2.5E+17	312

## ***APPENDIX B***

### **Theoretical Description of Parallel Circular Discs**

The movement of deformable particles in a flow (drops) has been widely studied both experimentally and theoretically; from Karman (1921) the flow created by the rotation of a disk is studied, where the velocity profiles are projected in the three dimensions, now for the particular case of the flow system produced by two parallel discs where one is stationary, and another rotates with an angular velocity  $\omega$ , in Figure 1, the geometry that I wish to study experimentally is shown.



**Figure A.1.** Flow geometry in cylindrical coordinates  $(r, \theta, z)$ , the upper steady disk  $z = H$  and the lower disk rotates with constant angular velocity  $\omega$ .

In cylindrical coordinates, we have that the velocity components in the radial and azimuthal directions are zero, where the velocity in the angular direction is given by equation 1.

$$v_{\theta} = \omega \cdot r \cdot \left(1 - \frac{z}{H}\right) \quad (\text{A.1})$$

$$\nabla \mathbf{v} = \begin{vmatrix} 0 & \omega \cdot \left(1 - \frac{z}{H}\right) & 0 \\ -\omega \cdot \left(1 - \frac{z}{H}\right) & 0 & 0 \\ 0 & -\omega \cdot \left(1 - \frac{z}{H}\right) & 0 \end{vmatrix} \quad (\text{A.2})$$

$$\mathbf{D} = \frac{1}{2} \cdot (\nabla \mathbf{v} + \nabla \mathbf{v}^T)$$

$$\mathbf{D} = \begin{vmatrix} 0 & 0 & 0 \\ 0 & 0 & -\omega \cdot \frac{r}{H} \\ 0 & -\omega \cdot \frac{r}{H} & 0 \end{vmatrix} \quad (\text{A.3})$$

$$\begin{aligned}
\mathbf{II}_{2D} &= \frac{1}{2} (\mathbf{I}_{2D}^2 + \text{Tr}((\mathbf{2D})^2)) \\
\mathbf{II}_{2D} &= -\frac{1}{2} \cdot \left( 2\omega^2 \cdot \frac{r^2}{H^2} \right) \\
\mathbf{II}_{2D} &= -\omega^2 \cdot \frac{r^2}{H^2}
\end{aligned} \tag{A.4}$$

Local

$$\dot{\gamma} = \sqrt{|\mathbf{II}_{2D}|} \tag{A.5}$$

$$\dot{\gamma} = \omega \cdot \frac{r}{H}$$

$$\begin{aligned}
\dot{\gamma}_{medio} &= \frac{1}{A} \cdot \int_S \dot{\gamma} \cdot da \\
\dot{\gamma}_{medio} &= \frac{1}{A} \cdot \int_{\theta=0}^{2\pi} \int_{r=0}^R \frac{\omega \cdot r}{H} \cdot r dr d\theta \\
\dot{\gamma}_{medio} &= \frac{2\pi}{\pi R^2} \cdot \frac{\omega}{H} \cdot \frac{r^3}{3} \Big|_{r=0}^R \\
\dot{\gamma}_{medio} &= \frac{2}{3} \cdot \frac{\omega}{H} \cdot R
\end{aligned} \tag{A.6}$$

in particular, the problem of two parallel discs can be seen a summary in the review of Gary Leal. For low Reynolds numbers. Experimental observations where very close to the center of the disk the flow remains stable at any rotation speed

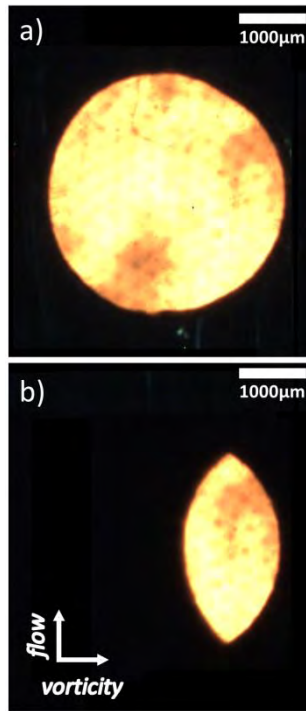
and secondary unstable movements are only observed in the angular region. The rotational flow of non-Newtonian liquids are important in a large number of technical applications: spinig-coating (centrifugal coating), the design of rotating machinery as a centrifuge and extruder, but especially in Rheology.

The observations and the calculations of the linear stabilities are presented for the stability of torsional flow of viscoelastic fluids between two parallel discs, one will be stationary, and another will move with constant angular velocity, purely the critical value of the rotation speed (Deborah number) , the purely circumferential, viscometry of the base may be unstable with respect to a non-asymmetric, time-dependent movement consisting of spiral vortices which travel to the outer through the disks.

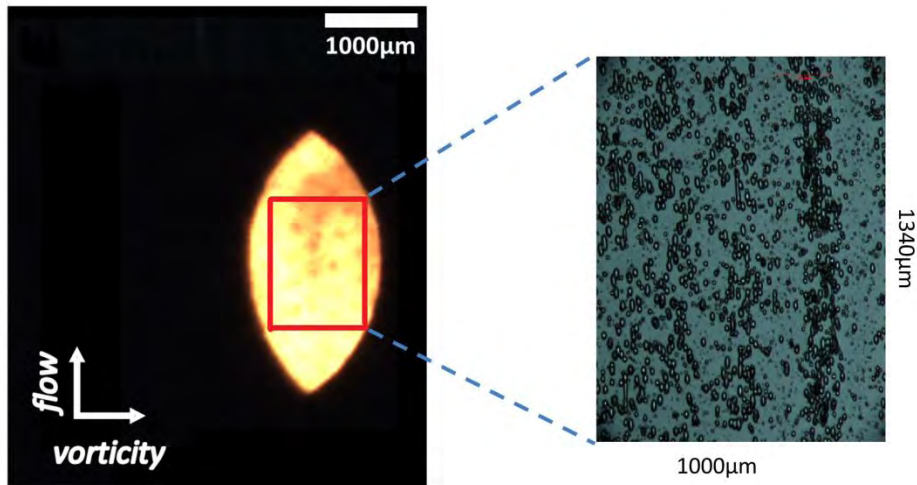
## ***APPENDIX C***

### **Location of the Image Captured in the Observation Hole.**

Figure C.1a shows an image of the observation hole without the top cover of the cell (CSS450-LINKAM) and figure C.2 with the cover. An eclipse is observed between the two lids, this is the product of the type of microscope used in the experiment, a Nikon SMZ-U (Manufacturer Nikon Corp., Tokyo, Japan), and this microscope is stereoscopic. The location of the captured images is just at the outer edge of the observation hole.



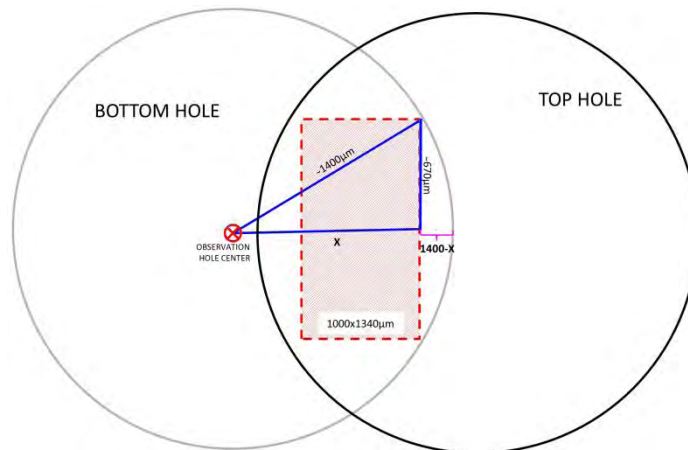
**Figure C.1.** The zoom with which the images were captured was  $\times 3.5$ . The hole has a diameter of 2.8 mm. The arrows indicate the direction of the axes, with the center of rotation to the left of the image; a) Observation hole of the cell without lid, and b) Observation hole with top lid.



**Figure C.2.** The dimensions and the location of the captured images are shown. The size of the image is  $1000 \times 1340 \mu\text{m}$ .

Remember the dimensions of the cell and the observation hole; we search deduce that the edge of the right of the hole is at  $7500 \mu\text{m} + 1400 \mu\text{m}$ . The center of the observation hole is at  $7500 \mu\text{m}$  ( $7.5 \text{ mm}$ ) from the center of rotation. The radius of the hole is  $1400 \mu\text{m}$  ( $1.4 \text{ mm}$ ).

Forming a rectangle triangle (figure C.3.) we search deduce that the distance  $X = \sim 1230 \mu\text{m}$ . Therefore, the right edge of the captured images is  $\sim 170 \mu\text{m}$  from the inner hole shape. It is important to note that the instruments used to align the horizontal axis of the holes are of the order of  $\sim 2 \mu\text{m}$ .



**Figure C.3.** Scheme of the two holes and location of the captured images.

There always exists, and there will be a limit to the precision with which measurements can be made. It is inevitable in every measure to have an error in the decimal digits inferior to the accuracy of the device or device used. Although the entire measurement process is carried out "correctly," the measured value has at least one error level given by the precision of the instrument used. As



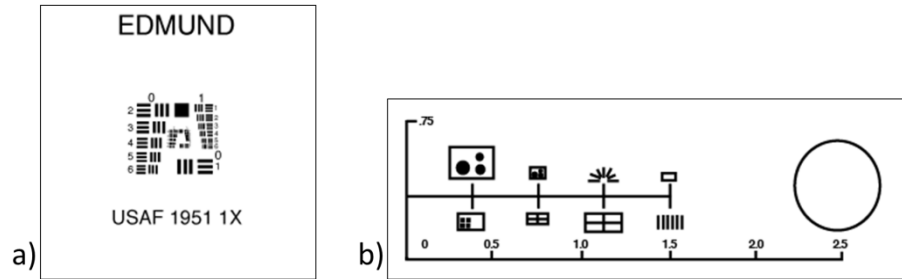
mentioned earlier it is of the order of  $\sim 2 \mu\text{m}$ . Below are the instruments used for the alignment of the equipment.

- Mitutoyo 513-405E. Dial Test Indicator, Horizontal Type. 0,2 mm, 0,002mm.
- Mitutoyo 513-103. Dial Test Indicator, Horizontal Type. 0,2mm, 0,002mm.
- Mitutoyo 2119-51 Dial Indicator 0.001-5mm.
- Mitutoyo 2050-11 Dial Indicator 0.01-5mm.
- Mitutoyo 183-902 8x Pocket Comparator with Six Reticles and Case.

## ***APPENDIX D***

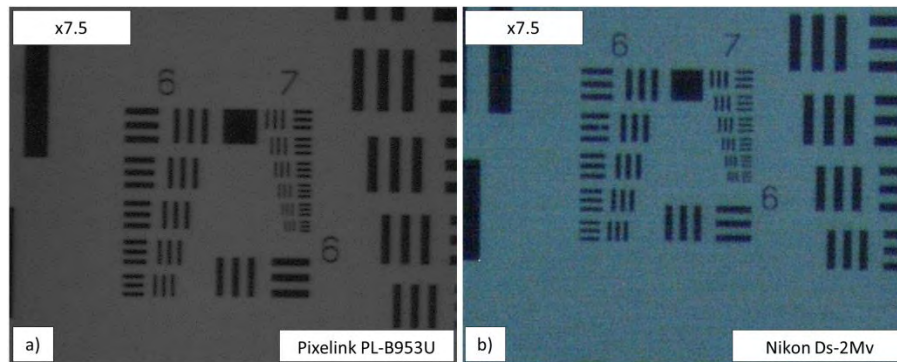
### **Calibration and Resolution of the Image**

The target test to determine the resolution of the images is 1951 USAF (2"x2" positive), manufactured by Edmund Optics and the micrometric TARGET TEST (Edmund optics) for the calibration and verification of the horizontal and vertical lengths of the image. Figure D.1 shows the technical images of the target tests used. The USAF 1591 target test is used with the two cameras to determine the resolution of the captured images.



**Figure D.1.** a) Technical image of 1951 USAF target (2"x2" positive), manufactured by Edmund Optics, b) technical image of image analysis micrometer

In Figure D.2a, you can see up to group 7 and element 4, therefore, the resolution is  $2.76 \mu\text{m}$ . (see Table D.1). Figure D.2b shows up to group 7 and element 6, so the resolution is  $2.19 \mu\text{m}$  (see Table D.1).



**Figure D.2.** a) Image captured with the Pixelink PL B953U camera, b) Image captured with the DS-2Mv camera. The two images have the size of 500x400 pixels.

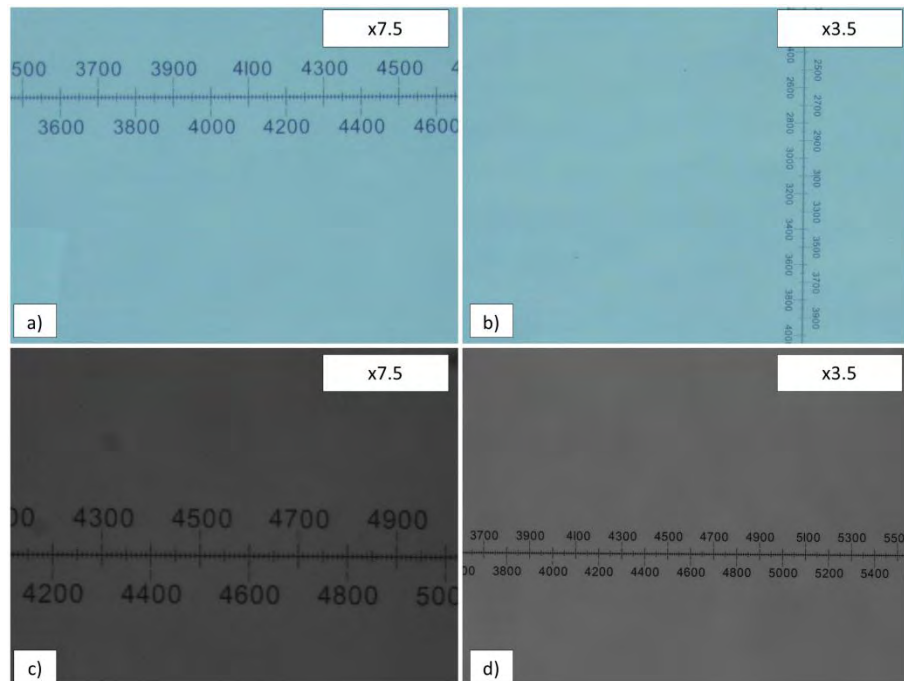
	Group Number								
Element	1	2	3	4	5	6	7	8	9
1	250.00	125.00	62.50	31.25	15.63	7.81	3.91	1.95	0.98
2	222.72	111.36	55.68	27.84	13.92	6.96	3.48	1.74	0.87
3	198.43	99.21	49.61	24.80	12.40	6.20	3.10	1.55	0.78
4	176.78	88.39	44.19	22.10	11.05	5.52	2.76	1.38	0.69
5	157.49	78.75	39.37	19.69	9.84	4.92	2.46	1.23	0.62
6	140.31	70.15	35.08	17.54	8.77	4.38	2.19	1.10	0.55

**Table D.1.** The width of 1 line in micrometers in USAF Resolving Power Test Target 1951.

For the calibration of the length of the images, 10 measurements were taken for each zoom, the average of the 10 measurements is chosen. The summary is indicated in table D.2.

Zoom	DS-2Vm				Pixelink PL-B953U			
	Horizontal px/ $\mu\text{m}$	Standard Deviation	Vertical px/ $\mu\text{m}$	Standard Deviation	Horizontal px/ $\mu\text{m}$	Standard Deviation	Vertical px/ $\mu\text{m}$	Standard Deviation
x0.75	0.085	0.006	0.084	0.003	--	--	--	--
x1.5	0.172	0.002	0.171	0.007	0.222	0.008	0.223	0.005
x2.5	0.284	0.002	0.285	0.004	0.371	0.008	0.371	0.007
x3.5	0.402	0.002	0.404	0.006	0.521	0.006	0.521	0.005
x4.5	0.520	0.003	0.520	0.006	0.671	0.005	0.672	0.004
x5.5	0.630	0.004	0.629	0.002	0.817	0.005	0.817	0.009
x6.5	0.745	0.003	0.748	0.003	0.968	0.009	0.968	0.011
x7.5	0.862	0.006	0.861	0.007	0.979	0.007	0.978	0.008

**Table D.2.** Calibration in px /  $\mu\text{m}$



**Figure D.3** Images captured with the Ds-2Mv camera, the size of each image is 1080x830 pixels.



## APPENDIX E



Article

## Evolution of the Size Distribution of an Emulsion under a Simple Shear Flow

Jairo M. Leiva \* and Enrique Geffroy

Instituto de Investigaciones en Materiales, Universidad Nacional Autónoma de México, Ciudad Universitaria, 04510 Cd. de México, CDMX, Mexico; geffroy@unam.mx

\* Correspondence: eleiva@iim.unam.mx; Tel.: +52-55-5622-4632

Received: 25 April 2018; Accepted: 20 June 2018; Published: 25 June 2018



**Abstract:** Understanding the rheology of immiscible liquids mixtures, as well as the role played by its micro-structures are important criteria for the production of new materials and processes in industry. Here, we study changes over time of the droplet size distributions of emulsions induced by slow shearing flows. We observe that the initial heterogeneous microstructure may evolve toward more complex structures (such as bimodal distribution) as a result of coalescence and rupture of droplets. These dynamic structures were produced using a flow cell made up of two parallel disks, separated by a gap of 100  $\mu\text{m}$ . The steady rotation of the lower disk generates a simple shear flow of  $\dot{\gamma} = 0.75 \text{ s}^{-1}$ , during  $\sim 400 \text{ s}$ . After a brief rest time, this procedure was repeated by applying a step ramp until the maximum shear rate of  $4.5 \text{ s}^{-1}$  was reached, using step increments of  $0.75 \text{ s}^{-1}$ . During the last portion of the flow and during the rest time in between flows, structures of emulsions were characterized. Initially, a broad single-peak distribution of drops was observed, which evolved toward a rather narrower bimodal distribution, at first due to the coalescence of the smaller droplets and subsequently of the larger drops. The rupture of drops at higher shear rates was also observed. The observed evolutions also presented global structures such as “pearl necklaces” or “bands of particles”, the latter characterized by alternating bands of a high density of particles and regions of the continuous phase with only a few droplets. These changes may indicate complex, time-dependent rheological properties of these mixtures.

**Keywords:** emulsion microstructure; drop size distribution; monomodal–bimodal distributions







"Se asentó y ha quedado por costumbre, que los que se graduasen de doctores y maestros es cualquier facultad envíen las conclusiones a todos los doctores y maestros a sus casas con los bedeles o persona de calidad, con música de trompetas, pompa y aparato y que se diese vejamen en los grados de doctor; y acabados los grados, en el teatro se den guantes a los señores doctores y maestros, un para cada uno, y por cada cosa que faltase, fuese multado con 30 pesos"